UNIVERSITY OF MICHIGAN
JUN 16 1959
ENGINEERING LIBRARY

THE AERONAUTICAL QUARTERLY

A Journal devoted to Aeronautics and the Allied Sciences

Volume X MAY 1959 Part 2

CONTENTS

The Effect of Jet Noise on Aircraft Structures — *B. L. Clarkson*

Note on the Forces that Act near the Centre and the Tips of a Swept-Back Wing — *D. G. Hurley*

On the Buckling of Certain Optimum Plate Structures with Linearly Varying Thickness — *E. H. Mansfield*

Flow in a Viscous Trailing Vortex — *B. G. Newman*

A Contribution to the Theory of Flow Stability in Multi-Stage Axial Compressors — *A. D. S. Carter*

Asymmetrically Plate-Reinforced Circular Hole in a Uniformly End-Loaded Flat Plate — *Raymond Hicks*

LONDON

ROYAL AERONAUTICAL SOCIETY

4 HAMILTON PLACE W1

15/-

THE AERONAUTICAL QUARTERLY

Editorial Board

Dr. A. M. BALLANTYNE, T.D., B.Sc., Ph.D., Hon.F.C.A.I. F.I.A.S., F.R.Ae.S. (*Chairman*)

Mr. HAYNE CONSTANT, C.B., C.B.E., M.A., F.R.S., F.R.Ae.S.

Sir HAROLD ROXBEE COX, D.Sc., D.I.C., Ph.D., F.I.A.S., F.R.Ae.S.

Sir WILLIAM FARREN, C.B., M.B.E., M.A., D.Sc., F.R.S., Hon.F.I.A.S., Hon.F.R.Ae.S.

Sir ARNOLD HALL, M.A., F.R.S., F.R.Ae.S.

Sir BENNETT MELVILL JONES, C.B.E., A.F.C., M.A., F.R.S., Hon.F.I.A.S., Hon.F.R.Ae.S.

Sir ALFRED PUGSLEY, O.B.E., D.Sc., F.R.S., F.R.Ae.S.

Sir GEOFFREY TAYLOR, M.A., D.Sc., F.R.S., Hon.F.R.Ae.S.

Dr. P. B. WALKER, C.B.E., M.A., F.R.Ae.S.

Editor—E. C. PIKE, M.A., A.F.R.Ae.S.

Editorial Referees

Aerodynamics

(a) *General*

Sir LEONARD BAIRSTOW
Mr. D. KEITH-LUCAS
Prof. W. A. MAIR
Mr. L. F. NICHOLSON
Dr. R. C. PANKHURST
Mr. E. F. RELF
Prof. E. J. RICHARDS
Dr. B. THWAITES

(b) *Fluid Motion*

Dr. G. K. BATCHELOR
Mr. A. FAGE
Dr. D. W. HOLDER
Prof. L. HOWARTH
Dr. W. P. JONES
Dr. J. W. MACCOLL
Prof. J. H. PRESTON
Prof. H. B. SQUIRE
Prof. G. TEMPLE
Prof. G. N. WARD
Prof. A. D. YOUNG

(c) *Stability and Control*

Mr. L. W. BRYANT
Mr. S. B. GATES
Mr. H. B. IRVING
Mr. G. H. LEE
Mr. M. B. MORGAN
Mr. H. H. B. M. THOMAS

Helicopters and Propellers

Prof. J. A. J. BENNETT
Mr. P. BRETT
Mr. L. G. FAIRHURST
Mr. R. HAFNER
Dr. G. S. HISLOP
Capt. R. N. LIPTROT

Instruments and Electrical Equipment

Dr. G. E. BAIRSTO
Sir GEORGE GARDNER
Dr. C. S. HUDSON
Mr. C. N. JAQUES
Mr. F. W. MEREDITH

Aircraft Design

Mr. R. BOORMAN
Mr. R. M. CLARKSON
Mr. A. N. CLIFTON
Mr. H. H. GARDNER
Mr. H. KNOWLER
Mr. W. E. W. PETTER
Mr. F. H. POLLICUTT
Dr. A. E. RUSSELL
Mr. R. S. STAFFORD
Mr. W. H. STEPHENS

Radio and Radar

Mr. J. F. ATHERTON
Mr. B. G. GATES
Dr. R. L. SMITH ROSE
Dr. A. M. UTTLEY
Sir ROBERT WATSON-WATT

Aviation Medicine

Dr. K. G. BERGIN
Dr. A. BUCHANAN BARBOUR

Meteorology

Sir DAVID BRUNT
Mr. J. K. HARDY
Prof. P. A. SHEPPARD

Sound

Mr. W. MAKINSON
Mr. F. B. GREATREX
Mr. N. FLEMING

Aircraft Propulsion

Mr. A. D. BAXTER
Mr. A. V. CLEAVER
Sir A. H. ROY FEDDEN
Dr. S. HOOKER
Mr. A. R. HOWELL
Mr. W. H. LINDSEY
Mr. P. LLOYD
Dr. A. W. MORLEY
Dr. E. S. MOULT
Mr. N. S. MUIR
Mr. F. NIXON
Mr. F. M. OWNER
Mr. H. PEARSON
Sir DAVID PYE
Mr. H. SAMMONS
Prof. O. A. SAUNDERS
Prof. A. G. SMITH

Air Transport

Mr. A. C. CAMPBELL ORDE
Mr. P. G. MASEFIELD
Mr. N. E. ROWE
Mr. B. S. SHENSTONE
Mr. W. TYE

Aircraft Accessories

Mr. A. E. BINGHAM
Mr. W. C. CLOTHIER
Mr. H. G. CONWAY
Sir GEORGE DOWTY
Mr. R. GRAHAM
Mr. C. D. HOLLAND

Performance

Mr. H. DAVIES
Mr. D. R. NEWMAN
Mr. A. H. YATES

Flight Testing

Mr. R. R. DUDDY
Mr. P. A. HUFTON
Mr. E. T. JONES
Mr. S. SCOTT HALL
Mr. H. L. STEVENS

Structures

Mr. A. C. BROWN
Mr. H. L. COX
Mr. D. J. FARRAR
Prof. W. S. HEMP
Prof. R. HILL
Mr. H. B. HOWARD
Col. H. T. JESSOP
Mr. E. D. KEEN
Mr. F. A. KERRY
Dr. D. M. A. LEGGETT
Mr. R. L. LICKLEY
Prof. A. J. SUTTON PIPPARD
Prof. S. C. REDSHAW
Mr. R. H. SANDIFER
Sir RICHARD SOUTHWELL

Fuels and Oils

Mr. E. L. BASS
Dr. J. W. DRINKWATER
Prof. F. H. GARNER
Prof. W. E. GARNER
Dr. K. E. W. RIDLER
Dr. C. G. WILLIAMS

Materials

Dr. L. AITCHISON
Dr. N. P. ALLEN
Mr. G. FORREST
Prof. N. F. MOTT
Mr. L. ROTHERHAM
Dr. H. SUTTON
Dr. C. SYKES

Vibration and Flutter

Mr. E. G. BROADBENT
Prof. A. R. COLLAR
Prof. W. J. DUNCAN
Dr. R. A. FRAZER
Mr. H. TEMPLETON
Mr. M. O. W. WOLFE

The Effect of Jet Noise on Aircraft Structures

B. L. CLARKSON, B.Sc., Ph.D.

(*Department of Aeronautical Engineering, The University of Southampton*)

SUMMARY: The present state of knowledge on the problem of fatigue failure due to vibrations excited by jet noise is reviewed. It is concluded that it should currently be possible to make reasonable estimates of the stress levels set up in a structure by jet noise but, in general, the resultant fatigue life of the components cannot be estimated with any confidence.

1. Introduction

The efflux from a jet engine produces fluctuating noise pressures which cause vibration of those parts of the aircraft structure situated in the region of the jet. The pressures are varying randomly in the statistical sense and cover a wide range of frequencies. Therefore, as a result of this wide frequency spectrum, resonant vibrations are set up in the structure. Such vibrations are generally of low amplitude but, because of their high frequency, a large number of stress reversals can be produced in a relatively short running time. The possibility of fatigue failure of these parts must now be considered in the design of the structure. The overall solution of the problem requires a study of many interrelated topics and the purpose of this paper is to review and co-ordinate the work being done in this field.

The complete analysis of the problem of fatigue failure due to vibrations excited by jet noise requires a detailed study of each of the following items:—

(*i*) General theory of structural response to random pressure loads.

(*ii*) Characteristics of the noise pressure field.

(*iii*) Mechanical impedance of the aircraft structure.

(*iv*) Practical approximations to the general case by considering panel vibrations.

(*v*) Fatigue life estimation.

The applied loads on the structure take the form of randomly varying pressures associated with noise which has a wide frequency spectrum. A statistical approach to the problem by using the method of generalised harmonic analysis is therefore the most convenient. By considering each normal mode of vibration of the structure separately, it is possible to use Lagrange's equations of motion to obtain the mean square value of the response to random loads. The random loading

Received July 1958.

[The Aeronautical Quarterly, Vol. X, May 1959]

must be defined by its power spectrum and also by its spatial correlation over the structure. The effectiveness of this loading in exciting a given mode of vibration is a function of its spatial correlation and of the mode deflection. The response of a structure to a given loading depends on the vibration characteristics of the structure. In aircraft structures the damping is low and the power spectrum of the noise pressure is relatively flat. Thus a practical solution can be obtained on the assumption that the response is essentially resonant.

It has been shown that the relevant properties of the noise pressure field are the pressure power spectrum and the spatial correlation of pressures over the whole structure. The mechanism of noise production by a jet efflux is so complicated that these properties must be obtained experimentally. The power spectrum of jet noise is relatively flat, indicating that the random pressure fluctuation can be considered to be made up of components in a wide range of frequencies. Close to the nozzle the power spectrum peaks towards the higher frequencies, while farther downstream the peak moves towards the lower frequencies. There is as yet no means of calculating this power spectrum to within the accuracy required for structural response calculations. Because of random variations in the noise pressure field close to the jet, the phase relationship along the structure must be obtained by correlation measurements. In this region the area of positive correlation of the overall pressure is of the order of one nozzle diameter. For points in the far field the jet can be considered to form a point source and hence the correlation can be calculated directly.

The vibration characteristics of the structure are defined by the normal modes and natural frequencies of vibration, together with the associated damping. In the present state of knowledge the normal modes of vibration of the general case of a stiffened cylinder of the type used in aircraft construction cannot be determined theoretically. However, in the special case of stiffeners, whose spacing is close compared with the flexural wavelengths, a modification of the simple case of a uniform cylinder can be made to render the problem tractable. This assumption of closely spaced longitudinal and circumferential stiffeners may adequately cover about half the number of modes significant in jet noise excitation. Thus further investigation is urgently required into the general case. The damping of the normal modes is due to energy dissipation in the material itself, joint slip, and sound radiation. As the mean square stress level is inversely proportional to the damping ratio, an increase in the damping will automatically produce a reduction in stress levels. Structural damping can be increased by the addition of damping materials to the inner surface of the structure or as interlayers at the joints. Acoustic damping cannot be varied appreciably on a given aircraft, but in the design stage of a new aircraft it may be possible to design for high acoustic damping.

As the correlation area is of the same order as the area of typical panels, it is probable that the form of vibration of the complete structure approximates to that of predominantly panel or stringer vibrations. However, this is a special case of the overall vibration of a stiffened cylinder subjected to localised loading and should

be treated generally until experience on typical structures justifies the approximation. Considerable experimental and theoretical work has been done on single panels subjected to high intensity acoustic loading, but in general it is not possible to extrapolate these results to the case of the complete structure. Such tests provide an indication of the relative fatigue lives of different panels but cannot reliably predict the magnitude of the fatigue life on the actual aircraft.

It can be concluded, therefore, that in the present state of knowledge it should be possible to make reasonable estimates of the stress levels set up in a structure by jet noise, but the fatigue life of components under these conditions cannot be estimated with any confidence. The effect of random loading at low stress levels needs considerable investigation. However, in special cases it may be possible to make estimates based on full-scale test experience on a similar structure and then use the theory to allow for the effect of structural changes.

NOTATION

A area of structure, amplitude of axial displacement
a element of area
B amplitude of circumferential displacement
b panel wavelength
C amplitude of radial displacement
c generalised viscous damping, velocity of sound
f_e equivalent frequency (c./s.)
h constant to convert displacement to stress
j joint acceptance
k generalised stiffness
L generalised force
l length of cylinder
m generalised mass, number of longitudinal half-waves
N' number of root-mean-square stress reversals to produce failure
n total number of modes, number of circumferential waves
P overall noise pressure
p noise pressure in a narrow frequency band
R correlation coefficient
S panel stress due to static pressure
T time to failure
t time
u axial displacement

v circumferential displacement

w radial displacement

x distance along cylinder

Y mechanical impedance

y mode deflection, ratio of stress to root-mean-square stress

δ damping ratio

η reduction factor

θ angle of incident sound waves

λ sound wavelength

ξ generalised co-ordinate

σ stress

τ time delay

ϕ radial position

ω frequency (rad./sec.)

Suffixes

0 denotes reference point

s denotes general mode

2. General Theory of Structural Vibrations Excited by Random Loads

2.1. Introduction

When a structure is subjected to random pressure loads, associated with a jet efflux, the resultant stresses are also random in nature. In this case instantaneous values of stress are meaningless, and therefore the problem must be treated statistically. The pressure loading has a wide frequency spectrum, causing excitation of many natural modes of vibration of the structure. In these circumstances the most convenient method of analysis is to use the Lagrange equations to consider the excitation of each normal mode of the structure independently. This assumes that the coupling between modes is negligible, and is justified by the fact that the damping of the normal modes is small. The total response of the structure is then obtained by combining the effects in each mode. The general study of random loading of a structure indicates what information about the exciting forces is required and shows in general terms the form of the response. It is shown later that, owing to the peculiarities of the system and of the excitation, it is possible to make simplifications which render the problem tractable. The method used is that of Generalised Harmonic Analysis developed by Liepmann[1] and others and applied by Powell[2, 3, 4] to this particular problem.

2.2. Response of a Structure to Random Loading

Consider the response of the structure, in the s^{th} mode of vibration due to random noise pressures. The Lagrange equation for this mode has the form

$$m_s\ddot{\xi}_s + c_s\dot{\xi}_s + k_s\xi_s = L_s(t) \quad (s=1 \text{ to } n)$$

where m_s, c_s, k_s, $L_s(t)$ are the generalised mass, generalised viscous damping, generalised stiffness and generalised force respectively. ξ is the generalised co-ordinate of the mode, *i.e.* the deflection of the reference point.

The solution of this equation yields the power spectral density of the displacement for the s^{th} mode,

$$w_{\xi_s}(\omega) = \frac{w_L(\omega)}{|Y(\omega)|^2},$$

and the mean square value of displacement is

$$\overline{\xi_s^2} = \int_0^\infty w_{\xi_s}(\omega)\, d\omega = \int_0^\infty \frac{w_L(\omega)}{|Y(\omega)|^2}\, d\omega,$$

where $Y(\omega)$ is the mechanical impedance of the system, *i.e.*

$$|Y(\omega)|^2 = m^2\left[(\omega_s^2-\omega^2)^2 + \frac{c^2}{m^2}\omega^2\right]$$

ω_s = natural frequency of the s^{th} mode

and $w_L(\omega)$ = power spectral density of the generalised force.

Now the generalised force

$$L(t) = \int_A P(t, a)\, y(a)\, da,$$

where $P(t, a)$ is the randomly varying noise pressure on the element of area of the structure, and $y(a)$ is the mode deflection relative to the reference point, which is taken as unity. The square of the generalised force is

$$\{L(t)\}^2 = \int_A \int_A P(t, a)\, P(t, a')\, y(a)\, y(a')\, da\, da'.$$

In this expression the product $P(t, a)\, P(t, a')$ is the spatial correlation of the total noise pressures at positions a and a'.

The power spectral density of the generalised force at frequency ω is

$$w_L(\omega) = \int_A \int_A p(t, a)\, p(t, a')\, y(a)\, y(a')\, da\, da',$$

where $p(t, a)\, p(t, a')$ is now the spatial correlation of the noise pressures in a narrow frequency band of central frequency ω. This correlation function can be normalised by dividing by the mean square pressure at some reference element a_0.

Re-writing:—

$$w_L(\omega) = \int_A \int_A \overline{p(t, a_0)^2}\, \frac{p(t, a)\, p(t, a')}{\overline{p(t, a_0)^2}}\, y(a)\, y(a')\, da\, da',$$

where now

$$\frac{p(t, a)\, p(t, a')}{\overline{p(t, a_0)^2}} = \text{the correlation coefficient in a narrow band having a central frequency } \omega$$

$$= R_\omega, \text{ say}$$

and $\overline{p(t, a_0)^2}$ = the power spectral density of the noise pressures in a narrow band at frequency ω and station a_0

$$= w_{p0}(\omega), \text{ say}$$

Therefore $$w_L(\omega) = \int_A \int_A w_{p0}(\omega)\, R_\omega\, y(a)\, y(a')\, da\, da'.$$

Thus the power spectral density of displacement

$$w_\xi(\omega) = \frac{w_L(\omega)}{|Y(\omega)|^2} = \frac{1}{|Y(\omega)|^2} \int_A \int_A w_{p0}(\omega)\, R_\omega y(a)\, y(a')\, da\, da'.$$

As the mode shape is known, the power spectral density of the stress at any point can be determined directly from $w_\xi(\omega)$. It is simply

$$w_s(\omega) = \frac{h_s^2}{|Y(\omega)|^2} \int_A \int_A w_{p0}(\omega)\, R_\omega y(a)\, y(a')\, da\, da',$$

where h_s is a constant converting the displacement of the reference point in the s^{th} mode to the stress at any required point in the mode.

It is seen from these expressions that the information required to arrive at a solution is

(*i*) $w_{p0}(\omega)$, the power spectral density of the noise pressure at some reference point.

(*ii*) R_ω, the narrow band spatial correlation of the noise pressures over the whole structure.

(*iii*) $Y(\omega)$, the mechanical impedance of the structure which is dependent on

(*a*) The normal structural modes and natural frequencies of vibration.

(*b*) The damping of the normal modes.

(*iv*) $y(a)$, the mode shape.

2.3. Further Consideration of the Generalised Force

2.3.1. *General*

Several specialised cases of the generalised force can now be considered. It is convenient to re-write the expression for the generalised force as

$$w_L(\omega) = w_{p0}(\omega) A^2 \left[\frac{1}{A^2} \int_A \int_A R_\omega y(a) y(a') \, da \, da' \right].$$

The term in square brackets is now non-dimensional, having values equal to, or less than, unity. It is a measure of the inter-relationship between pressures and the mode deflections and its square root has been termed " joint acceptance " by Powell and denoted by j. We have then simply that the power spectral density of the generalised force is given by

$$w_L(\omega) = w_{p0}(\omega) A^2 j^2,$$

where j is a factor to be determined from the space correlation and the mode deflection.

2.3.2. *Near Field*

For structure in the near field of the jet it is not possible to calculate R_ω. Thus j^2 must be obtained from experimentally determined values of R_ω. In the special case of a correlation coefficient falling off rapidly to zero in a distance which is short compared with the half wavelength of the mode, the mode deflections $y(a)$, $y(a')$ will be approximately equal over the region having appreciable values of R_ω.

Then $$j^2(\omega) \simeq \frac{1}{A^2} \int_A R_\omega y^2(a) \, da = \frac{y^2(a)}{A^2} \int_A R_\omega da,$$

which can readily be evaluated. When this condition is not true the calculation of $j^2(\omega)$ is best carried out on a digital computer.

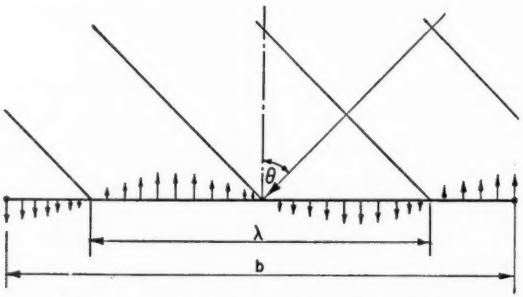

FIGURE 1. Pressure loads on a panel due to an incident sound wave.

2.3.3. *Far Field*

For structure in the far field of the jet, R_ω, and hence $j^2(\omega)$, can be calculated directly. Assume that the sound wave is incident on the structure at an angle θ, as shown in Fig. 1. The velocity of the plane waves is c, the velocity of sound, and the velocity of the trace waves along the panel is $c/\sin\theta$. The trace wavelength is assumed equal to λ.

Consider the case of the panel vibrating as a rigid body, giving $y(a)=y(a')=1$. When the trace wavelength λ is very long compared with the span b there will be effectively a uniform pressure loading along the panel, in which case R_ω approaches unity. Therefore $j^2(\omega)=1$ for $b/\lambda=0$. It can readily be seen that when $b/\lambda=1$ pressures on one half of the beam will be balanced by suctions on the other half and $j^2(\omega)=0$. The complete curve for the variation of $j^2(\omega)$ with b/λ is given by

$$j^2(\omega)=\left(\frac{\lambda}{\pi b}\sin\frac{\pi b}{\lambda}\right)^2$$

and is shown in Fig. 2.

Consider now the case of the panel vibrating in a sinusoidal mode having n half-waves of wavelength b. In the special case when $n=1$ there will be a node at each support and all parts of the panel will have deflections in phase. The maximum excitation will occur when $b/\lambda=0$, as in the previous case. When there are several semi-wavelengths in the panel, maximum excitation will occur when the pressure is everywhere in phase with the deflection, which is achieved when $b/\lambda=1$. The variation of $j^2(\omega)$ with b/λ is shown in Fig. 3 and is given by

$$j^2(\omega)=\frac{2}{\pi^2 n^2}\left(\frac{1}{1-b^2/\lambda^2}\right)^2\left\{1-(-1)^n\cos(n\pi b/\lambda)\right\}.$$

It can be seen from this that a typical structure, vibrating in a mode of n half-waves, acts as a wavelength filter. The highest response is obtained when the trace wavelength is equal to the mode wavelength. It can also be seen that the selectivity increases as the value of n increases.

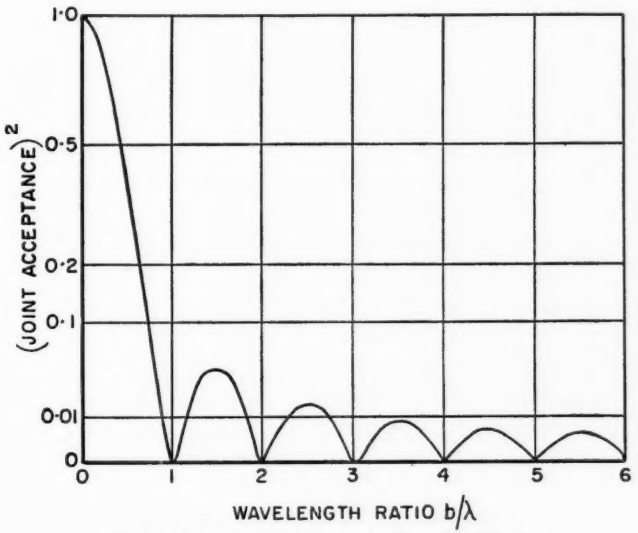

FIGURE 2. Joint acceptance. Rigid panel. Ref. 2.

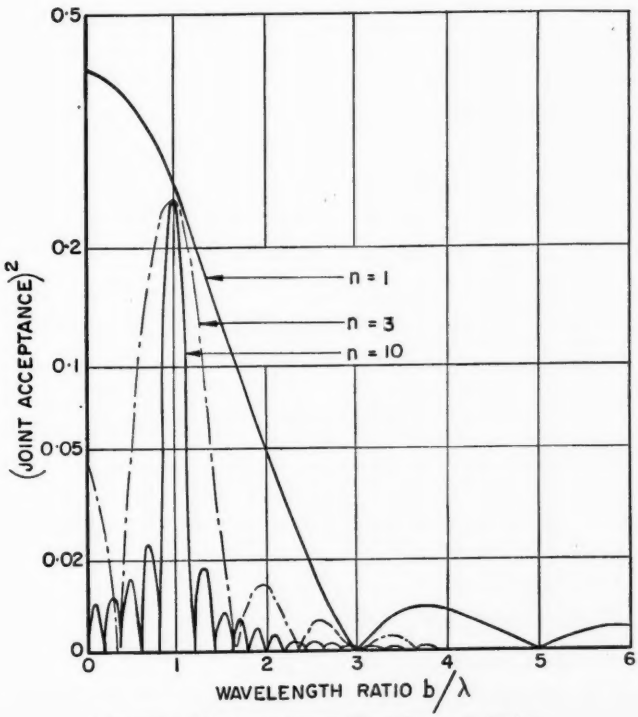

FIGURE 3. Joint acceptance. Flexible panel. Ref. 2.

2.4. Effects of the Surrounding Medium

As the structure vibrates there will be forces exerted upon it by the surrounding air. In general these forces will be made up of two parts; one part in phase with the acceleration, and a second part in phase with the velocity. The component in phase with the acceleration causes a slight increase in the effective mass of the structure, but it is not considered that this will be appreciable in practical cases. The component in phase with velocity gives rise to a damping force due to the fact that the vibrating structure is radiating sound energy. This acoustic damping is considered in detail in Section 4.3.

A third effect which has received little attention, but which may be important in special cases, is due to the effect of the air enclosed within the structure. Foxwell and Franklin[6, 7] have shown that at certain frequencies standing waves can be set up inside a cylinder, thus inhibiting movement of the cylinder walls.

2.5. Simplifications to the General Theory

It is shown in Section 4.3 that the damping of the normal modes is small. Thus the response will be primarily resonant, with only those forces having a frequency close to the natural frequency contributing appreciably to the excitation. As the power spectrum of the noise pressures is relatively flat, the power spectral density in the region of the natural frequency can be assumed to be constant. If it is assumed that $j^2(\omega)$ is also constant in this narrow band of frequencies, then the response equation can be simplified as follows:—

$$\overline{\xi_s^2} = \int_0^\infty \frac{w_L(\omega_s)}{|Y_s(\omega)|^2}\,d\omega = \int_0^\infty \frac{w_{p0}(\omega_s)\,A^2 j_s^2(\omega_s)}{|Y_s(\omega)|^2}\,d\omega$$

$$\simeq A^2 w_{p0}(\omega_s)\,j^2(\omega_s) \int_0^\infty \frac{d\omega}{|Y_s(\omega)|^2}$$

$$\simeq A^2 w_{p0}(\omega_s)\,j^2(\omega_s)\,\frac{\pi}{2c_s k_s} \quad \text{(for resonant response)}$$

$$= A^2 w_{p0}(\omega_s)\,j^2(\omega_s)\,\frac{\pi}{4\delta_s m_s^2 \omega_s^3},$$

where δ_s is the damping ratio.

Therefore the mean square stress

$$\overline{\sigma_s^2} = \frac{\pi A^2}{4\delta_s m_s^2 \omega_s^3}\,w_{p0}(\omega_s)\,j^2(\omega_s)\,h_s^2.$$

As it has been assumed that the damping is small there will be little coupling between the modes of vibration. Thus it can be assumed that the mean square of the total response is equal to the sum of the mean squares of the responses in each separate mode. The mean square of the total stress is therefore

$$\overline{\sigma^2} = \frac{\pi A^2}{4} \sum_{s=1}^{s=n} \frac{w_{p0}(\omega_s)\, \bar{j}^2(\omega_s)\, h_s^2}{\delta_s m_s^2 \omega_s^3}.$$

Thus the r.m.s. stress level in each mode varies directly as the noise pressure level, and the joint acceptance, and varies inversely as the square root of the damping ratio.

Having obtained the r.m.s. stress level and the loading spectrum, fatigue life estimates can be attempted. The effect of randomly varying stresses on fatigue life is not fully understood, but a first approximation can be made by using Miner's "cumulative damage hypothesis." Unfortunately this can be considerably in error for some materials.

3. Noise Pressure Field

3.1. Introduction

It has been shown that both the power spectrum and the spatial correlation of the noise pressures are required to define the exciting forces acting on the structure. The mechanism of noise production by a jet efflux is so complicated that much of this information must be obtained experimentally. Lighthill has developed a theoretical analysis of jet noise in which the sources are assumed to be acoustic quadrupoles formed by the eddies in the turbulent mixing region. The qualitative results of this analysis are supported by tests on model and full-scale jets, but because the exact nature of the turbulence in the jet efflux is not yet known it is not possible to estimate quantitatively the amplitude and correlation of the associated noise pressures. Refs. 6 to 23 discuss the properties of the noise pressure field.

3.2. Power Spectrum of Noise Pressures

3.2.1. *Subsonic Jets: Near Field*

The main sources of noise are the eddies in the mixing region of the jet efflux. The typical size of these eddies is small at positions close to the exit nozzle but increases with increase in distance downstream. The smaller eddies produce noise in the higher frequency range and the larger eddies produce noise in the lower frequency range. The proportion of energy in the eddies which is converted into sound, however, is very small. The eddies will in general have two associated pressure components; one out of phase with velocity, which is the purely hydrodynamic pressure proportional to $\frac{1}{2}\rho V^2$, and a much smaller component, in phase with the velocity, which is radiating sound. Structure close to the jet is thus influenced partly by hydrodynamic pressures and partly by sound pressures. A

further complication is due to the fact that noise components of different frequencies are emanating from different positions in the jet stream. Clearly this position is so complex that it is not possible to estimate analytically the pressure fluctuations on any structure in the near field. Measurements show that for a given jet the pressure amplitudes vary with jet velocity raised to a power of 2 close to the jet and a power of 4 at distances greater than about ten diameters from the jet centre line.

3.2.2. *Subsonic Jets: Far Field*

At some considerable distance away from the jet, the mixing region can be considered to form a point source and therefore the sound waves will be approximately plane. The noise reaching a point in this far field thus takes the form of a randomly varying pressure wave. As would be expected from the composition of the noise source, this random wave has a power spectrum which is relatively flat over a wide range of frequencies. The noise field also shows marked directionality, the maximum total noise intensity occurring along a line making an angle of about 30° to the jet centre line.

Lighthill[16, 17] has developed the general theory of the production of noise by turbulence in the mixing region of a jet efflux. He shows that the noise is produced by a field of acoustic quadrupoles, whose strength depends on the degree of turbulence. Unfortunately the degree of turbulence is not known with any accuracy, but nevertheless the theory establishes the important parameters. It is found that the sound intensity varies typically as the jet velocity raised to the power eight, the so-called V^8 law; and as the square of the exit nozzle diameter. The sound pressure thus varies as V^4. Experimental work on both model and full scale jets[8-13, 18, 20-22] shows that the general character of the noise field agrees with Lighthill's predictions.

3.2.3. *Choked Jets*

The mechanism of noise production by a choked jet is usually complicated by the presence of shock waves in the efflux. Although a convergent-divergent nozzle can be designed to give shock-free flow at one particular operating condition, at other operating conditions shock waves will be formed. The interaction of eddies and hot spots with these shock waves gives off additional sound waves which increase the total noise output of the jet. Richards[20] and Powell[19] have discussed these effects in detail. Vickers Supermarine[22] have confirmed that the noise output of a full-scale jet is considerably increased when the jet is choked. For structural response estimations it will again be necessary to measure experimentally the power spectrum and the spatial correlation of the noise pressures.

3.3. Correlation of Noise Pressures

3.3.1. *Space Correlation*

The next important property of the noise field from the structural response point of view has been shown to be the spatial correlation of the noise pressures

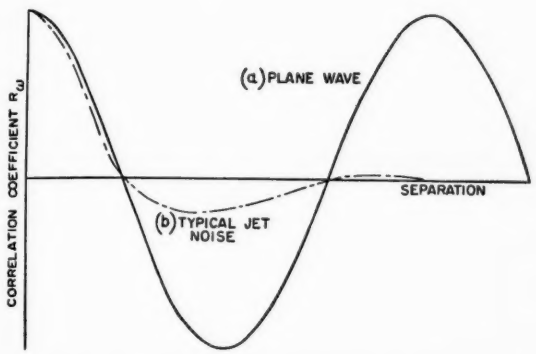

FIGURE 4. Correlogram of sound pressures.

over the structure. This is a measure of the phase relationship between pressures at different points and hence of the effectiveness of the pressure field as an exciting force. Now as the pressure is fluctuating randomly the instantaneous pressures $p(t, a)$ must be replaced by their time-averaged values. Thus the correlation coefficient in the narrow frequency band of central frequency ω becomes

$$R_\omega = \frac{\lim_{T\to\infty}\left[\frac{1}{T}\int_0^T p(t,a)\,p(t,a')\,dt\right]}{\overline{p(t,a_0)^2}}.$$

For discrete frequencies the pressure varies sinusoidally and hence the variation of the correlation coefficient with spatial separation takes the form of a cosine curve as shown in Fig. 4(*a*). In the near field of a jet efflux, however, there are no discrete frequencies and the noise field variation with distance is such that the interdependence between pressures at two points decreases as the spatial separation increases. Consequently the correlogram for the near field of a typical jet takes the form shown in Fig. 4(*b*) with R_ω falling off rapidly to zero. The full curve when extended to negative values of spatial separation is approximately symmetrical, and for practical purposes the distance between the first zero crossing points on either side of the datum represents the distance over which the pressures can be considered to be acting in phase.

Full scale correlation measurements have been made by Callaghan, Howes and Coles[24] on an axial flow turbine of 10,000 lb. thrust rating. Analyses were made in eight frequency bands covering the range 100 c./s. to 1,000 c./s. in a region within 2 to 26 nozzle diameters from the jet exit nozzle. These showed that the size of the region of positive correlation of the overall pressures varied from 0·385 to 0·93 nozzle diameters. Work is being done at Southampton University on a 2 in. diameter model jet to study the mechanism underlying correlation patterns and to make comparisons with full-scale results. Franklin and Foxwell[25, 26] have shown that, for points close to and parallel to the boundary of the jet, the overall correlation can be deduced from the assumption that a fixed noise pattern is convected

downstream at a velocity equal to half the velocity in the centre of the jet. This is confirmed for full-scale jets but only holds for points close to the jet boundary.

3.3.2. *Auto-Correlation*

The auto-correlation coefficient is obtained by multiplying the signal by itself after a time delay τ has been inserted into one channel. It is defined as

$$R_\tau = \frac{\lim_{T\to\infty}\left[\frac{1}{T}\int_0^T p\,(t+\tau)\,p\,(t)\,dt\right]}{\overline{p\,(t)^2}}.$$

Although this is not required directly for structural response calculations it has the important property of being the Fourier transform of the power spectrum of the noise pressure. Thus the power spectral density of the noise pressure can be obtained from the relationship

$$w_p\,(\omega) = \int_0^\infty R_\tau \cos\omega\tau\, d\tau.$$

The variation of R_τ with time delay τ can be measured and the Pegasus digital computer has been programmed to carry out the transform. This provides effectively a narrow band analysis and is thus a more accurate way of obtaining the power spectrum of the noise pressures than the more usual one-third octave filters.

3.3.3. *Measurement of Correlation Coefficients*

The measurement of correlation coefficients can be carried out most conveniently by means of an electronic analogue computer. A general purpose correlator of this type, having a frequency range from 0 to 20 kc./s. has been constructed at Southampton University. The input signals are amplified and pass to a quarter-squares multiplier. A bootstrap integrator integrates the product, which is then finally converted into digital form and registered on a Dekatron counter. The integration time can be any multiple of 10 sec. within the range 10 sec.-10 min. Integration times longer than 10 sec. are achieved by operating two integrators in sequence for 10 sec. periods. The 10 sec. standstill period of each integrator is used to transfer the result to the digital register and to correct for drift by means of a servo-mechanism.

A time delay unit is now in operation with this correlator to enable auto- and cross-correlation measurements to be made. Using a frequency modulated system, the two signals are recorded on widely separated parallel tracks on a rotating magnetic drum. Corresponding reading heads are fixed some little distance round the circumference and one of these heads can be moved relative to the other to introduce a time delay in one of the channels. The two signals then pass to the multiplier and integrator in the normal way.

4. Mechanical Impedance of the Structure

4.1. Introduction

The determination of the mechanical impedance of the structure requires a knowledge of the normal modes and natural frequencies of vibration and also the damping associated with the normal modes. The analysis of the modes and frequencies of vibration of a cylindrical shell of uniform skin thickness has been presented by several authors. The general case of a stiffened shell of the type used in aircraft construction has not been fully analysed, although it is possible to make approximations to the lower modes of vibration. The inherent damping in an aircraft structure is usually low, but this can be increased by the addition of damping materials. As has been shown, any increase in damping reduces the amplitudes of vibration and hence the stress levels in the structure.

4.2. Normal Modes of Vibration

4.2.1. *Uniform Cylinder*

The most comprehensive analysis of the normal modes and natural frequencies of vibration of a cylindrical shell of uniform thickness is due to Arnold and Warburton[27, 28]. Using the strain energy method and Lagrange's equations, they analysed the flexural vibration characteristics of the shell and verified the results by tests on four steel cylinders of different dimensions. For the simply-supported cylinder the mode of vibration is assumed to be made up of sine waves longitudinally and circumferentially. The deflection of any surface element is written

Axial displacement: $u = A \cos n\phi \cos (m\pi x/l)$

Circumferential displacement: $v = B \sin n\phi \sin (m\pi x/l)$

Radial displacement: $w = C \cos n\phi \sin (m\pi x/l)$,

where n is the number of circumferential waves and m is the number of longitudinal half-waves. The lowest root of the frequency equation gives the frequency of the mode having predominantly radial displacement. Curves are given by Arnold and Warburton from which the variation in natural frequency with both n and m can be obtained for four different skin thicknesses. For a relatively thin shell it is found that, for a given value of m, the frequency decreases as n increases, which is contrary to what would have been expected. For thicker shells the reverse trend takes place. These results have been verified by tests on four steel cylinders having internal and external diameters of 3·748 in. and 3·950 in., and lengths ranging from 3·84 in. to 15·63 in.

4.2.2. *Cylinder with Closely Spaced Stiffeners*

Miller[29] has extended the work of Arnold and Warburton to apply to the case of a cylinder stiffened by frame rings and longerons. The spacing of the stiffening material is assumed to be small compared with the mode semi-wavelength in the

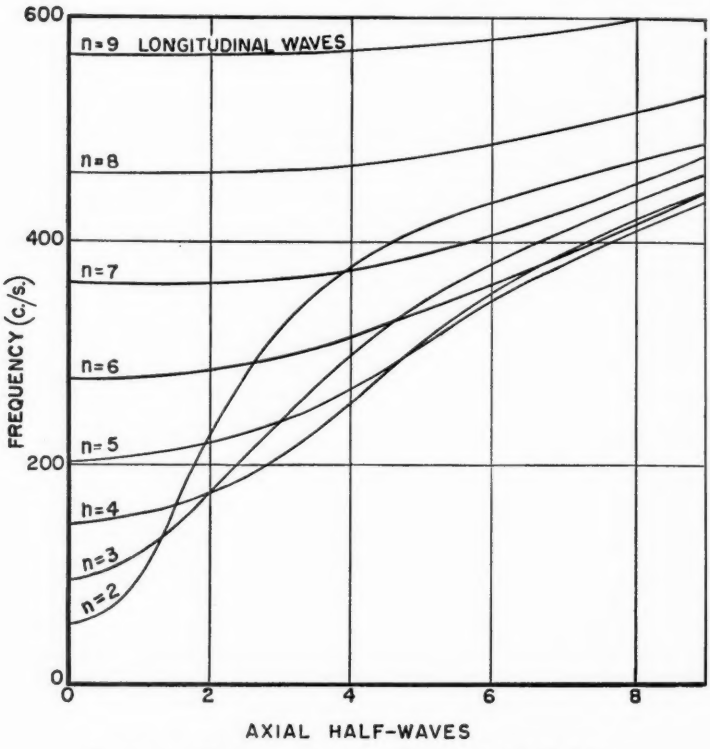

FIGURE. 5. Vibration modes of a stiffened cylinder. Ref. 26.

respective direction. It is then justifiable to assume that the mode shape takes the form of sine waves, as in the previous case. The strain energy and kinetic energy of vibration of the stiffening material are then added on to the energy of the uniform shell. This should give reasonably accurate results for the lower frequencies of a typical aircraft structure. Fig. 5 shows Miller's estimate of the frequency curves for a stiffened cylinder of radius 60 in., skin thickness 0·048 in. and 15 ft. long. The stringer pitch is 8 in. and the frame pitch 20 in. In this case there are only 10 frame rings and 48 longitudinal stiffeners; thus the curves should give reasonable approximations when m is less than 4 and n less than 10. These limiting values, however, need further investigation.

4.2.3. *Cylinder with Widely Spaced Stiffeners*

In cases where the stiffener spacing becomes comparable with the half wavelength in either circumferential or longitudinal directions it is not yet possible to calculate the natural frequencies. For the uniform cylinder, coupling terms between the modes were neglected. It seems probable, however, that these coupling terms assume considerable importance when the stiffener spacing is of the same

order as the mode semi-wavelengths. It is considered possible that the so-called panel and stringer modes, where one panel or stringer on the shell moves a greater amount than corresponding ones, can arise from these coupling effects. Some experimental evidence supports the idea of panel and stringer modes, but no thorough examination has been made.

In practical aircraft structures, using stiffened cylinders, it is probable that over part of the range of frequencies excited by jet noise the modes can be determined sufficiently accurately by assuming closely spaced stiffeners. Over the remainder of the range this approximation breaks down and the modes and frequencies may require experimental investigation.

4.3. Damping of the Normal Modes

4.3.1. *Inherent Structural Damping*

Structural damping results from internal hysteresis of the material of the structure and from energy dissipation at the joints. The predominant effect is usually the damping due to the joints, as the energy loss due to hysteresis in the metal is very small. The damping due to energy dissipation at the joints depends on the normal pressure between the plates, due to forming the rivets, and also on the tangential force loading the joint. On loading the joint a point is reached when the frictional force between the plates is overcome and further increase in load causes slipping of the plates relative to one another. Most of the energy dissipation is due to this slipping. Thus a lightly loaded joint will not dissipate much energy, whereas a more heavily loaded joint is capable of appreciable energy dissipation.

4.3.2. *Methods of Increasing Structural Damping*

The amount of energy dissipated by joints can be increased by the use of a thin insert of damping material if an increase in the joint flexibility can be tolerated. This insert is subjected to a high shear strain, as the joint is loaded. Where the joint is made by adhesives, in the place of rivets, an improvement in the damping can be achieved by choosing an adhesive which is also a good energy absorber.

With an existing structure the damping can be increased by the addition of damping materials, which are essentially layers possessing high energy absorption characteristics. Damping tapes have been used successfully by Vickers Supermarine[22]. Alternatively "anti-drumming" compounds, developed originally for the motor industry, can be sprayed onto the inner surface of the structure. A high polymer type of plastic material is more efficient as an energy absorber than the older bitumen based materials and can be "blended" to give optimum damping over any particular range of temperatures and frequencies. This material is most effective when used on parts of the structure which carry the highest direct strains. Mead[31, 32] has investigated the damping properties of this type of material and studied the effect of damping compounds in general on vibrations excited by jet noise.

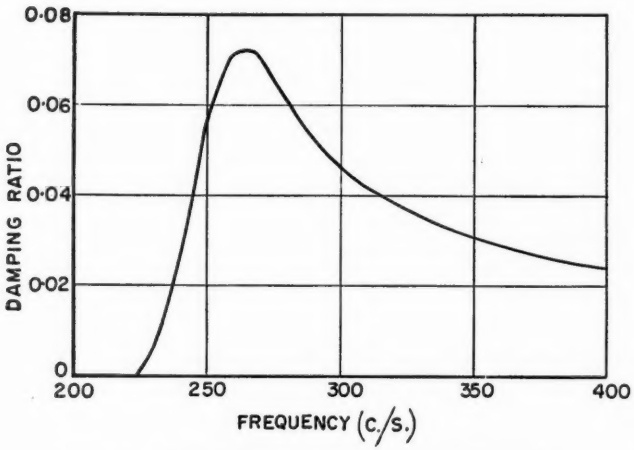

FIGURE 6. Variation in acoustic damping with frequency.

4.3.3. *Acoustic Damping*

Acoustic damping arises from the fact that as the structure vibrates it radiates sound and thus dissipates energy. The magnitude of the acoustic damping depends on the mode and frequency of vibration of the structure. Junger[33] has analysed the case of a long cylinder radiating sound; and from this work a good approximation to the acoustic damping can be made. The cylinder is considered to be vibrating with flexural waves both circumferentially and longitudinally and it is assumed that the cylinder is long compared with the longitudinal wavelength, so that three-dimensional radiation effects at the ends can be neglected. This may not be a severe restriction in practical cases of jet noise excitation.

Typical values of the acoustic damping ratio have been computed for the cylinder discussed in Section 4.2.2. For modes having frequencies in the range 200 c./s.-500 c./s. the damping ratio varied from 0·02 to 0·06. If it were possible to change the frequency of a given mode of vibration, the variation in damping ratio with frequency would take the form shown in Fig. 6. The curve has a marked peak and there is a "cut off" frequency below which no sound is radiated. Radiation does not take place when the structural longitudinal wavelength is less than the sound wavelength. In general it would not be possible to change the frequency of a given mode appreciably on an existing aircraft structure. This work does indicate, however, that in the design stage of a new aircraft it may be possible to achieve high acoustic damping ratios by a suitable choice of structure.

5. Panel Tests

5.1. INTRODUCTION

In the early days of experience of fatigue failure attributable to the action of jet noise, many simple *ad hoc* tests were made in an effort to investigate the problem. Many of these were misleading because they failed to reproduce all the

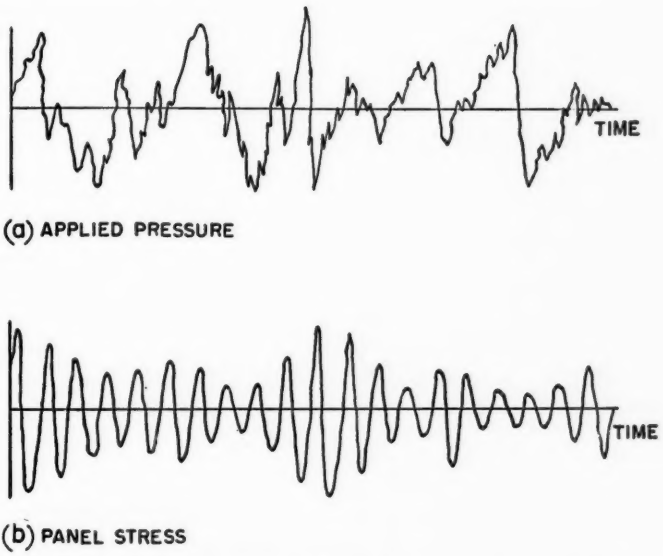

FIGURE 7. Resonant response of a panel to a random pressure wave.

characteristics of the phenomenon. One extensive series of tests, being made primarily in the United States, involves the subjection of single panels to high intensity noise. The panels, having dimensions typical of aircraft fuselage panels, are usually mounted rigidly along their edges. The method of generalised harmonic analysis has been applied to the analysis of panel vibrations by Miles[34]. Subsequently some agreement between theoretical and experimental results has been achieved, but the validity of extrapolating from these tests to complete aircraft structures has not been fully confirmed.

5.2. THEORETICAL ANALYSIS

Miles analyses the case of a panel vibrating in its fundamental mode due to excitation by random noise pressures. The wave of random noise is assumed to impinge normally on the panel; thus the correlation coefficient is equal to unity over the whole panel surface. The damping of this panel mode is small and, therefore, the response is assumed to be essentially resonant. Thus the panel can be considered to respond only to those pressures having frequencies in the range $\omega_0 \pm \delta\omega_0$, where ω_0 is the panel natural frequency, and δ is the damping ratio. The analysis is now simplified and the response takes the form of a vibration of frequency ω_0 but having an envelope which varies randomly, as shown in Fig. 7. The mean square value of the envelope amplitude is given by

$$\overline{\sigma^2} = \frac{\pi}{4\delta}\omega_0 w_p(\omega_0) S_0^2 .$$

$W_p(\omega_0)$ is the power spectral density of the noise pressure at frequency ω_0 and S_0 is the stress at the particular point due to uniform static pressure.

This estimation of r.m.s. stress levels for panel tests gives good agreement with experimental results. The problem of fatigue failure under random loads, however, requires much more investigation before reliable estimates of fatigue lives can be made.

5.3. Experimental Results

Lassiter, Hess and Hubbard[36] have carried out tests on many panels to investigate the fatigue properties of different materials and different forms of construction. Flat panels 11 in. × 13 in., varying in thickness from 0·032 in. to 0·064 in., and curved panels having a radius of curvature of 48 in. were mounted rigidly onto one face of a supporting chamber. High intensity acoustic loading of the panels was obtained by means of a siren or a loudspeaker playing back noise recorded close to an actual jet efflux. The damping of the panels was measured by the resonant amplification method. Stress levels measured on the surface of the panel were found to be in good agreement with predictions based on Miles's method of analysis. The tests were carried on until fatigue failure occurred, but no theoretical estimation of the fatigue life was achieved.

Tests have been made by Vickers Supermarine on panels placed behind an actual jet engine, to investigate the fatigue properties of different types of construction. It was found that the honeycomb sandwich type of construction is much superior to single skin panels. At de Havilland's a limited *ad hoc* test on a complete aircraft[22] indicated that a simplified analysis based on Miles's work and assuming so-called panel and stringer modes could give reasonable agreement with measured r.m.s. stresses. More investigation is required before the general validity of this approach can be established.

5.4. Limitations

The main difficulty with the theoretical work of Miles and the experimental results of Lassiter, Hess and Hubbard and others is that it cannot be reliably used for the prediction of the behaviour of a complete aircraft structure until the validity of such an extrapolation has been established. In the first place the vibration characteristics of a stiffened cylindrical fuselage cannot be represented by a single panel. Secondly, the correlation pattern in the noise field cannot be reproduced by a loudspeaker or siren. A smaller discrepancy may arise from the fact that non-linear vibrations occur in panel tests, as a result of the membrane effect of direct stresses in the middle plane of the panel. Aircraft panels cannot be considered to be rigidly fixed along their edges; consequently non-linearity should not be present to the same extent. It can be concluded, therefore, that panel tests have value in checking the relative strength of different materials and forms of construction from a fatigue point of view; but they can give little indication of the magnitude of that fatigue life on an actual aircraft.

6. Fatigue Life Estimates

6.1. General

It has been seen that, having made certain reasonable assumptions, it is possible to estimate the r.m.s. stress levels in an aircraft structure but it still remains to provide some estimate of the fatigue life of the parts concerned. The effect of random loading on fatigue life has not been fully investigated and the fatigue properties of materials in the low stress range have received little attention in the past. One possible approach is to assume a normal distribution of stress and to use Miner's "cumulative damage hypothesis" to estimate the life under random loading conditions. Tests on simple specimens have indicated that this approach can be in error for low stress levels. Thus it should be emphasised that reliable fatigue life estimates cannot be made at the present stage of knowledge on the subject. In special cases it may be possible to make estimates based on full-scale test experience on a similar structure by using the theory to allow for the effect of structural changes. Much improvement can also be achieved by good detail design of attachments and joints.

6.2. Effect of Random Loading

Freudenthal and Heller[38] have carried out rotating-bending tests on plain polished 2024 and 7075 aluminium alloy specimens using random loading. Their results indicate that the fatigue life under random loading is lower than that predicted by the cumulative damage hypothesis. The specimens were loaded by means of a lever system and an electro-magnet which produced, in a random order, six different stress levels. The stress levels were of an order associated with gust load conditions in an aircraft and not the low stress levels associated with jet noise vibrations. With gust loading, the load cycle is not completely random in sequence, as the highest loads are associated with other high loads in high level turbulence. It is not yet known whether or not this is true in the case of jet noise stresses. Thus the tests using a completely random sequence of loads may be severe.

The difference between the fatigue life achieved, and that predicted by the cumulative damage rule, increased as the r.m.s. stress level decreased for 2024 aluminium alloy. At a characteristic random fatigue life of 10^7 cycles the actual life had been reduced to only 10 per cent of the predicted value. For the 7075 aluminium alloy there was more scatter of results, but the trend was towards a constant ratio of 0·7 between actual and predicted lives. These tests show that the effect of random loading is more severe than is predicted by the cumulative damage rule and also that there is considerable difference in the sensitivity of different materials to random loads.

6.3. Estimates of Fatigue Life Using the Cumulative Damage Rule

In attempting to estimate the fatigue life of a component subjected to randomly varying loads, it would be convenient to be able to express the loading in terms of an effective number of applications of the r.m.s. stress. If cyclic stresses, of magnitude equal to the r.m.s. stress, alone were applied, fatigue failure would occur

in a time $$T = \frac{N'}{f_e} \text{ sec.},$$

where N' = number of applications of r.m.s. stress level required to produce failure

f_e = frequency of r.m.s. stress in c./s.

If now the loading magnitude is varied randomly about this r.m.s. level, the life will be reduced, because stresses greater than r.m.s. value will produce more damage than stresses lower than r.m.s. value. To allow for this Powell[3] introduces the factor η such that

$$T = \frac{\eta N'}{f_e} \text{ for random loading.}$$

Using the cumulative damage rule, assuming a normal distribution of stresses, and a net peak representation of the loading due to Rice[40], Powell shows that

$$\frac{1}{\eta} = \int_0^\infty 2 \frac{N'}{N} y e^{-y^2/2} \, dy$$

where $y^2 = \sigma^2 / \overline{\sigma^2}$

N = number of applications of stress σ to produce failure

and $$f_e = \frac{1}{2\pi} \left[\frac{\int_0^\infty \omega^2 w_\sigma(\omega) \, d\omega}{\overline{\sigma^2}} \right]^{1/2},$$

where $w_\sigma(\omega)$ is the power spectral density of stress at frequency ω.

Thus, when the fatigue curve of the material is known, η and f_e can be estimated for the case of random loading.

However, much more experimental investigation is required to justify this approach.

ACKNOWLEDGMENTS

The author wishes to express his thanks to Professor E. J. Richards for his help and encouragement in the preparation of this paper; to Mr. D. J. Mead and others on whom he has drawn for much of the information which has been included; and to Dr. P. B. Walker and Mr. M. O. W. Wolfe for helpful criticism.

REFERENCES

1. LIEPMANN, H. W. On the Application of Statistical Concepts to the Buffeting Problem. *Journal of the Aeronautical Sciences*, December 1952.
2. POWELL, A. The Problem of Structural Failure due to Jet Noise. A.R.C. 17,514, March 1955.
3. POWELL, A. On the Fatigue Failure of Structures due to Vibrations Excited by Random Pressure Fields. General Theory. A.R.C. 17,925, October 1955.
4. POWELL, A. On Structural Vibrations Excited by Random Pressures. Douglas Report S.M.22795. *To be published.*
5. THOMPSON, W. T. and BARTON, M. V. Response of Mechanical Systems to Random Excitation. *Journal of Applied Mechanics*, July 1957.
6. FOXWELL, J. H. and FRANKLIN, R. E. Acoustic Effects in the Vibrations of Structures. A.R.C. 19,495, August 1957.
7. FOXWELL, J. H., and FRANKLIN, R. E. The Vibrations of a Thin-Walled Stiffened Cylinder in an Acoustic Field. *The Aeronautical Quarterly*, Vol. X, February 1959.
8. RICHARDS, E. J. Research on Aerodynamic Noise from Jets and Associated Problems. *Journal of the Royal Aeronautical Society*, May 1953.
9. POWELL, A. Survey of Experiments on Jet Noise. *Aircraft Engineering*, January 1954.
10. RICHARDS, E. J., GREATREX, F. B., LILLEY, G. M., WARREN, C. H. E., FLEMING, N. and HAYHURST, J. D. Symposium. Aeronautical Acoustics—In Particular Jet Noise. *Journal of the Royal Aeronautical Society*, April 1954.
11. LAURENCE, J. C. Intensity, Scale and Spectra of Turbulence in Mixing Region of Free Subsonic Jet. N.A.C.A. Report 1292, 1956.
12. HUBBARD, H. H. and LASSITER, L. W. Experimental Studies of Jet Noise. *Journal of the Acoustical Society of America*, May 1953.
13. GREATREX, F. B. Jet Noise. Fifth International Aeronautical Congress, Los Angeles, 1955. Institute of the Aeronautical Sciences, 1956.
14. FRANKLIN, R. E. The Estimation of Fluctuating Pressures in the Near Field of a Jet. (Interim Report.) A.R.C. 17,987, November 1955.
15. HOWES, W. L. and MULL, H. R. Near Noise Field of a Jet Engine Exhaust. I. Sound Pressures. N.A.C.A. T.N. 3763, October 1956.
16. LIGHTHILL, M. J. On Sound Generated Aerodynamically, Part I. *Proc. Roy. Soc.*, Vol. 211, A, 1952.
17. LIGHTHILL, M. J. On Sound Generated Aerodynamically, Part II. *Proc. Roy. Soc.*, Vol. 222, A, 1954.
18. GERRARD, J. H. Investigation of Noise Produced by a Subsonic Air Jet. *Journal of the Aeronautical Sciences*, September 1956.
19. POWELL, A. On the Mechanism of Choked Jet Noise. *Proceedings of the Physical Society*, B, 66, p. 1039, 1953.
20. RICHARDS, E. J. Noise Research in the United Kingdom. Canadian Aeronautical Institute Preprint 7/7, May 1957.
21. FOWELL, L. R. and KORBACHER, G. K. Review of Aerodynamic Noise. Institute of Aerophysics, Toronto, Review 8.

22. WOLFE, M. O. W., FRANKLIN, R. E., MEAD, D. J., CLARKSON, B. L. and HETZEL, K. W. Jet Efflux. A Symposium. *Journal of the Royal Aeronautical Society*, February 1957.

23. RICHARDS, E. J., MEAD, D. J., FRANKLIN, R. E., MACLACHLAN, K. R. and others. Notes of the Conference on Aeronautical Acoustics, March 1957. Southampton University. Unpublished.

24. CALLAGHAN, E. E., HOWES, W. L., COLES, W. D., CONGER, C. C. and BERG, D. F. Near Noise Field of a Jet Engine Exhaust. II. Cross Correlation of Sound Pressures. N.A.C.A. T.N. 3764, September 1956.

25. FOXWELL, J. H. and FRANKLIN, R. E. Pressure Fluctuation Near a Cold, Small-Scale Air Jet. A.R.C. 20,182, April 1958.

26. FOXWELL, J. H. and FRANKLIN, R. E. Correlation in the Random Pressure Field Close to a Jet. A.R.C. 20,264, June 1958.

27. ARNOLD, R. N. and WARBURTON, G. B. Flexural Vibrations of the Walls of Thin Cylindrical Shells having Freely Supported Ends. *Proc. Roy. Soc.*, Vol. 197, 1949.

28. ARNOLD, R. N. and WARBURTON, G. B. Flexural Vibrations of Thin Cylinders. *Proceedings of the Institution of Mechanical Engineers* (A), Vol. 167, 1953.

29. MILLER, P. R. Free Vibrations of a Stiffened Cylindrical Shell. A.R.C. 19,338, May 1957.

30. MEAD, D. J. The Internal Damping due to Structural Joints. A.R.C. 19,870, January 1958.

31. MEAD, D. J. The Effect of a Damping Compound on Jet Efflux Excited Vibrations. Part I: The Structural Damping due to the Compound. A.R.C. 20,155, July 1958.

32. MEAD, D. J. The Effect of a Damping Compound on Jet Efflux Excited Vibrations. Part II: The Reduction of Vibration and Stress Level due to the Compound. A.R.C. 20,263, November 1958.

33. JUNGER, M. C. The Outgoing Wave in Cylindrical Co-ordinates. *Journal of the Acoustical Society of America*, Vol. 25, 1953.

34. MILES, J. W. Structural Fatigue under Random Loading. *Journal of the Aeronautical Sciences*, November 1954.

35. ERINGEN, A. C. Response of Beams and Plates to Random Loads. *Journal of Applied Mechanics*, March 1957.

36. LASSITER, L. W., HESS, R. W. and HUBBARD, H. H. Experimental Study of the Response of Simple Panels to Intense Acoustic Loading. *Journal of the Aeronautical Sciences*, January 1957.

37. KIRCHMANN, E. J. and GREENSPON, J. E. Non-Linear Response of Aircraft Panels in Acoustic Noise. *Journal of the Acoustical Society of America*, July 1957.

38. FREUDENTHAL A. M. and HELLER, R. A. Accumulation of Fatigue Damage. Presented at the Conference, *Fatigue in Aircraft Structures*, Columbia University, 1956. Academic Press Inc., New York.

39. MINER, M. A. Cumulative Damage in Fatigue. *Journal of Applied Mechanics*, Vol. 12, 1945.

40. RICE, S. O. Mathematical Analysis of Random Noise. *Bell System Technical Journal*, Vol. 24, 1945.

Note on the Forces that Act near the Centre and the Tips of a Swept-Back Wing

D. G. HURLEY

(*Aeronautical Research Laboratories, Melbourne*)

SUMMARY: The momentum equation is used to calculate the drag that acts near the tip of a semi-infinite swept-forward wing of constant chord that is at zero incidence to a uniform stream of incompressible, inviscid fluid. The drag is given as a function of wing section and angle of sweep and is shown to be unaffected by shaping the tip. The results may be used to calculate the drag that acts near the centre and the thrusts that act near the tips of a swept-back wing, provided that its aspect ratio is sufficiently great for the regions where the different forces act to be separated. Some results due to Neumark and to Küchemann and Weber suggest that this will be so provided that the aspect ratio is greater than about two. The results are combined with some due to these authors to estimate the spanwise extent of the forces. It is found that this extent decreases as the angle of sweep is increased and that it depends quite markedly on the wing section.

1. Introduction

The low speed potential flow about untapered non-lifting swept wings has been considered by Neumark[1] and by Küchemann and Weber[2]. One of their findings was that wing sections near the plane of symmetry experience quite large drag forces, whereas sections near the tip experience balancing thrusts. They also found that when the aspect ratio is greater than about two the regions where these forces act are separated by ones where the flow is very nearly the same as that about the corresponding swept wing of infinite span—a flow in which the force per unit span is zero.

These findings suggested that it should be possible to use either the energy or the momentum equation to calculate the drag and thrust forces in these cases and this paper shows how this can be done.

The results are useful, since the approximate method used by the authors referred to is more suited to calculating the drag that acts *at* the centre section rather than the total drag that acts *near* the centre section, which is given quite simply by the present method.

It is convenient to introduce the method by considering the flow about a semi-infinite swept-forward wing.

Received June 1958.

NOTATION

$\mathbf{a}$ unit vector in direction of $\mathbf{V}_0$

c chord measured normal to leading edge

C contour of wing section described in positive sense

$C_D = D/(\frac{1}{2}\rho V_0^2 c^2)$, drag coefficient of tip of semi-infinite swept-forward wing cut off by plane normal to leading edge

$C_{D'} = D'/(\frac{1}{2}\rho V_0^2 c^2)$, drag coefficient of tip of semi-infinite swept-forward wing cut off by vertical plane containing $\mathbf{V}_0$

$c_{d_c} = d_c/(\frac{1}{2}\rho V_0^2 c)$, drag coefficient of wing section at centre of swept wing

D drag of tip of semi-infinite swept-forward wing cut off by plane normal to leading edge

D' drag of tip of semi-infinite swept-forward wing cut off by vertical plane containing $\mathbf{V}_0$

D_t drag of triangular portion of wing (*see* Fig. 3 on p. 136)

d_c drag force per unit span that acts on wing section at centre of swept wing

$\mathbf{F}$ resultant force on wing tip

L one half edge length of cube (*see* Fig. 1)

m source strength

p fluid pressure

p_0 free stream pressure

S surfaces of cube excluding S_1 (*see* Fig. 1)

S_1 cross-sectional area of wing section (*see* Fig. 1)

t thickness of wing

u_x, u_z perturbation velocity components of two-dimensional motion past wing section when speed at infinity is unity

$\mathbf{V}, V$ fluid velocity and speed, respectively

$\mathbf{V}_0, V_0$ free stream velocity and speed, respectively

V_x, V_y, V_z components of fluid velocity

v_x, v_y, v_z perturbation velocity components (*see* equation (1))

x, y, z rectangular co-ordinates { x normal to leading edge, y along leading edge from tip, z vertically upwards (*see* Fig. 1)

x' co-ordinate measured in direction of V_0

β angle of yaw (*see* Fig. 6)

λ angle of sweep

μ doublet strength (*see* equation (6))

ρ fluid density

ϕ_2 velocity potential: $u_x = -\partial\phi_2/\partial x$, $u_z = -\partial\phi_2/\partial z$

ψ_2 stream function corresponding to ϕ_2

2. The Semi-Infinite Swept-Forward Wing

Consider the low speed potential flow about a semi-infinite untapered wing of symmetrical section which is swept forward through an angle λ and which is at zero incidence to a stream of speed V_0 (*see* Fig. 1).

Let $Oxyz$ be a set of rectangular axes with O at the tip and Oy along the leading edge. Ox lies in the chordal plane of the wing and Oz is vertically upwards. Let V_x, V_y, V_z be the components of the fluid velocities and let v_x, v_y, v_z be the perturbation velocity components, so that

$$\left.\begin{aligned} V_x &= V_0 \cos\lambda + v_x \\ V_y &= V_0 \sin\lambda + v_y \\ V_z &= v_z \end{aligned}\right\} \quad . \quad . \quad . \quad . \quad . \quad . \quad (1)$$

The momentum equation is applied to the fluid which lies within the large cubic control surface S shown in Fig. 1, and this gives

$$\mathbf{F} = -\int\int_S p\, d\mathbf{S} - \int\int_S \rho \mathbf{V}\,(\mathbf{V} \cdot d\mathbf{S}) \quad . \quad . \quad . \quad . \quad (2)$$

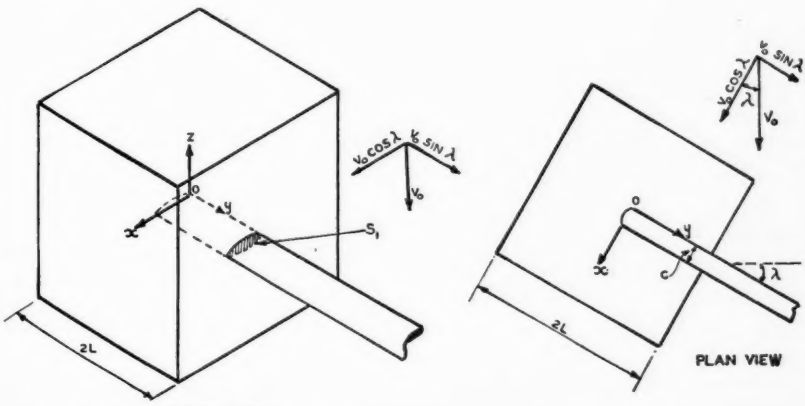

FIGURE 1. Semi-infinite swept-forward wing, showing control surface and notation.

Here **F** is the force acting on the portion of the wing inside the cube, $d\mathbf{S}$ is a vector element of surface area in the direction of the outward normal to S and **V** is the fluid velocity.

Now, by Bernoulli's equation,

$$\begin{aligned} p &= p_0 + \tfrac{1}{2}\rho V_0^2 - \tfrac{1}{2}\rho V^2 \\ &= p_0 + \tfrac{1}{2}\rho V_0^2 - \tfrac{1}{2}\rho\{(V_0\cos\lambda + v_x)^2 + (V_0\sin\lambda + v_y)^2 + v_z^2\}, \quad \text{from equation (1)} \\ &= p_0 - \rho V_0 (v_x\cos\lambda + v_y\sin\lambda) - \tfrac{1}{2}\rho (v_x^2 + v_y^2 + v_z^2). \quad . \quad . \quad . \quad . \quad . \quad (3) \end{aligned}$$

Substitution into equation (2), and taking the scalar product with a unit vector **a** in the direction of $\mathbf{V}_0$, gives

$$D = -p_0\mathbf{a}\cdot\iint_S d\mathbf{S} + \rho\iint_S (v_x\cos\lambda + v_y\sin\lambda)\, V_0\mathbf{a}\cdot d\mathbf{S} +$$

$$+ \tfrac{1}{2}\rho\iint_S (v_x^2 + v_y^2 + v_z^2)\,\mathbf{a}\cdot d\mathbf{S} - \rho\iint_S \mathbf{V}\cdot\mathbf{a}\,(\mathbf{V}\cdot d\mathbf{S}),$$

where D is the component of **F** in the direction of $\mathbf{V}_0$.

Since $\mathbf{V}\cdot\mathbf{a} = V_x\cos\lambda + V_y\sin\lambda$

$$= V_0 + v_x\cos\lambda + v_y\sin\lambda, \quad \text{from equation (1)},$$

$$D = -p_0\,\mathbf{a}\cdot\iint_S d\mathbf{S} + \rho\iint_S (v_x\cos\lambda + v_y\sin\lambda)\ \mathbf{V}\cdot d\mathbf{S} +$$

$$+ \tfrac{1}{2}\rho\iint_S (v_x^2 + v_y^2 + v_z^2)\,\mathbf{a}\cdot d\mathbf{S} - \rho\iint_S (V_0 + v_x\cos\lambda + v_y\sin\lambda)\,(\mathbf{V}\cdot d\mathbf{S})$$

$$= -p_0\,\mathbf{a}\cdot\iint_S d\mathbf{S} + \rho\iint_S (v_x\cos\lambda + v_y\sin\lambda)\,(\mathbf{V}_0 - \mathbf{V})\cdot d\mathbf{S} +$$

$$+ \tfrac{1}{2}\rho\iint_S (v_x^2 + v_y^2 + v_z^2)\,\mathbf{a}\cdot d\mathbf{S} - \rho V_0\iint_S \mathbf{V}\cdot d\mathbf{S}. \quad . \quad . \quad (4)$$

Now since the surface S excludes the surface S_1 where the wing protrudes through the cube,

$$\mathbf{a}\cdot\iint_S d\mathbf{S} = -S_1\sin\lambda,$$

so that the first term on the right hand side of equation (4) is $p_0 S_1\sin\lambda$. The last

term on the right hand side is zero because $\iint_S \mathbf{V} \cdot d\mathbf{S}$ is the total flux of fluid across S, which is zero.

Thus equation (4) becomes

$$D = p_0 S_1 \sin\lambda + \rho \iint_S (v_x \cos\lambda + v_y \sin\lambda)(\mathbf{V}_0 - \mathbf{V}) \cdot d\mathbf{S} + \tfrac{1}{2}\rho \iint_S (v_x^2 + v_y^2 + v_z^2)\,\mathbf{a} \cdot d\mathbf{S}. \quad . \quad . \quad . \quad (5)$$

The limit of this equation as $L \longrightarrow \infty$ is considered, where L is half the edge length of the cube. It is assumed that the velocity perturbations at large distances from the wing can be considered as arising from a semi-infinite line doublet of strength μ lying along the positive y-axis and a source of strength m at the origin. With these assumptions it can be shown that

$$\left.\begin{aligned} v_x &= \frac{\mu(z^2-x^2)}{(x^2+z^2)^2}\left\{1+\frac{y}{(x^2+y^2+z^2)^{1/2}}\right\} - \frac{\mu x^2 y}{(x^2+z^2)(x^2+y^2+z^2)^{3/2}} + \frac{mx}{(x^2+y^2+z^2)^{3/2}} \\ v_y &= \frac{\mu x}{(x^2+y^2+z^2)^{3/2}} + \frac{my}{(x^2+y^2+z^2)^{3/2}} \\ v_z &= \frac{-2\mu xz}{(x^2+z^2)^2}\left\{1+\frac{y}{(x^2+y^2+z^2)^{1/2}}\right\} - \frac{\mu xyz}{(x^2+z^2)(x^2+y^2+z^2)^{3/2}} + \frac{mz}{(x^2+y^2+z^2)^{3/2}} \end{aligned}\right\} \quad . \quad . \quad . \quad . \quad (6)$$

This equation shows that v_x, v_y and v_z are $O(1/L^2)$ on all the faces of the cube other than the face $y = +L$. On this face v_y is $O(1/L^2)$ but v_x and v_z are not. Also, on this face,

$$(\mathbf{V}_0 - \mathbf{V}) \cdot d\mathbf{S} = -v_y\, dS,$$

so that the limit as $L \longrightarrow \infty$ of equation (5) is

$$D = p_0 S_1 \sin\lambda + \tfrac{1}{2}\rho \iint_\infty (v_x^2 + v_z^2)\,\mathbf{a} \cdot d\mathbf{S}$$

$$= p_0 S_1 \sin\lambda + \tfrac{1}{2}\rho \sin\lambda \iint_\infty (v_x^2 + v_z^2)\, dS, \quad . \quad . \quad . \quad (7)$$

where the region of integration extends over the whole of the xz-plane, at $y = +\infty$. It is evident* that, as $y \longrightarrow +\infty$, v_x and v_z approach the values for the two-dimensional flow about the wing section when the speed at infinity is $V_0 \cos\lambda$.

*The replacement of the wing by a semi-infinite line doublet (and a source), as has been done, is nearly equivalent to replacing it by a semi-infinite circular cylinder. On the face $y = +L$ the values of v_x and v_z given by equation (6) differ from the two-dimensional values for a circular cylinder only by quantities which are $O(1/L^2)$.

If u_x and u_z denote these two-dimensional velocity perturbations when the speed at infinity is unity, then, as $y \longrightarrow +\infty$,

$$v_x \longrightarrow u_x V_0 \cos\lambda$$
$$v_z \longrightarrow u_z V_0 \cos\lambda,$$

so that equation (7) becomes

$$D = p_0 S_1 \sin\lambda + \tfrac{1}{2}\rho V_0^2 \sin\lambda \cos^2\lambda \int\int_{\infty} (u_x^2 + u_z^2)\, dS. \quad . \quad . \quad (8)$$

Now $$\int\int_{\infty} (u_x^2 + u_z^2)\, dS = \oint_C \phi_2 d\psi_2, \quad . \quad . \quad . \quad . \quad (9)$$

(Ref. 3, p. 66), where ϕ_2 and ψ_2 are the velocity potential and stream function corresponding to the perturbation velocity components u_x and u_z and C is the contour of the wing section. Thus equation (8) becomes

$$C_D = \frac{D}{\tfrac{1}{2}\rho V_0^2 c^2} = \frac{p_0 S_1 \sin\lambda}{\tfrac{1}{2}\rho V_0^2 c^2} + \frac{\sin\lambda \cos^2\lambda}{c^2} \oint_C \phi_2 d\psi_2. \quad . \quad . \quad (10)$$

This equation is the same as equation (9) of Ref. 4, which was derived using the energy equation.

3. Physical Interpretation of Equation (8)

If the whole of the wing surface were subject to a uniform pressure p_0, then the component of the force acting on the wing in the direction of $\mathbf{V}_0$ would be $p_0 S_1 \sin\lambda$, which is the first term on the right hand side of equation (8). It is thus seen that this term represents a buoyancy type force and is of little interest.

To obtain a physical interpretation of the second term on the right hand side, it is convenient to multiply the equation by V_0 and to consider the motion as arising from the wing's being advanced through fluid which is at rest at large distances from it. The left hand side is then equal to the rate at which work must be done to produce the motion.

A cubic control surface is again introduced, but it is now considered to be at rest, so that the length of wing inside the cube is increasing at a rate $V_0 \sin\lambda$. The second term on the right hand side of equation (8) (multiplied by V_0) can be written

$$\{V_0 \sin\lambda\} \times \left\{ \tfrac{1}{2}\rho \int\int_{\infty} \left[(u_x V_0 \cos\lambda)^2 + (u_z V_0 \cos\lambda)^2 \right] dS \right\}.$$

The second factor in this expression is the kinetic energy of the fluid per unit span of wing where it protrudes from the cube (the y velocity component being now

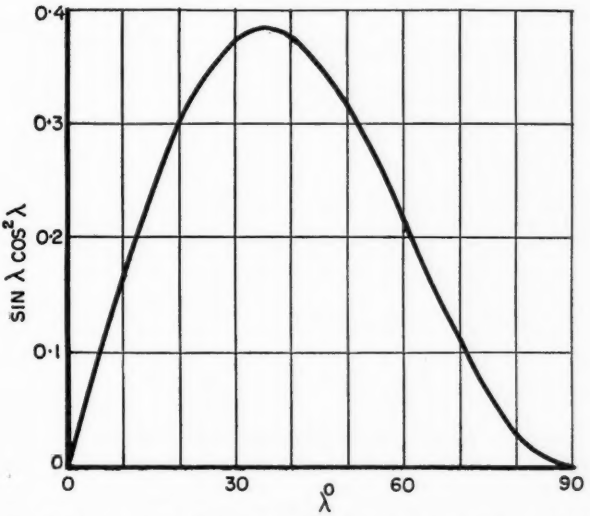

FIGURE 2. Variation of tip drag of swept-forward wing with angle of sweep.

zero). Thus the expression is the rate at which the fluid inside the fixed cube is gaining kinetic energy and, as remarked previously, the left hand side of the equation represents the rate at which work must be done to generate the motion.

4. Dependence of C_D on Angle of Sweep and Wing Section

Equation (10) shows that, apart from a buoyancy type force, C_D varies as $\sin\lambda\cos^2\lambda$ for all wing sections and this function is shown in Fig. 2. It is zero for $\lambda=0°$ and 90° and has a maximum when $\lambda=35°\ 16'$.

The effect of differing wing sections was investigated by evaluating

$$\frac{1}{c^2}\oint_C \phi_2 d\psi_2$$

for a number of standard aerofoil sections, using the ordinates and surface velocities given in Ref. 5.

ϕ_2 was obtained by numerical integration from

$$\phi_2 = -\int_0^s (u_x^2+u_z^2)^{1/2} ds, \quad . \quad . \quad . \quad . \quad . \quad (11)$$

where s is the distance measured around the surface of the aerofoil from its leading edge.

ψ_2 is given by $\psi_2 = -z(x)$, ... (12)

where $z = z(x)$ is the aerofoil profile (Ref. 3, p. 83).

$$\frac{1}{c^2} \oint_C \phi_2 d\psi_2$$

was evaluated numerically, using the values of ϕ_2 and ψ_2 given by equations (11) and (12). The results are given in Table I, which also contains the exact value for an elliptic section, $(\pi/4)/(t/c)^2$ (Ref. 3, p. 85).

Approximate calculations were also made for the biconvex section

$$z(x) = 2\frac{t}{c}\frac{x}{c}(c-x), \qquad 0 \leqslant x \leqslant c, \quad . \quad . \quad . \quad (13)$$

which is considered extensively in Refs. 1 and 2.

Equation (2.4) of Ref. 2 is, with $c=1$ and $V_0=1$,

$$u_x = \frac{1}{\pi}\int_0^1 \frac{dz(x')}{dx'}\frac{dx'}{x-x'} \quad . \quad . \quad . \quad . \quad . \quad . \quad (14)$$

$$\text{which gives} \quad u_x = \frac{2}{\pi}\frac{t}{c}\left\{2 + (2x-1)\log_e\left(\frac{1-x}{x}\right)\right\} \quad . \quad . \quad . \quad (15)$$

To the same degree of approximation as is involved in equation (14), ϕ_2 may be evaluated from

$$\phi_2 = -\int_0^x u_x(x')\,dx' \quad . \quad . \quad . \quad . \quad . \quad (16)$$

which gives, using equation (15),

$$\phi_2 = -\frac{2}{\pi}\frac{t}{c}\left\{x + x\log_e x - (1-x)\log_e(1-x) - x^2\log_e x + (1-x)^2\log_e(1-x)\right\}.$$

It then follows from equations (12), (13) and (16) that

$$\frac{1}{c^2}\oint_C \phi_2 d\psi_2 = \frac{2}{\pi}\left(\frac{t}{c}\right)^2 \quad . \quad . \quad . \quad . \quad . \quad (17)$$

a value which is included in Table I.

TABLE I

Wing Section	$\frac{1}{c^2}\oint_C \phi_2\, d\psi_2$	$\frac{\frac{1}{c^2}\oint_C \phi_2\, d\psi_2}{(t/c)^2}$
N.A.C.A. 63-010	0·00667	0·667
64-010	0·00656	0·656
65-010	0·00673	0·673
66-010	0·00693	0·693
65-006	0·00243	0·676
65-008	0·00429	0·670
Ellipse	$\frac{\pi}{4}\left(\frac{t}{c}\right)^2$	$\frac{\pi}{4}=0{\cdot}785$
Biconvex (equation (13))	$\frac{2}{\pi}\left(\frac{t}{c}\right)^2$	$\frac{2}{\pi}=0{\cdot}637$

The first four aerofoils listed in Table I are each 10 per cent thick, but differ in the location of the point of maximum thickness. The table shows that this has little effect on the drag. The third, fifth and sixth aerofoils have similar thickness distributions but different values of t/c. The third column shows that the drag varies almost exactly as $(t/c)^2$, which is also seen to be the case for elliptic and biconvex sections. The table also shows that, for a given value of t/c, an ellipse gives a larger value of the drag than the other sections.

5. Wing Tips Cut Off in Direction of $\mathbf{V}_0$ Instead of Normal to Leading Edge

To enable comparisons to be made with the results of Refs. 1 and 2, it is necessary to consider the case when the wing tip is cut off by a vertical plane which contains $\mathbf{V}_0$ and not by a plane which is normal to the leading edge, as has been the case so far.

If D' is the drag that acts in the former case, then

$$D' = D + D_t, \quad . \quad . \quad . \quad . \quad . \quad . \quad (18)$$

where D_t is the drag that acts on the triangular portion of wing shown in Fig. 3.

From this figure,

$$D_t = 2\cos\lambda \int_0^c px \tan\lambda \frac{dz}{dx}\, dx$$

$$= 2\sin\lambda \int_0^c px \frac{dz}{dx}\, dx. \quad . \quad . \quad . \quad . \quad . \quad (19)$$

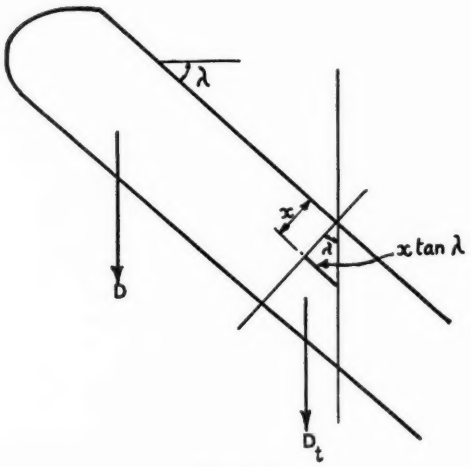

FIGURE 3.

When the triangular portion of wing under consideration is sufficiently remote from the tip for the surface pressures to be the same as for a swept wing of infinite aspect ratio, the use of Bernoulli's equation leads to

$$D_t = 2 \sin \lambda \int_0^c \left\{ p_0 - \frac{1}{2} \rho V_0^2 \cos^2 \lambda (2u_x + u_x^2 + u_z^2) \right\} x \frac{dz}{dx} dx.$$

$$= -p_0 S_1 \sin \lambda - \rho V_0^2 \sin \lambda \cos^2 \lambda \int_0^c (2u_x + u_x^2 + u_z^2) x \frac{dz}{dx} dx,$$

since $$-2 \int_0^c x \frac{dz}{dx} dx = S_1,$$

the cross-sectional area of the profile, so that, from equations (8) and (18),

$$D' = \frac{1}{2} \rho V_0^2 \sin \lambda \cos^2 \lambda \int_\infty \int (u_x^2 + u_z^2) \, dS - \rho V_0^2 \sin \lambda \cos^2 \lambda \int_0^c (2u_x + u_x^2 + u_z^2) x \frac{dz}{dx} dx. \quad . \quad . \quad . \quad . \quad (20)$$

It is shown in the Appendix that the linear theory approximation to the second term on the right hand side of this equation is zero for all profiles. It can also be shown*, using the results of Ref. 6, p. 160, for example, that the term is exactly zero

*The calculations are not included as they are straightforward, although lengthy.

for the case of elliptic profiles. The term was also evaluated numerically for the N.A.C.A. 65-010 profile, using the data of Ref. 5, and once again the result was, to within the accuracy of the calculations, zero.

Although no proof that it is exactly zero in the general case was found, the preceding results suggest that it can be neglected in practice, so that equation (20) can be written in coefficient form

$$C_{D'} = \frac{D'}{\frac{1}{2}\rho V_0^2 c^2} = \frac{\sin\lambda \cos^2\lambda}{c^2} \int\int_{\infty} (u_x^2 + u_z^2)\, dS$$

$$= \frac{\sin\lambda \cos^2\lambda}{c^2} \oint_C \phi_2 d\psi_2, \qquad (21)$$

using equation (9).

6. Application of Results to Swept Wings of Finite Aspect Ratio and Other Cases

Consider a swept wing of large aspect ratio, as shown in Fig. 4. Now if the aspect ratio is sufficiently large, then the flow near the tips will not be influenced by the distortion to the flow produced by the kinked centre section, and the preceding analysis may be used (with the sign of λ changed) to calculate the net force in the direction of $\mathbf{V}_0$ that acts on each of the tips. Equation (21) shows that each force will be a thrust and, since the total force that acts on the complete wing must be zero, it follows that there will be a drag force acting on the central portion which, in coefficient form, will be of magnitude $2C_{D'}$, with $C_{D'}$ given by equation (21).

An idea of how large the aspect ratio must be for this separation of the forces to apply can be obtained from some calculations carried out by Neumark[1]. He

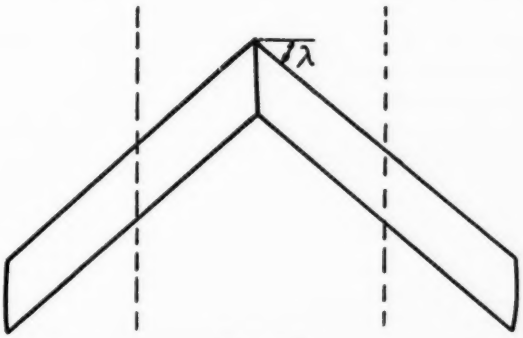

FIGURE 4.

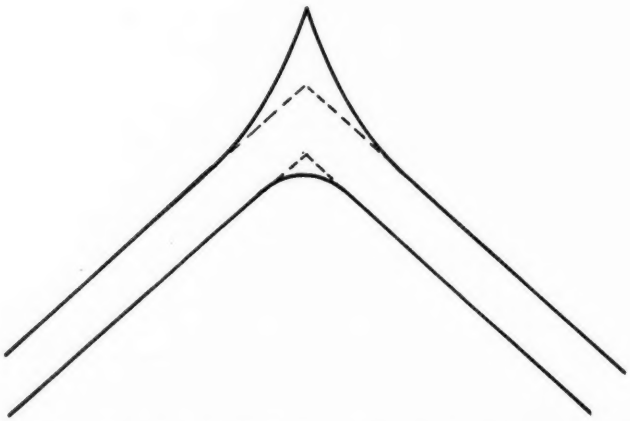

FIGURE 5. Swept wing differing from one of constant chord section and sweep only near centre.

considered a biconvex wing of aspect ratio 2 having 53° 8′ sweep and found that, even for this small aspect ratio, the velocity field inboard of mid-semi-span was nearly the same as when the aspect ratio is infinite. It thus appears that if the aspect ratio is greater than about 2 it is legitimate to treat the central and tip portions of the wing separately and to apply the preceding analysis. Some further comments on this are made in Section 8.

The preceding results may also be applied to a wing of infinite aspect ratio whose shape departs from one of constant chord, sweep and section only near the centre (*see* Fig. 5). For the disturbances to the "infinite aspect ratio flow" at sections of the wing remote from the centre may be represented by a certain distribution of doublets, and these disturbances will die out sufficiently rapidly for the preceding analysis to apply. It is thus seen that the total drag force that acts near the centre section of a swept wing of large aspect ratio cannot be reduced by changing the sections near the centre. This remark, of course, applies only to low speed flow and not to transonic flow.

The present method can also be used to treat the case of a wing which is swept through an angle λ and also yawed through an angle β (Fig. 6). The thrusts acting on the port and starboard tips will be given by equation (21) with λ replaced by $-\lambda+\beta$ and $-\lambda-\beta$ respectively. The drag force acting near the centre will be numerically equal to the sum of the two tip thrusts.

7. The Results of Neumark[1] and of Küchemann and Weber[2]

These authors have calculated the flow that occurs near the centre of a swept wing of infinite aspect ratio by a method in which the wing is replaced by a system of kinked sources. Küchemann and Weber obtained the following expression for the drag coefficient of the central *section* (*see* equations (3.13) and (3.26) of Ref. 2).

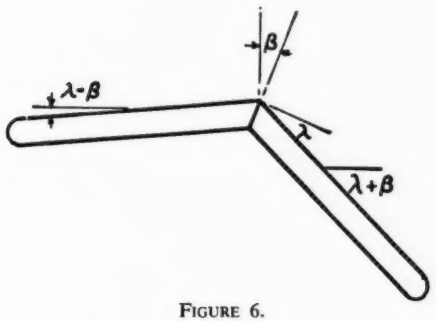

FIGURE 6.

$$c_{d_c} = \frac{d_c}{\frac{1}{2}\rho V_0^2 c} = \frac{4}{\pi}\log_e\left(\frac{1+\sin\lambda}{1-\sin\lambda}\right)\int_0^{c/\cos\lambda}\left(\frac{dz'}{dx'}\right)^2 \frac{dx'}{\{1+(dz'/dx')^2\}^{1/2}}, \quad . \quad (22)$$

where $z' = z'(x'), \quad 0 \leqslant x' \leqslant \frac{c}{\cos\lambda}$,

is the wing profile in the direction of $\mathbf{V}_0$.

To obtain the value of $2C_{D'}$, the total drag that acts near the centre, it is necessary to know the values of the local drag at sections of the wing other than the central one and then to integrate across the span. This involves lengthy numerical calculations which appear to have been carried out only for the biconvex section of equation (13). Figure 12 of Ref. 2 gives results when $\lambda = 45°$ and Fig. 19 of Ref. 1 gives results when $\lambda = 53° 8'$.

For the biconvex section, equation (22) gives

$$c_{d_c} = \frac{16}{3\pi}\left(\frac{t}{c}\right)^2 \cos^2\lambda \log_e\left(\frac{1+\sin\lambda}{1-\sin\lambda}\right) + O\left(\frac{t}{c}\right)^4 \quad . \quad . \quad . \quad . \quad (23)$$

and by numerical integration of the two figures just referred to it is found that

$$2C_{D'} = 0{\cdot}42\,(t/c)^2 \quad \text{for } \lambda = 45°$$

$$\text{and } = 0{\cdot}37\,(t/c)^2 \quad \text{for } \lambda = 53° 8'.$$

The values of $2C_{D'}$ given by the present method (equations (21) and (17)) are

$$0{\cdot}45\,(t/c)^2 \quad \text{for } \lambda = 45°$$

$$\text{and } \quad 0{\cdot}37\,(t/c)^2 \quad \text{for } \lambda = 53° 8',$$

which are seen to agree reasonably well with the results of the other authors.

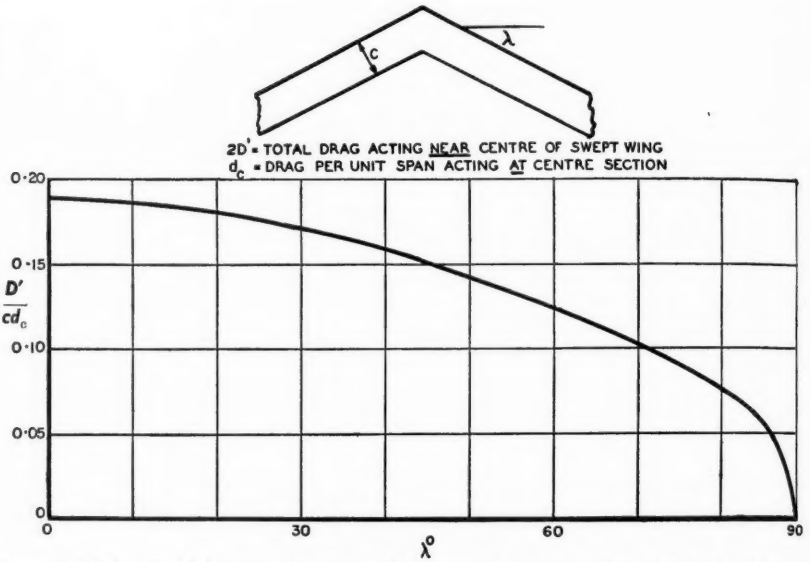

FIGURE 7. Estimates of the spanwise extent of the central drag force for wing having biconvex sections.

8. The Spanwise Extent of the Drag Force that Acts Near the Centre of a Swept Wing

As remarked in the previous section, it is only for swept wings of biconvex section that the method of Refs. 1 and 2 has been used to calculate the flow at sections other than the centre one, so that knowledge of the spanwise extent of the region where the drag acts is very meagre. Additional information can be obtained by calculating the ratio D'/d_c, which has the dimensions of length and is a measure of the spanwise extent of the region where the drag acts.

For the biconvex section, equations (17), (21) and (23) give

$$\frac{D'}{d_c} = \frac{3}{8} \frac{c \sin \lambda}{\log_e\left(\frac{1+\sin\lambda}{1-\sin\lambda}\right)} + O\left(\frac{t}{c}\right)^2$$

and the main term is seen to be independent of t/c.

Figure 7 gives the values of $D'/(cd_c)$ and it is seen that this decreases as λ is increased.

For wings having elliptic sections, equation (21) and Table I give

$$D' = \tfrac{1}{2}\rho V_0^2 c^2 \sin\lambda \cos^2\lambda \frac{\pi}{4}\left(\frac{t}{c}\right)^2,$$

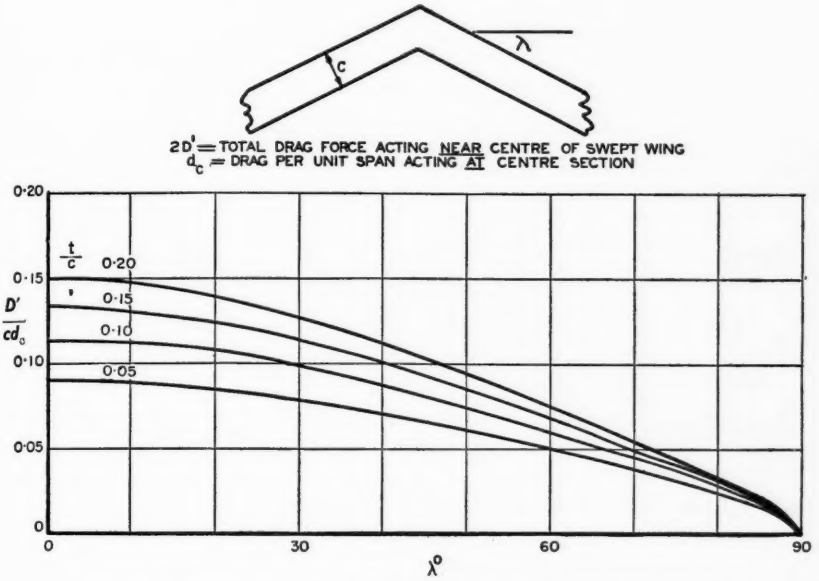

FIGURE 8. Estimates of the spanwise extent of the central drag force for wings having elliptic sections.

and equation (3.28) of Ref. 2 gives*

$$d_c = \tfrac{1}{2}\rho V_0^2 c \cos^2\lambda \log_e\left(\frac{1+\sin\lambda}{1-\sin\lambda}\right)\frac{\mathrm{K}(k)-\mathrm{E}(k)}{k^2} \times \frac{4}{\pi}\left(\frac{t}{c}\right)^2,$$

where $k^2 = 1-[(t\cos\lambda)/c]^2$ and $\mathrm{K}(k)$ and $\mathrm{E}(k)$ are the complete elliptic integrals of the first and second kind, respectively.

Thus, for elliptic sections,

$$\frac{D'}{d_c} = \frac{\pi^2}{16}\frac{c\sin\lambda}{\log_e\left(\frac{1+\sin\lambda}{1-\sin\lambda}\right)} \times \frac{k^2}{\mathrm{K}(k)-\mathrm{E}(k)}.$$

Figure 8 gives the values of $D'/(cd_c)$ for various values of t/c. It is seen that $D'/(cd_c)$ increases as t/c is increased, unlike the case when the wing section is biconvex, when it was independent of t/c. It is also seen that $D'/(cd_c)$ decreases as λ is increased in a similar way to when the wing has a biconvex section.

*It is noted that as $t/c \to 0$ this equation gives the surprising result that $d_c/(t/c)^2 \to \infty$, so that the spanwise extent of the drag force would appear to tend to zero.

ACKNOWLEDGMENT

Acknowledgment is made to the Chief Scientist, Department of Supply, Australia, for permission to publish this paper.

REFERENCES

1. NEUMARK, S. Critical Mach Numbers for Swept-Back Wings. *Aeronautical Quarterly*, Vol. II, pp. 85-110, August 1950.

2. KÜCHEMANN, D. and WEBER, J. The Subsonic Flow past Swept Wings at Zero Lift Without and With Body. R. & M. 2908, 1956.

3. LAMB, H. *Hydrodynamics*. Sixth Edition. Cambridge University Press, 1932.

4. HURLEY, D. G. Note on the Forces that Act near the Centre and the Tips of Swept Wings. A.R.L. Note A.150, 1956.

5. ABBOTT, I. H. and VON DOENHOFF, A. E. *Theory of Wing Sections*. McGraw-Hill, London, 1949.

6. MILNE-THOMPSON, L. M. *Theoretical Hydrodynamics*. Second Edition. Macmillan, London, 1949.

7. HARDY, G. H. The Theory of Cauchy's Principal Values (Third Paper: Differentiation and Integration of Principal Values). *Proceedings of the London Mathematical Society*, Vol. XXXV, pp. 81-107, 1902.

Appendix

EVALUATION OF $\int_0^c (2u_x+u_x^2+u_z^2)\, x\, (dz/dx)\, dx$ FOR ARBITRARY PROFILES USING LINEAR THEORY

Introducing the approximations of linear theory and taking $c=1$ the integral becomes

$$\left.\begin{aligned} I &= 2\int_0^1 u_x\, x\, \frac{dz}{dx}\, dx \\ \text{where } \frac{dz}{dx} &= \sigma(x), \text{ say} \\ \text{and } u_x &= \frac{1}{\pi}\, \mathrm{P}\int_0^1 \frac{\sigma(t)}{x-t}\, dt, \end{aligned}\right\} \quad . \quad . \quad . \quad . \quad (24)$$

where P denotes that the principal value of the integral is taken.

$$\text{Thus } u_x = \frac{1}{\pi}\int_0^1 \frac{\sigma(t)-\sigma(x)}{x-t}\,dt + \frac{\sigma(x)}{\pi}\,\mathrm{P}\int_0^1 \frac{dt}{x-t}$$

$$= \frac{1}{\pi}\int_0^1 \frac{\sigma(t)-\sigma(x)}{x-t}\,dt + \frac{\sigma(x)}{\pi}\log_e\frac{x}{1-x}$$

and, from equation (24),

$$I = \frac{2}{\pi}\int_0^1\int_0^1 \frac{x\sigma(x)\,[\sigma(t)-\sigma(x)]}{x-t}\,dt\,dx + \frac{2}{\pi}\int_0^1 x\sigma^2(x)\log_e\frac{x}{1-x}\,dx$$
$$= I_1 + I_2 + I_3 \qquad \ldots\ldots \quad (25)$$

$$\left.\begin{aligned} \text{where } I_1 &= \frac{2}{\pi}\int_0^1\int_0^x \frac{x\sigma(x)\,[\sigma(t)-\sigma(x)]}{x-t}\,dt\,dx \\ I_2 &= \frac{2}{\pi}\int_0^1\int_x^1 \frac{x\sigma(x)\,[\sigma(t)-\sigma(x)]}{x-t}\,dt\,dx \\ \text{and } I_3 &= \frac{2}{\pi}\int_0^1 x\sigma^2(x)\log_e\left(\frac{x}{1-x}\right)dx \end{aligned}\right\} \ldots\ldots \quad (26)$$

If $d\sigma/dx$ exists, I_2 is proper, so that the order of integration may be changed to give

$$I_2 = \frac{2}{\pi}\int_0^1\int_0^t \frac{x\sigma(x)\,[\sigma(t)-\sigma(x)]}{x-t}\,dx\,dt,$$

and interchanging the symbols x and t gives

$$I_2 = \frac{2}{\pi}\int_0^1\int_0^x \frac{t\sigma(t)\,[\sigma(x)-\sigma(t)]}{t-x}\,dt\,dx.$$

Thus, from equation (26),

$$I_1 + I_2 = \frac{2}{\pi}\int_0^1\int_0^x \sigma(x)\,\sigma(t)\left[\frac{x}{x-t}+\frac{t}{t-x}\right]dt\,dx - \frac{2}{\pi}\int_0^1\int_0^x \frac{x\sigma^2(x)-t\sigma^2(t)}{x-t}\,dt\,dx$$

$$= \frac{2}{\pi}\int_0^1\int_0^x \sigma(x)\,\sigma(t)\,dt\,dx - \frac{1}{\pi}\int_0^1\int_0^1 \frac{x\sigma^2(x)-t\sigma^2(t)}{x-t}\,dt\,dx,$$

since the value of $[x\sigma^2(x)-t\sigma^2(t)]/(x-t)$ is unchanged by interchanging x and t.

Thus, using equation (24),

$$I_1+I_3=\frac{2}{\pi}\int_0^1 \frac{dz}{dx} z\,dx-\frac{1}{\pi}\int_0^1 \mathrm{P}\int_0^1 \frac{x\sigma^2(x)}{x-t}\,dt\,dx+\frac{1}{\pi}\int_0^1 \mathrm{P}\int_0^1 \frac{t\sigma^2(t)}{x-t}\,dt\,dx. \quad . \quad . \quad . \quad (27)$$

The first term on the right hand side is

$$\frac{1}{\pi}\Big[z^2\Big]_{x=0}^1$$

and is thus zero, since $z=0$ at $x=0$ and 1.

Using a theorem due to Hardy[7], the order of integration in the third term may be changed, provided that $d\sigma/dx$ is continuous, so that it becomes

$$\frac{1}{\pi}\int_0^1 \mathrm{P}\int_0^1 \frac{t\sigma^2(t)}{x-t}\,dx\,dt=\frac{1}{\pi}\int_0^1 t\sigma^2(t)\,\mathrm{P}\int_0^1 \frac{1}{x-t}\,dx\,dt$$

$$=\frac{1}{\pi}\int_0^1 t\sigma^2(t)\log_e\frac{1-t}{t}\,dt.$$

The second term on the right hand side of equation (27) is also equal to this expression, so that equation (27) becomes

$$I_1+I_2=\frac{2}{\pi}\int_0^1 t\sigma^2(t)\log_e\frac{1-t}{t}\,dt$$

$$=-I_3\,,\ \text{from equation (26).}$$

Thus, from equation (25), $I=0$.

On the Buckling of Certain Optimum Plate Structures with Linearly Varying Thickness

E. H. MANSFIELD, M.A., Sc.D., A.F.R.Ae.S.

(*Royal Aircraft Establishment*)

SUMMARY: This paper is concerned with the buckling under uniform longitudinal compression of a variety of structures composed of plates whose thickness tapers linearly to zero across the section. Such structures include the angle of Fig. 1, the strut of cruciform section of Fig. 2 and the simply-supported strip of Fig. 3. For given cross-sectional area and overall dimensions (*e.g.* length of arm) the sections with linearly varying thickness achieve a greater buckling load (assuming that local buckling, rather than Euler buckling, is the criterion) than sections with any other smooth variation of thickness. These particular sections are therefore optimum sections and, even if they may not be used in practice, provide a convenient yardstick for purposes of comparison. The buckling loads are considerably greater than those for the corresponding "constant thickness" sections.

NOTATION

Ox, Oy	Cartesian axes, Ox measured lengthwise, Oy measured across the width from the simply-supported edge
a	length of plate
b	width of singly tapered plate
t_0	maximum thickness of tapered plate (at $y=0$)
t	thickness of plate
E, G	Young's modulus and shear modulus
ν	Poisson's ratio
D	flexural rigidity, $Et^3/\{12(1-\nu^2)\}$
$\alpha=t_0/b$	
σ_x	uniform compressive buckling stress
w	displacement normal to plane of plate
n	integer
A_n	arbitrary constant.

Received February 1959

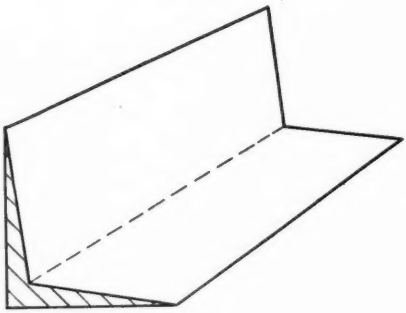

FIGURE 1.

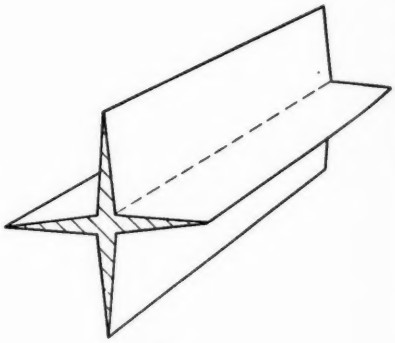

FIGURE 2.

1. Method of Solution

The basic problem is the determination of the buckling stress of the tapered plate shown in Fig. 4 subject to conditions of simple-support along the ends $x=0, a$ and along the edge $y=0$, and zero moment and shear along the edge $y=b$. Because of the variable flexural rigidity of the plate the differential equation[1] contains derivatives of D:—

$$D\nabla^4 w+2\frac{dD}{dy}\frac{\partial}{\partial y}(\nabla^2 w)+\frac{d^2D}{dy^2}\left(\nu\frac{\partial^2 w}{\partial x^2}+\frac{\partial^2 w}{\partial y^2}\right)+\sigma_x t\frac{\partial^2 w}{\partial x^2}=0. \quad . \quad (1)$$

$$\text{Now} \quad D=\frac{Et_0^3}{12(1-\nu^2)}\left(1-\frac{y}{b}\right)^3,$$

$$\text{so that} \quad (1-\nu)\frac{d^2D}{dy^2}=\frac{Et}{2(1+\nu)}\left(\frac{t_0}{b}\right)^2$$

$$=Gt\alpha^2 \quad . \quad . \quad . \quad . \quad . \quad (2)$$

and equation (1) can therefore be written in the form

$$D\nabla^4 w+2\frac{dD}{dy}\frac{\partial}{\partial y}(\nabla^2 w)+\frac{d^2D}{dy^2}\nabla^2 w+(\sigma_x-G\alpha^2)\,t\frac{\partial^2 w}{\partial x^2}=0. \quad . \quad . \quad (3)$$

A glance at equation (3) shows that if

$$\sigma_x=G\alpha^2 \quad . \quad . \quad . \quad . \quad . \quad (4)$$

the last term vanishes, and if

$$\nabla^2 w=0 \quad . \quad . \quad . \quad . \quad . \quad (5)$$

the first three terms vanish. There are an infinite number of solutions of equation (5) satisfying all the boundary conditions and the general solution can be expressed as follows in the form of an infinite series with arbitrary coefficients.

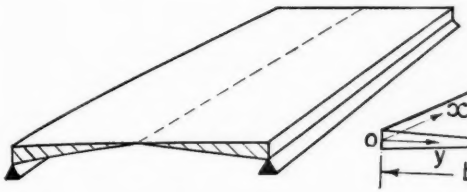

FIGURE 3.

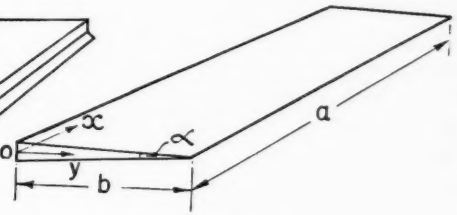

FIGURE 4.

$$w = \sum_{n=1}^{\infty} A_n \sin(n\pi x/a) \sinh(n\pi y/a). \quad . \quad . \quad . \quad (6)$$

Equations (4) and (6) represent the complete solution, which might also have been deduced from the particular approach of Ref. 2, based on energy considerations. It is to be noted that, because of the vanishing of D and dD/dy along the free edge, the conditions there are automatically satisfied by any smoothly varying deflection function.

The fact that the buckling stress is proportional to the shear modulus G, rather than to $E/(1-\nu^2)$, is at first surprising, until it is seen that in any of the buckling modes the sum of the principal curvatures is zero, so that conditions of pure twist exist everywhere. The fact that there is an infinite number of possible buckling modes occurring at the same value of the compressive stress implies that the structure is an optimum one; any small variation of thickness designed to raise the buckling stress in certain modes will lower the buckling stress in others.

If the edge of the plate is clamped, or elastically restrained against rotation, the plate with a linearly varying thickness is no longer the optimum one; it will, in fact, buckle at the same stress as for the simply-supported case—the buckles being initially confined to a vanishingly narrow strip along the free edge:—

$$w \simeq \operatorname*{Lim}_{n\to\infty} A_n \sin(n\pi x/a) \sinh(n\pi y/a). \quad . \quad . \quad . \quad (7)$$

2. Comparison with Constant Thickness Sections

For purposes of comparison with the angle of Fig. 1 and the cruciform strut of Fig. 2 it is sufficient to consider a single plate simply-supported along one edge and free along the other. The thickness of the constant thickness plate of equal weight is $\frac{1}{2}t_0$ and the buckling stress is therefore given by[3]

$$\sigma_x = \tfrac{1}{4}G\left(\frac{t_0}{b}\right)^2 \left\{1 + \frac{\pi^2}{6(1-\nu)}\left(\frac{b}{a}\right)^2\right\} \quad . \quad . \quad . \quad . \quad (8)$$

compared with $$\sigma_x = G\left(\frac{t_0}{b}\right)^2 \quad . \quad . \quad . \quad . \quad . \quad . \quad . \quad . \quad (9)$$

for the tapered plate.

It follows from equations (8) and (9) for moderate ratios of $a:b$ that the tapered plate, and hence the angle and the cruciform strut in Figs. 1 and 2, will buckle at a stress nearly four times greater than one of constant thickness. However, for very short plates ($a < 0{\cdot}9b$) the constant thickness plate is the better; this is because the influence of the supported edge is diminished and the plate tends to buckle as an "Euler plate". Similarly, for very long struts, in which Euler buckling of the complete strut is possible, the constant thickness strut may again be better.

If $a > 2b$, the simply-supported constant thickness plate, of thickness $\frac{1}{2}t_0$ and width $2b$, buckles at a stress given by

$$\sigma_x \simeq \frac{\pi^2 E}{48(1-\nu^2)}\left(\frac{t_0}{b}\right)^2. \qquad . \quad . \quad . \quad . \quad . \quad (10)$$

It follows from equations (9) and (10) that the doubly tapered plate will buckle at a stress $24(1-\nu)/\pi^2$ times that of the constant thickness plate, and it will be noted that

$$\left.\begin{aligned}\frac{24(1-\nu)}{\pi^2} &= 1{\cdot}70 \text{ if } \nu = 0{\cdot}3 \\ \text{or} &= 1{\cdot}82 \text{ if } \nu = 0{\cdot}25\end{aligned}\right\} \qquad . \quad . \quad . \quad . \quad . \quad (11)$$

These ratios may be compared with the maximum value of 1·40 obtained by Capey[4] for a stepped cross section with a thin central strip. The doubly tapered plate is, of course, ruled out on practical considerations because of the vanishing thickness at the centre, resulting in zero shear rigidity in the plane of the plate.

FIGURE 5.

However, a localised increase in thickness over this region, such as indicated in Fig. 5, could give the necessary shear rigidity and strength without seriously altering the buckling stress for the "lower" modes, the buckling stress for the "higher" modes being considerably increased.

REFERENCES

1. TIMOSHENKO, S. *Theory of Plates and Shells*. McGraw-Hill, p. 195, 1940.

2. MANSFIELD, E. H. Leading Edge Buckling due to Aerodynamic Heating. Unpublished M.O.S. Report.

3. TRAYER, G. W. and MARCH, H. W. Elastic Instability of Members having Sections Common in Aircraft Construction. N.A.C.A. Report 382, 1931.

4. CAPEY, E. C. The Buckling under Longitudinal Compression of a Simply-Supported Panel that Changes in Thickness across the Width. A.R.C. Current Paper 235, 1956.

Flow in a Viscous Trailing Vortex

B. G. NEWMAN, M.A., Ph.D., A.F.R.Ae.S.

(*Department of Engineering, University of Cambridge*)

SUMMARY: The equations of motion for an isolated laminar viscous vortex at moderate to large Reynolds numbers are linearised, by assuming that both the rotational velocity and the deficit of longitudinal velocity are small compared with that in the free stream. The rotational motion and the longitudinal motion may then be superimposed and solutions are readily obtained for each. If the vortex is generated by a body with profile drag it is predicted that the deficit of longitudinal velocity will be positive, which is in agreement with experimental observation. Further details of the solution and its relation to the flow in real vortices are discussed; and the theory is compared with some measurements in a turbulent vortex.

1. Introduction

When fluid flows past a lifting wing trailing vorticity is produced which, at some distance downstream, eventually concentrates into two trailing vortices. At large distances from the centre of each vortex the rotational or swirl velocity associated with each is very closely equal to that of a free irrotational vortex. This fact is exploited when determining the effect of vortices at large distances as, for example, in the determination of ground effect and wind-tunnel interference. Near the centre of each vortex, however, the distribution of rotational velocity progressively deviates from that of a free vortex and at the centre the velocity is zero instead of infinite. A better approximation to the trailing vortex is then provided by the Rankine combined vortex consisting of a core of fluid rotating like a solid body, surrounded by a free vortex. In this model of the flow the radius of the forced vortex core should increase as the flow proceeds downstream and the vorticity diffuses outwards. The rotational velocity at any particular radius within the core decreases until, very far downstream, the velocity is negligible and the vortex has completely decayed. However, an inviscid model of this kind does not enable the diffusion of vorticity and decay of the vortex to be predicted. Furthermore it is implicitly assumed that the longitudinal or axial velocity within the vortex is constant. This does not appear to be true in general; for example, Hilton[1] has measured a reduced longitudinal velocity near the centre of a trailing vortex.

Received June 1958.

The diffusion of vorticity and decay of a vortex are important in some practical applications. Andrews[2] and Kraft[3] have both shown that the flow disturbance several span lengths downstream of an aircraft is mainly associated with the rotational flow in the trailing vortices and thus a knowledge of their decay is of interest when assessing the behaviour of a second pursuing aircraft. Another example is afforded by the use of small, low aspect ratio fins as vortex generators to prevent boundary-layer separation from a wing or other surface. The trailing vortices re-energise the boundary layer and the downstream extent of their effectiveness depends on the extent to which the rotational velocity within the vortices is maintained.

In this paper a small perturbation analysis of a single trailing vortex is presented. The vortex is formed in a viscous incompressible fluid and is assumed to be laminar. The equations of motion and continuity are linearised by assuming that both the rotational velocity and the deficit of longitudinal velocity within the vortex are small compared with the undisturbed stream velocity. As a result of the linearisation the equations for the rotational and longitudinal motion separate, and simple solutions are obtained for each. A similar type of solution has been given by Görtler[4] for the flow in a jet with weak swirl, although it differs from the present analysis in that the variation of static pressure associated with the swirl is neglected.

Notation

r, θ, z cylindrical polar co-ordinates: Oz is along the axis of the vortex

u radial velocity component

v rotational velocity component

w' longitudinal velocity component parallel to Oz

W longitudinal velocity in the free stream at large r

$w = W - w'$, longitudinal velocity defect

p static pressure

p_∞ static pressure in the free stream

P total pressure

P_∞ total pressure in the free stream

ρ density of the fluid

ν kinematic viscosity of the fluid

η eddy viscosity when the flow is turbulent

Γ circulation round the vortex at large r

D drag of body producing the vortex

D_0 profile drag, value of D as $\Gamma \longrightarrow 0$

D_i induced drag

$r_1 = 2z\,(\nu/Wz)^{1/2}$, radius of the equivalent forced vortex

$v_1 = (\Gamma/4\pi z)(Wz/\nu)^{1/2}$, rotational velocity at the edge of the forced vortex

$R = r/r_1$, non-dimensional radius

$V = v/v_1$, non-dimensional rotational velocity

ϕ measured upwash angle within the vortex in a plane parallel to the trailing edge and the free stream velocity, $\simeq \tan^{-1}(v/W)$.

2. Analysis of a Laminar Viscous Trailing Vortex

The flow is assumed to be steady, axi-symmetric, incompressible and laminar. Choosing cylindrical polar co-ordinates r, θ and z, where Oz is the axis of symmetry, and denoting the radial velocity by u, the rotational velocity by v and the longitudinal velocity by w', the equations of motion are[5]

radial:
$$u\frac{\partial u}{\partial r} + w'\frac{\partial u}{\partial z} - \frac{v^2}{r} = -\frac{1}{\rho}\frac{\partial p}{\partial r} + \nu\left[\nabla^2 u - \frac{u}{r^2}\right], \quad . \quad . \quad . \quad (1)$$

rotational:
$$u\frac{\partial v}{\partial r} + w'\frac{\partial v}{\partial z} + \frac{uv}{r} = \nu\left[\nabla^2 v - \frac{v}{r^2}\right], \quad . \quad . \quad . \quad . \quad . \quad (2)$$

axial:
$$u\frac{\partial w'}{\partial r} + w'\frac{\partial w'}{dz} = -\frac{1}{\rho}\frac{\partial p}{\partial z} + \nu\nabla^2 w', \quad . \quad . \quad . \quad . \quad (3)$$

where $$\nabla^2 \equiv \frac{\partial^2}{\partial r^2} + \frac{1}{r}\frac{\partial}{\partial r} + \frac{\partial^2}{\partial z^2}$$

and the continuity equation is
$$\frac{1}{r}\frac{\partial}{\partial r}(ru) + \frac{\partial w'}{\partial z} = 0. \quad . \quad . \quad . \quad . \quad (4)$$

Putting the axial velocity $w' = W - w$, where W is the axial velocity in the undisturbed fluid at large r, it is assumed that

v and w are small compared with W, *i.e.* $O(\varepsilon)$ if W is $O(1)$,

u is very small compared with W, *i.e.* $O(\varepsilon^2)$.

Thus, if z is $O(1)$, the continuity equation (4) indicates that r is $O(\varepsilon)$.

The radial equation (1) therefore becomes

$$\underset{(\varepsilon^3)}{u\frac{\partial u}{\partial r}} + \underset{(\varepsilon^2)}{W\frac{\partial u}{\partial z}} - \underset{(\varepsilon^3)}{w\frac{\partial u}{\partial z}} - \underset{(\varepsilon)}{\frac{v^2}{r}} = -\frac{1}{\rho}\frac{\partial p}{\partial r} + \nu\left[\underset{(\nu)}{\frac{\partial^2 u}{\partial r^2}} + \underset{(\nu)}{\frac{1}{r}\frac{\partial u}{\partial r}} + \underset{(\nu\varepsilon^2)}{\frac{\partial^2 u}{\partial z^2}} - \underset{(\nu)}{\frac{u}{r^2}}\right]$$

where the order of magnitude of the various terms is indicated.

If the Reynolds number of the main flow Wz/ν is large and $O(1/\varepsilon^2)$, *i.e.* ν is $O(\varepsilon^2)$, then the radial equation simplifies to equation (5) which follows:—

$$\frac{v^2}{r} = \frac{1}{\rho}\frac{\partial p}{\partial r}, \qquad (5)$$

also indicating that $(1/\rho)\,\partial p/\partial r$ is $O(\varepsilon)$.

The rotational equation (2) becomes

$$\underset{(\varepsilon^2)}{u}\frac{\partial v}{\partial r} + \underset{(\varepsilon)}{W}\frac{\partial v}{\partial z} - \underset{(\varepsilon^2)}{w}\frac{\partial v}{\partial z} + \underset{(\varepsilon^2)}{\frac{uv}{r}} = \nu\left[\underset{(\varepsilon)}{\frac{\partial^2 v}{\partial r^2}} + \underset{(\varepsilon)}{\frac{1}{r}\frac{\partial v}{\partial r}} + \underset{(\varepsilon^3)}{\frac{\partial^2 v}{\partial z^2}} - \underset{(\varepsilon)}{\frac{v}{r^2}}\right],$$

and thus simplifies to

$$W\frac{\partial v}{\partial z} = \nu\left[\frac{\partial^2 v}{\partial r^2} + \frac{1}{r}\frac{\partial v}{\partial r} - \frac{v}{r^2}\right] \qquad (6)$$

The axial equation (3) becomes

$$\underset{(\varepsilon^2)}{-u}\frac{\partial w}{\partial r} - \underset{(\varepsilon)}{W}\frac{\partial w}{\partial z} + \underset{(\varepsilon^2)}{w}\frac{\partial w}{\partial z} = \underset{(\varepsilon^2)}{-\frac{1}{\rho}\frac{\partial p}{\partial z}} - \nu\left[\underset{(\varepsilon)}{\frac{\partial^2 w}{\partial r^2}} + \underset{(\varepsilon)}{\frac{1}{r}\frac{\partial w}{\partial r}} + \underset{(\varepsilon^3)}{\frac{\partial^2 w}{\partial z^2}}\right],$$

and hence this equation simplifies to

$$W\frac{\partial w}{\partial z} = \nu\left[\frac{\partial^2 w}{\partial r^2} + \frac{1}{r}\frac{\partial w}{\partial r}\right] \qquad (7)$$

It will be noticed that equations (6) and (7) are now linear and the variables v and w have been separated.

The continuity equation (4) becomes

$$\frac{1}{r}\frac{\partial}{\partial r}(ru) - \frac{\partial w}{\partial z} = 0. \qquad (8)$$

By the nature of the approximations we are examining the vortex some distance downstream of its origin. Hence it is sufficient to assume that the vortex is suddenly generated at $z=0$ as a free vortex of circulation Γ. Far downstream the vortex finally decays until all the perturbation velocities u, v and w are once again zero. The boundary conditions to be satisfied by equations (5) to (8) are thus

$z = 0$, $v = \Gamma/(2\pi r)$ and $w = 0$ except at the singular point $r = 0$,

$z > 0$, v and $w \longrightarrow 0$ when r is large (though still small compared with z),

$z \longrightarrow \infty$, v and $w \longrightarrow 0$ for all r.

The solution of equation (6) which satisfies these boundary conditions is identical with that given by Lamb[6] for the development with time of a two-dimensional viscous vortex if the time t is replaced by z/W, and it has previously been given in this form by Squire[7]:—

$$v = \frac{\Gamma}{2\pi r}\left[1 - e^{-Wr^2/(4\nu z)}\right] \quad . \quad . \quad . \quad . \quad . \quad . \quad (9)$$

The solution of (7) is $w = \frac{A}{z} e^{-Wr^2/(4\nu z)}$, ... (10)

where A is a constant, as yet undetermined.

The distribution of radial velocity u is given by equation (8):—

$$u = -\frac{Ar}{2z^2} e^{-Wr^2/(4\nu z)} \quad . \quad . \quad . \quad . \quad . \quad . \quad (11)$$

The constant A may be determined by considerations of momentum. The rotational and the axial-radial flows are independent of one another and thus equations (10) and (11) represent the distributions of w and u for all values of the vortex strength Γ. Thus if D is the drag of the body which is producing the vortex it is apparent that the limit of D as $\Gamma \longrightarrow 0$*, D_0 say, is such that

$$D_0 = \int_0^\infty \rho\,(W - w)\, w 2\pi r\, dr = \int_0^\infty \rho W w\, 2\pi r dr,$$

since w is small compared with W.

Hence $A = \frac{D_0}{4\pi\rho\nu}$.

The static pressure distribution is dependent only on the rotational velocity v and is given by equations (5) and (9).

For large r, $v = \frac{\Gamma}{2\pi r}$, a "free" vortex

and for small r, $v = \frac{\Gamma W r}{8\pi\nu z}$, a "forced" vortex.

These "free" and "forced" vortices meet at

$$r_1 = 2z\left(\frac{\nu}{Wz}\right)^{1/2} \text{ and } v_1 = \frac{\Gamma}{4\pi z}\left(\frac{Wz}{\nu}\right)^{1/2}.$$

*In proceeding to this limit it is assumed that the wake flow remains axi-symmetric.

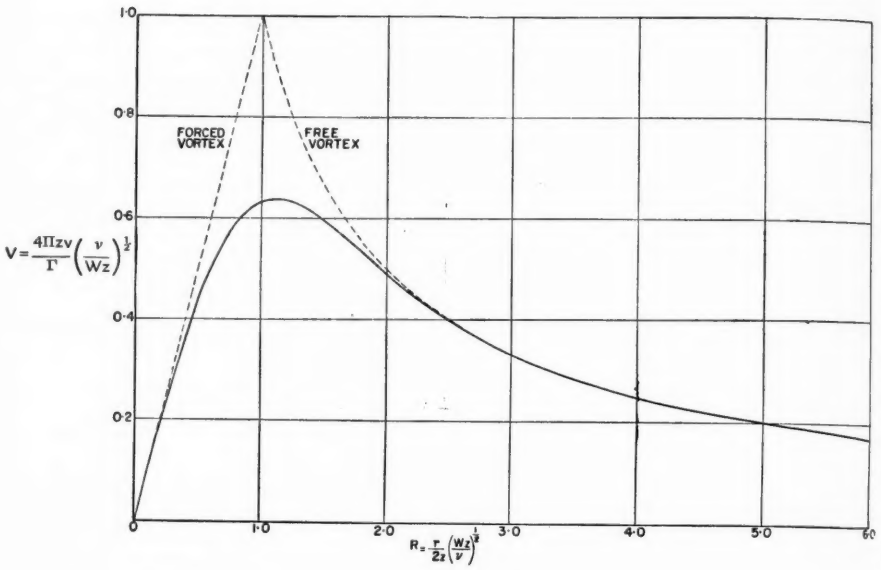

FIGURE 1.

r_1 may be thought of as the radius of the vortex core of an equivalent Rankine vortex (*see* Fig. 1).

It is convenient to rewrite equation (9) with v and r made non-dimensional in terms of v_1 and r_1.

$$\text{Thus } V=\frac{1}{R}\left[1-e^{-R^2}\right] \quad \text{where } V=v/v_1 \text{ and } R=r/r_1.$$

The maximum value of V is 0·639 and occurs at $R=1{\cdot}12$.

The distribution of V is shown in Fig. 1.

The variation of static pressure is given by equation (5):—

$$\frac{1}{\rho v_1^2}\frac{\partial p}{\partial R}=\frac{1}{R^3}[1-2e^{-R^2}+e^{-2R^2}].$$

Hence, integrating from R to ∞,

$$\frac{p_\infty-p}{\frac{1}{2}\rho v_1^2}=\frac{1}{R^2}-2\left[\frac{e^{-R^2}}{R^2}+\mathrm{Ei}(-R^2)\right]+\left[\frac{e^{-2R^2}}{R^2}+2\mathrm{Ei}(-2R^2)\right],$$

where $\mathrm{Ei}(-x)=-\int_x^\infty \frac{e^{-t}}{t}\,dt$, one of the exponential integrals, and p_∞ is the static

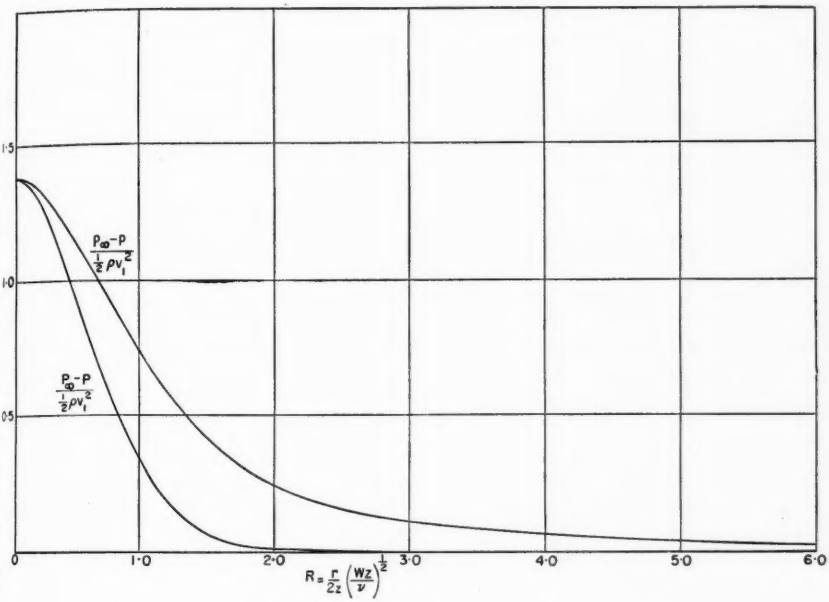

FIGURE 2.

pressure in the free stream. The limiting value of $(p_\infty - p)/(\frac{1}{2}\rho v_1^2)$ when $R \longrightarrow 0$ is $2 \log_e 2$, and the variation of $(p_\infty - p)/(\frac{1}{2}\rho v_1^2)$ with R is shown in Fig. 2.

The distribution of total pressure P through the vortex is dependent on both the rotational and the longitudinal motion.

$$\frac{P_\infty - P}{\rho} = \frac{p_\infty - p}{\rho} + \frac{1}{2}\,[2Ww - w^2 - v^2 - u^2],$$
$$(\varepsilon^2) \qquad (\varepsilon) \quad (\varepsilon^2)\ (\varepsilon^2)\ (\varepsilon^4)$$

where P_∞ is the total pressure in the free stream.

Thus, if w and v are of the same order of smallness, the deficit of total pressure in the vortex is associated mainly with the longitudinal motion and

$$\frac{P_\infty - P}{\frac{1}{2}\rho W^2} = \frac{D_0}{2\pi\rho\nu Wz}\, e^{-Wr^2/(4\nu z)}.$$

However, it is not essential to the analysis that v and w are of the *same* order of smallness, but merely that both are small compared with W. Thus the second-order contribution to the total pressure variation from the rotational motion may be significant when the longitudinal velocity deficit is very small.

This is given by $$\frac{P_\infty - P}{\frac{1}{2}\rho v_1^2} = \frac{p_\infty - p}{\frac{1}{2}\rho v_1^2} - \frac{v^2}{v_1^2}$$
$$= 2\,[\mathrm{Ei}\,(-2R^2) - \mathrm{Ei}\,(-R^2)],$$

which is also shown in Fig. 2.

3. Discussion

The present solution is based on the assumption that the rotational velocity and the defect of longitudinal velocity within the vortex are both small compared with the free stream velocity. It is therefore clear from equations (9) and (10) that the solution is invalid in the immediate vicinity of the origin O where the vortex is generated, but that it becomes increasingly accurate as the flow proceeds downstream.

Certain details of the solution are worth noting. The radius of the equivalent forced vortex core $r_1 = 2z\,(Wz/\nu)^{-1/2}$ and is proportional to $z^{1/2}$. As expected from the nature of the approximations, the growth of the vortex core is similar to that of a laminar boundary layer in zero pressure gradient. The maximum rotational velocity $v_{max} = 0{\cdot}639\,(\Gamma/4\pi z)\,(Wz/\nu)^{1/2}$ occurs at a radius $1{\cdot}12\,r_1$ and at this radius the static pressure rise from the centre of the vortex is just over half the total rise attained at large radii.*

The maximum deficit of total pressure occurs at the centre of the vortex and is given by

$$\left(\frac{P_\infty - P}{\frac{1}{2}\rho W^2}\right)_{max} = \frac{D_0}{2\pi\rho\nu W z} + (2\log_e 2)\frac{v_1^2}{W^2} \quad . \quad . \quad . \quad (12)$$

If the vortex is assumed to be one of those generated by a wing with an elliptic spanwise distribution of circulation, then the vortex drag $D_i = \frac{1}{8}\pi\rho\Gamma^2$ and equation (12) may be written

$$\left(\frac{P_\infty - P}{\frac{1}{2}\rho W^2}\right)_{max} = \frac{1}{2\pi\rho\nu W z}\left\{D_0 + \left(\frac{2\log_e 2}{\pi^2}\right)D_i\right\},$$

the two terms being respectively the contributions associated with the longitudinal and the rotational motion. Since D_i is usually of the same order as, or less than, D_0, the contribution from the longitudinal motion is usually greater than that from the rotational motion if, as seems probable, most of the wake leaving the wing is gathered into the two trailing vortices, so that $2D_0$ represents a large proportion of the total profile drag of the wing.† This tendency is noted in the measurements of Fage and Simmons[8] in the wake behind a wing.

*Compared with the Rankine vortex for which exactly half the pressure rise occurs at the edge of the forced vortex core.

†Note that the total drag of the wing is expressed as $2D_0 + D_i$.

Since the effective profile drag is usually positive, there will usually be a deficit of longitudinal velocity in the trailing vortices generated by a wing. Such a deficit has been measured by both Hilton[1] and Templin[9] and it has also recently been found by Mowforth within the vortex generated by a half wing mounted on the wall of a wind tunnel (full details of these measurements are given in the Appendix). This conclusion will presumably apply generally to vortices generated by a closed body. However it is easy to imagine a situation in which the deficit might be negative, for example behind a jet-flapped wing.

When an attempt is made to relate the present solution in greater detail with the flow in a real trailing vortex, two questions arise. Can an isolated trailing vortex of infinite extent exist and will the flow within it be effectively laminar?

The deficit of longitudinal momentum within the vortex has been equated to the profile drag of the vortex-producing body on the assumption that all the wake is gathered into the vortex. The remaining induced drag D_i must clearly balance the net pressure force on a control volume surrounding the body.

$$\text{Thus} \quad D_i = \int_0^\infty (p_\infty - p)\, 2\pi r\, dr.$$

At large r, $p_\infty - p \propto \frac{1}{r^2}$, and hence $D_i \longrightarrow \infty$.

In other words, the drag of a body producing an isolated trailing vortex of infinite extent would be infinite and therefore such a vortex cannot strictly exist. A finite wing, of course, produces two trailing vortices, and the rotational velocities associated with each cancel at large radii so that D_i is finite. A single trailing vortex of *finite* extent is readily produced in a duct[10], in which case the flow field does not extend to infinity and the drag is once again finite. As usual the effect of the duct boundaries may be determined by the introduction of a suitable series of image vortices. Within the limits of the present small perturbation analysis, the equation for the rotational velocity, and hence the trailing vorticity, is linear and is thus unaltered by the superposition of an irrotational flow field. Hence the velocities associated with the various real and imaginary vortices may be superimposed vectorially for as long as the effectively rotational parts of the vortices ($r < 2{\cdot}5r_1$) do not overlap.* Hence, with this restriction, the present solution may be applied directly by superposition for the trailing vortices produced by a wing or for a single trailing vortex surrounded by boundaries.

It is more difficult to reach a satisfactory conclusion concerning the second question. The flow which is gathered into the trailing vortex from the wake will in general be turbulent and not laminar. However, the circulation increases with radius and thus there is a tendency for the turbulent flow to be attenuated and

*It is interesting to note that this conclusion is implicit in Prandtl's determination of the radius of the forced vortex core within the two Rankine vortices trailing behind a wing.[11]

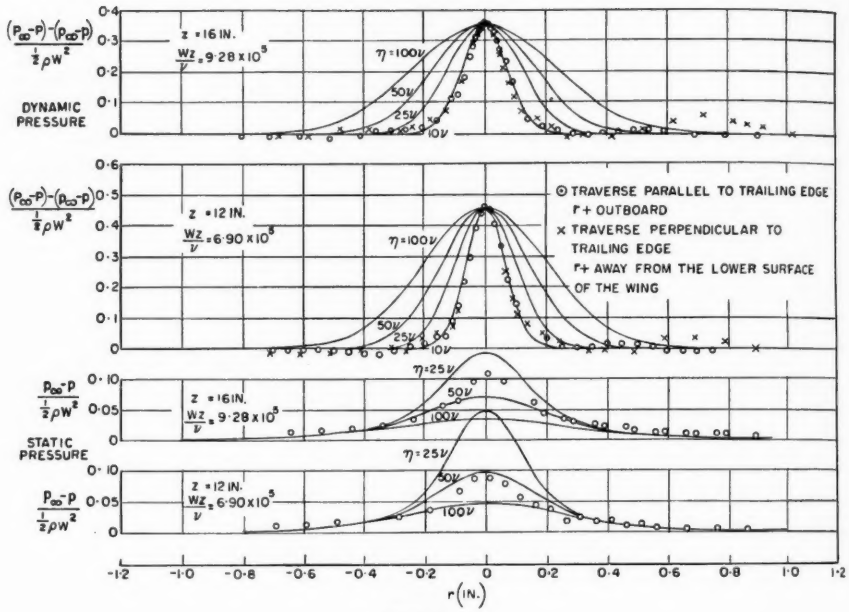

FIGURE 3.

possibly completely damped out, particularly near the core of the vortex. The high degree of stability for a rotational flow in which the circulation increases with radius was first pointed out by Rayleigh and was noted by Taylor[12] for the flow between rotating cylinders. It was also found that when the speed of rotation was sufficient for the flow to become unstable and turbulent the associated turbulent stress was nevertheless small. It is therefore expected that the eddy viscosity associated with a turbulent vortex will be small compared with that usually associated with free turbulent flow.

Following Görtler[4] and Squire[7], it is attractive to apply the present laminar solution to a turbulent vortex by simply replacing the kinematic viscosity by an eddy viscosity which is constant at each downstream station*. The present measurements, which were made some three semi-spans downstream of a rectangular half-wing, are therefore compared with the theory in this way. The results are shown in Figs. 3 and 4, where the measured values of downwash angle, Pitot and static pressures are compared directly with the theory for various values of the eddy viscosity. Full details of the measurements and the method of reducing them will be found in the Appendix. The results indicate that an eddy viscosity of approximately 10ν is appropriate for the deficit of dynamic pressure associated with the longitudinal motion near the centre of the vortex, with somewhat higher values farther out, although it should be noted that the vortex is no longer axi-symmetric in this region.

*This is considered to be slightly more convenient than the usual procedure of *adding* an eddy viscosity to the kinematic viscosity.

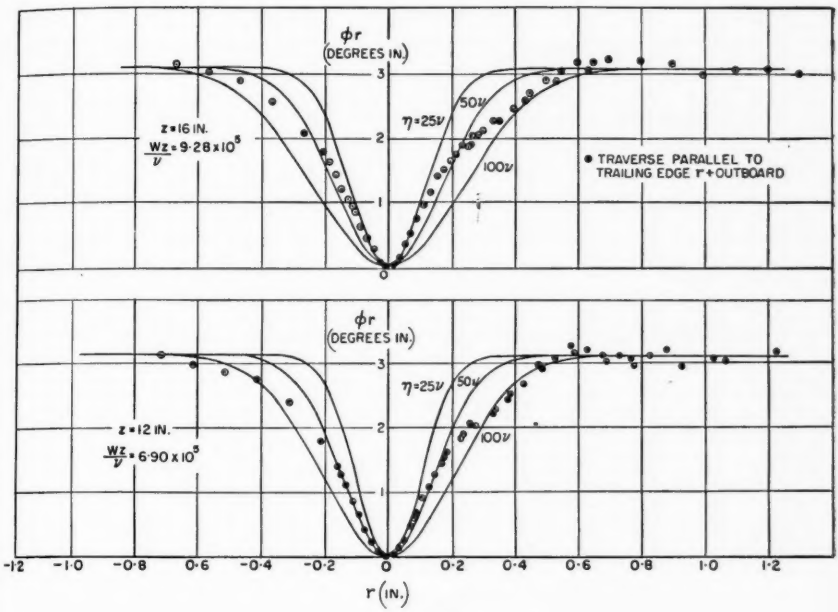

FIGURE 4.

For the rotational motion the independent measurements of static pressure and downwash angle are in agreement in giving the following values for the eddy viscosity near the centre of the vortex:—

12 in. station, $\eta = 50\nu$

16 in. station, $\eta = 30\nu$

and farther out $\eta = 100\nu$ approximately in both cases.

It should be noted that these results are qualitatively in agreement with Rayleigh's ideas in that the eddy viscosity is least in those regions where $|\, d\Gamma/dr \,|$ is greatest. It is clear therefore that the flow cannot be strictly described in terms of a constant eddy viscosity at each downstream station. However, for the central part of the vortex η is approximately constant and for some engineering purposes the deviation from this curve at larger radii may be unimportant. Perhaps it should be noted that the deviation is comparable with that found for similar analyses of turbulent jets. The idea that a constant eddy viscosity gives a useful engineering approximation to the real fluid flow will therefore be pursued.

The reduction of η in the downstream direction for the rotational motion is probably associated with the fact that the vortex was not fully rolled up. Templin[9] has noted that when this is so the apparent viscosity will be large. The vorticity at any radius is greater than that in the fully rolled-up state: thus the vorticity appears to have diffused to larger radii and this leads to a fictitiously high value of the

eddy viscosity. The fall in computed C_{D_0} with downstream distance (*see* the Appendix) and the lack of complete axial symmetry support the hypothesis that the vortex was not fully rolled up.

From dimensional considerations it would be expected that η/ν would be a function of Γ/ν and Wz/ν, probably becoming independent of Wz/ν when it is large. Mowforth's values for η/ν, and also those of Templin and those of Titchener and Taylor-Russell*, are presented in Fig. 5, where the values of Wz/ν are shown in brackets.

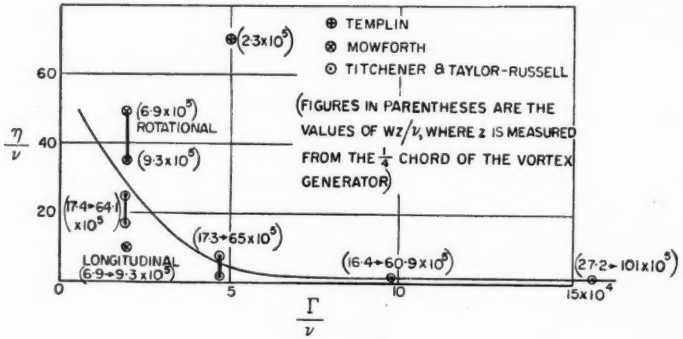

FIGURE 5.

These few results seem to be consistent in indicating that η/ν falls to a constant value with increasing Wz/ν and, for large values of Wz/ν, tends to unity as Γ/ν exceeds about 8×10^4. However this curve should only be accepted tentatively. η/ν would hardly be expected to remain unity for very high values of Γ/ν. For instance, Timme[13] has noted that the flow in the cross-stream vortices forming the Kármán vortex street behind a circular cylinder is effectively laminar if Γ/ν is *less* than $2{\cdot}5 \times 10^3$ and that above this Reynolds number the vortices become turbulent, with an apparent eddy viscosity roughly ten times the kinematic viscosity. Furthermore free turbulent flows usually become independent of viscosity, which should give η/Γ constant at large Wz/ν (Ref. 7). Clearly more measurements are needed before Fig. 5 can be accepted with any confidence.

4. Conclusions

A small perturbation analysis for a laminar viscous vortex has been given. This indicates that there is usually a deficit of longitudinal momentum within the vortex which is directly associated with the profile drag of the vortex generator, while the cross-stream variation of static pressure associated with the rotational motion directly balances the induced drag. The solution has been compared with measured turbulent vortices by replacing the kinematic viscosity by a constant eddy viscosity. The agreement is only fair, but it is noted that the theory may be useful for some engineering purposes.

*Templin's vortex was measured very near the trailing edge of a rectangular wing of aspect ratio 1/4; that of Titchener and Taylor-Russell was generated in the centre of a circular pipe.

Appendix

Details of E. Mowforth's Measurements in a Turbulent Trailing Vortex

The vortex was produced by an untwisted rectangular wing, of length (equivalent semi-span) 4·20 in. and chord 1·56 in., which was mounted as a half-model in the middle of the 20 in. wall of the 7½ in.×20 in. low speed wind tunnel at Cambridge University. The wing, which was uncambered, was set at 6° incidence and had an aerofoil section of 18½ per cent thickness/chord ratio with maximum thickness at 25 per cent chord. The wind speed was approximately 100 ft./sec. and was adjusted throughout the experiments to maintain a constant Reynolds number per foot at the wing of $W/\nu = 6{\cdot}60 \times 10^5$. The value of W/ν increased slightly down the tunnel, because of the growth of the boundary layer on the tunnel walls; the values of Wz/ν are noted on Figs. 3 and 4. A trailing vortex was thus formed in the centre of the tunnel and was measured at two stations, $z=12$ in. and $z=16$ in., downstream of the quarter-chord point. The following measurements were made:—

(*i*) Total pressure P, by means of a 0·028 in. diameter Pitot tube with lips sharpened internally. This tube measured the true total pressure for angles of yaw up to 12° and had an error of only one per cent of the dynamic pressure at 20° yaw (note that the measured yaw did not exceed 11°). The tube was traversed across the vortex, both parallel and perpendicular to the trailing edge.

(*ii*) Angle of upwash ϕ, with a null-reading Conrad yawmeter made from two 0·028 in. diameter tubes. The yawmeter was traversed through the centre of the vortex and parallel to the trailing edge.

(*iii*) Static pressure p, with a 0·028 in. diameter static tube aligned with the local flow direction as indicated by the yawmeter. This was also traversed parallel to the trailing edge.

The centre of the vortex was determined as the point of minimum total pressure from a preliminary survey with the Pitot tube. The measurements of downwash and static pressure have been corrected for small interference of the traversing gear. The downwash has also been corrected for the interference of the nearest tunnel walls (*i.e.* those 7½ in. apart). This correction was small and did not exceed 0·1°, which was the accuracy of measurement. The associated correction to static pressure was negligible.

As the vortex is not strictly axi-symmetric, the measurements are compared directly with the theory rather than in terms of a mean rotational velocity and a mean longitudinal velocity defect. The theoretical curves are presented for various values of the eddy viscosity η. For the downwash and static pressure measurements the theory has been matched with the measured value of ϕr at large r. The values at both stations are in agreement in giving $\Gamma/\nu = 1{\cdot}97 \times 10^4$. Using lifting-line theory for a rectangular wing at 6° incidence, this gives a two-dimensional lift-curve slope of approximately 5·2, which is a plausible value, bearing in mind the low Reynolds number of the experiment and the fact that about ½ in. of the wing was immersed in tunnel-wall boundary layer at the wing root. The mean curve of measured static pressure has been subtracted from the Pitot pressure to give the results shown in the top curves of Fig. 3. The theory has been matched to the value of $[(P_\infty - P) - (p_\infty - p)]/(\frac{1}{2}\rho W^2)$ at the centre of the vortex. Assuming that the eddy viscosity $\eta = 10\nu$, the measurements give

$$C_{D_0} = 0{\cdot}00183 \text{ at } 12 \text{ in.}, \quad C_{D_0} = 0{\cdot}00190 \text{ at } 16 \text{ in.}$$

These values are very low but it should be noted that much of the deficit of longitudinal momentum is found in the outer part of the vortex, when the eddy viscosity is apparently greater than 10ν and where, in any case, the flow is not strictly axi-symmetric. It also is interesting to note the slight increase of C_{D_0} with distance downstream. Discussion of these measurements is given in the main body of the paper.

References

1. Hilton, W. F. Longitudinal Flow in a Trailing Vortex. R. & M. 1858, 1938.
2. Andrews, D. R. A Flight Investigation of the Wake behind a Meteor Aircraft, with Some Theoretical Analysis. A.R.C. Current Paper 282, 1954.
3. Kraft, C. C. Flight Measurements of the Velocity Distribution and Persistence of the Trailing Vortices of an Airplane. N.A.C.A. T.N. 3377, 1955.
4. Görtler, H. Decay of Swirl in an Axially Symmetrical Jet Far from the Orifice. *Revista Matemática Hispano Americana.* 4ª Serie-Tomo XIV—Núms. 4 y 5, 1954.
5. Goldstein, S. *Modern Developments in Fluid Dynamics.* Oxford University Press, Vol. I, p. 104, 1938.
6. Lamb, H. *Hydrodynamics.* Cambridge University Press, 6th Edition, p. 591, 1932.
7. Squire, H. B. The Growth of a Vortex in Turbulent Flow. A.R.C. 16,666, 1954.
8. Fage, A. and Simmons, L. F. G. An Investigation of the Air-Flow Pattern in the Wake of an Aerofoil of Finite Span. *Phil. Trans. Roy. Soc.* A.225, p. 303, 1925.
9. Templin, R. J. Flow Characteristics in a Plane behind the Trailing Edge of a Low Aspect Ratio Wing as Measured by a Special Pressure Probe. N.A.E., Canada, LM AE-58, 1954.
10. Titchener, I. M. and Taylor-Russell, A. J. Experiments on the Growth of Vortices in Turbulent Flow. A.R.C. Current Paper 316, March 1956.
11. Durand, W. F. *Aerodynamic Theory.* Springer, Berlin, Vol. II, p. 328, 1934.
12. Taylor, G. I. Fluid Friction between Rotating Cylinders. *Proc. Roy Soc.* A.157, p. 546, 1936.
13. Timme, A. Über die Geschwindigkeitsverteilung in Wirbeln. *Ingenieur Archiv.*, Vol. 25, p. 205, 1957.

A Contribution to the Theory of Flow Stability in Multi-Stage Axial Compressors

A. D. S. CARTER, B.Sc., A.M.I.Mech.E., A.F.R.Ae.S.

(Royal Military College of Science, Shrivenham)

SUMMARY: Previous theories on the surging of axial compressors have been based on a quasi-static theory, whereas a finite rate of growth of the circulation around each blade must occur in practice. An examination of this factor is made in the paper, studying the stability with respect to small changes in speed instead of mass flow as in the normal approach. Effects of capacity are neglected. It is concluded that an instability occurs in the last stage of the compressor, even when that stage is itself unstalled, which could give rise to surge. It has been found necessary to introduce one empirical factor into the analysis but, when this is given a value compatible with other experimental and theoretical evidence, reasonably good agreement with experimental results is obtained.

1. Introduction

Although the surging of multi-stage axial compressors is a feature of paramount importance in gas turbine design and operation, the problem has received comparatively little experimental or theoretical attention. Experimental investigations are considerably hampered by safety considerations and usually confined to the simple determination of the surge line. Theoretical work is probably limited by the absence of basic test data on which to formulate any hypothesis, while the conflict of information available on surge behaviour may be a contributory factor.

The basic mechanism of surging has been expounded by Kearton[1] and Den Hartog[2]. A more formal mathematical treatment of this basic concept has been given in Reference 3. It is well known, however, that the treatment does not accord with experience, although the resulting conclusion that surge will occur at peak pressure ratio is often used as a practical guide. A much more advanced study was made by Pearson and Bowmer[4]. However, for the average compressor this gives a surge line which does not depart to any significant extent from that based on peak pressure ratio.

A fundamental criticism of the previous theoretical work is that a unique stage or compressor performance characteristic is assumed. Stability is usually

Received October 1958.

studied by the method of small displacements in the operating parameters. Any lag in change of performance which would accompany such a small change in operating conditions should really be included, but has always so far been neglected (Pearson and Bowmer quote lag as one of the major factors which could modify the results obtained by their theory). Furthermore, although the stability of operation of a compressor with respect to mass flow changes is studied, stability with respect to speed changes appears to be neglected. These aspects of the problem are taken up in this paper.

NOTATION

A	annulus area
F	constant in equation for temperature rise coefficient
k	constant
P	pressure
p	ratio of circulation during transient to circulation with constant axial velocity
R	gas constant
s	blade pitch
T	temperature
U	blade speed
V	fluid velocity
W	mass flow
α	fluid angle measured from axial direction
ΔP	pressure rise
ΔT	temperature rise
Γ	circulation
η	stage efficiency
Ω	work done factor

Suffixes

0	at exit from previous blade row
1, 2	at entry to, and exit from, blade row
I, II	at entry to, and exit from, compressor
a	axial component
t	constant throttle conditions
s	stage value
w	whirl component
τ	value during transient speed increase

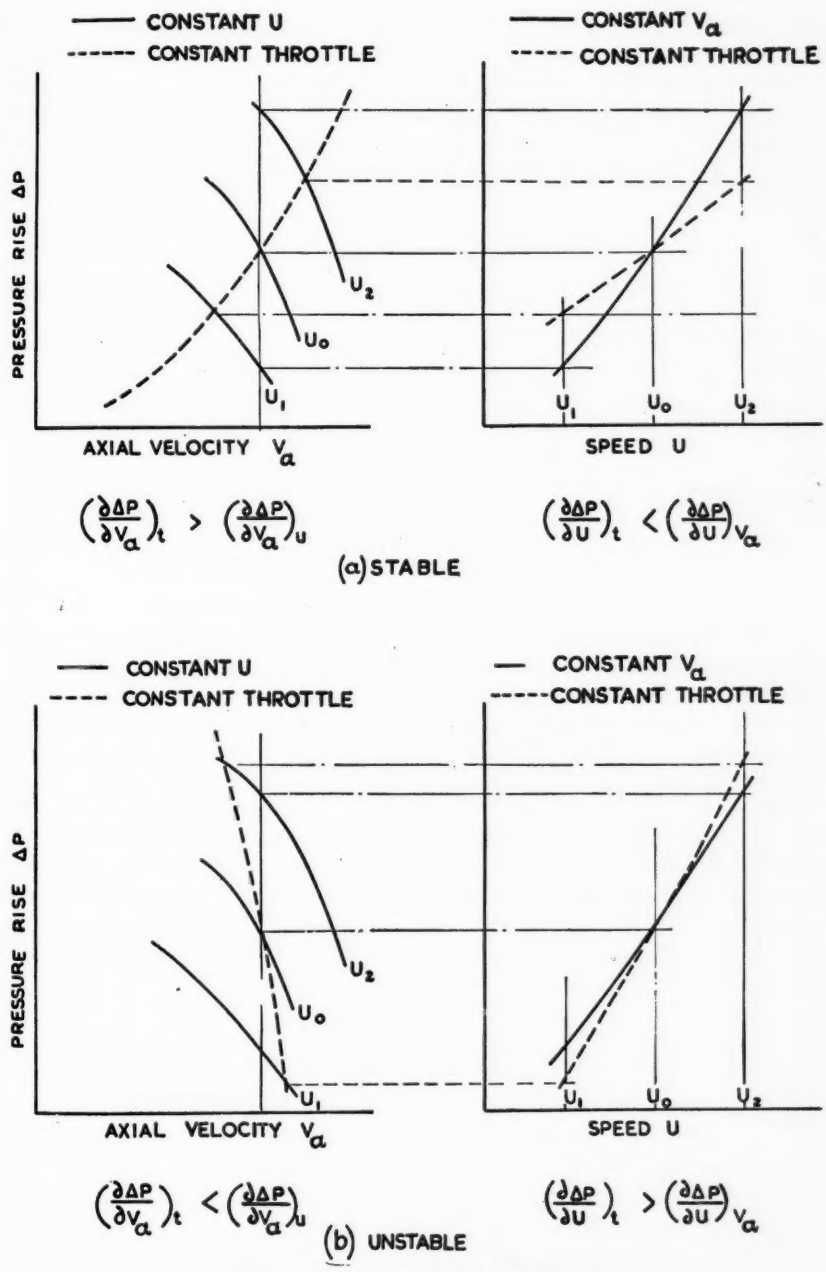

FIGURE 1. Flow conditions in a simple single-stage system.

2. General Theory

2.1. Stability of a Stage

Consider in the first instance the stability of a stage which forms part of a multi-stage compressor. The conventional approach involves the arbitrary displacement of one of the operating parameters, say mass flow. If the system is to be stable, then it can easily be shown (*see*, for example, any of the references previously quoted) that

$$\left(\frac{\partial \Delta P}{\partial V_a}\right)_t > \left(\frac{\partial \Delta P}{\partial V_a}\right)_U, \quad . \quad . \quad . \quad . \quad . \quad (1)$$

where ΔP is the pressure rise across the stage, V_a is the fluid axial velocity, suffix U denotes constant blade speed (or r.p.m.) and suffix t denotes constant throttle setting.

Figure 1(*a*) shows some typical compressor stage characteristics and also a typical constant throttle line. It is seen that the flow is stable according to the criterion (1). It is also seen from Fig. 1(*a*) that this can be written in the less familiar form

$$\left(\frac{\partial \Delta P}{\partial U}\right)_t < \left(\frac{\partial \Delta P}{\partial U}\right)_{V_a} \quad \text{for stability.} \quad . \quad . \quad (2)$$

This condition can also be shown to be necessary by the physical nature of the problem. Suppose the speed increased from U_0 to U_2, as defined in Fig. 1, then the compressor would be giving more pressure rise than is required by the throttle. To achieve this pressure rise the compressor speed would drop, by virtue of the excess load on the blades, thus making for stability. If the condition (2) were not satisfied the pressure rise at speed U_2 would be less than that required by the throttle and so the speed would have to rise, making for instability, as shown in Fig. 1(*b*) for example. This condition locates a possible point of instability at the peak pressure point as usually assumed for practical purposes. It is shown in Appendix I that (1) and (2) are only equivalent if the stage is unstalled. In that case the efficiency and the fluid outlet angle can be taken as independent of the fluid axial velocity. It can then be shown (as in Appendix I) that the conditions (1) and (2) for stability can be written

$$\left(\frac{\partial \alpha_1}{\partial V_a}\right)_t > \left(\frac{\partial \alpha_1}{\partial V_a}\right)_U \quad . \quad . \quad . \quad . \quad . \quad . \quad (3)$$

$$\left(\frac{\partial \alpha_1}{\partial U}\right)_t < \left(\frac{\partial \alpha_1}{\partial U}\right)_{V_a} \quad . \quad . \quad . \quad . \quad . \quad . \quad (4)$$

Condition (3) can also be derived directly by assuming that a small change of mass flow takes place while the speed remains constant, and condition (4) can be derived by assuming that a small change in speed takes place while the mass flow remains constant (as given in detail in Appendix I). A unique stage performance in terms

of mass flow and speed has to be assumed in both cases. Now it does seem reasonable that any small adventitious mass flow changes will occur in such a manner as to satisfy the internal aerodynamics of the stage. However, speed changes can be quite arbitrary and illustrate a fallacy in the simple stability argument. Suppose the speed increases by a quantity δU from U to $(U+\delta U)$.

At speed U the circulation will be given by

$$\Gamma = s(V_{w1} - V_{w2}) \quad . \quad . \quad . \quad . \quad . \quad . \quad (5)$$

where Γ is the circulation around the blade, and V_{w1} and V_{w2} are respectively the whirl velocity at the inlet to, and the exit from, the blade row.

It can then be shown (as in Appendix I) that

$$\left(\frac{\partial \Gamma}{\partial U}\right)_{V_a} = s. \quad . \quad . \quad . \quad . \quad . \quad . \quad . \quad (6)$$

The increase of speed (δU), supposedly taking place while the axial velocity remains constant (due to inertia) in the stability argument, must therefore be accompanied by an increase of circulation round the blades given by

$$\delta\Gamma = s\delta U. \quad . \quad . \quad . \quad . \quad . \quad . \quad . \quad (7)$$

An increase of circulation cannot occur any more than an increase in axial velocity. This is more clearly demonstrable if the speed increase δU is supposed to take place suddenly or instantaneously, a postulate usually made in the orthodox stability argument. Likewise, both axial velocity and circulation cannot remain constant. This difficulty can only be resolved by supposing that the sudden or instantaneous speed increase takes place in finite time, and that the axial velocity and circulation both change in a mutually compatible manner in that time. To take the most general case it can be assumed that, following a rapid speed increase, the circulation changes by p times the change which would be obtained if the axial velocity could have remained constant, where p is some as yet unknown factor.

$$\text{Then} \quad \left(\frac{\partial \Gamma}{\partial U}\right)_{\tau} = ps \quad . \quad . \quad . \quad . \quad . \quad . \quad . \quad (8)$$

where the suffix τ denotes the value during the transient speed increase δU.

From this relation it follows, as indicated in Appendix I, that

$$\left(\frac{\partial \alpha_1}{\partial U}\right)_{\tau} = \left\{\frac{p\tan\alpha_0 - (1-p)\tan\alpha_1 + \tan\alpha_2}{\tan\alpha_0 + \tan\alpha_2}\right\} \frac{\cos^2\alpha_1}{V_a} \quad . \quad . \quad . \quad (9)$$

A similar expression for $(\partial\alpha_1/\partial V_a)_\tau$ could be obtained mathematically by supposing a sudden mass flow increment, in which case the compressor speed would have to adjust itself to accommodate the rate of growth of circulation.

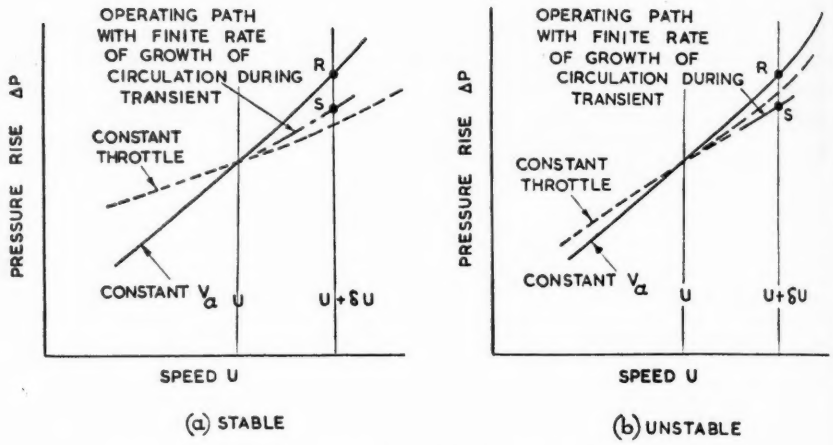

FIGURE 2. Stability of a stage assuming a finite rate of growth of circulation.

An examination of isolated aerofoil data and calculations (*see* Ref. 5 for example) suggests that the circulation would grow very rapidly at first, but would take some time to reach its ultimate value. A value for p somewhere between 0·5 and 0·85 might be expected. Failure of the circulation to attain its full value for constant axial velocity displaces the momentary operating point from R to S, as shown in Fig. 2(*a*). It has been pointed out to the author that this régime is only possible physically if there is a capacity between the compressor and the throttle. Such an assumption is necessarily made although, in studying the stability, any other effects of capacity are neglected. For the example shown in Fig. 2(*a*) the system is still stable, but the displacement may be so large, or the throttle line so orientated, that instability results, as shown in Fig. 2(*b*). The condition for stability which replaces (4) is

$$\left(\frac{\partial \alpha_1}{\partial U}\right)_t < \left(\frac{\partial \alpha_1}{\partial U}\right)_r \quad \text{for stability} \quad . \quad . \quad . \quad . \quad . \quad . \quad (10)$$

$$\text{or} \quad \left(\frac{\partial \alpha_1}{\partial U}\right)_t < \left\{\frac{p \tan \alpha_0 - (1-p)\tan \alpha_1 + \tan \alpha_2}{\tan \alpha_0 + \tan \alpha_2}\right\} \frac{\cos^2 \alpha_1}{V_a} \quad . \quad . \quad (11)$$

If the axial velocity could remain constant during the transient speed increase (*i.e.* $p=1$), the condition for stability would become

$$\left(\frac{\partial \alpha_1}{\partial U}\right)_t < \frac{\cos^2 \alpha_1}{V_a} \quad . \quad . \quad . \quad . \quad . \quad . \quad (12)$$

If the circulation remains constant during the transient speed increase (*i.e.* $p=0$), the condition for stability is given by (13), which follows.

$$\left(\frac{\partial \alpha_1}{\partial U}\right)_t < - \left\{\frac{\tan \alpha_1 - \tan \alpha_2}{\tan \alpha_0 + \tan \alpha_2}\right\} \frac{\cos^2 \alpha_1}{V_a} \quad . \quad . \quad . \quad (13)$$

The latter is clearly the more rigorous condition. As nearly always, reality probably lies between the extremes, and the condition for stage stability will be applied to a multi-stage compressor retaining p as an unknown factor.

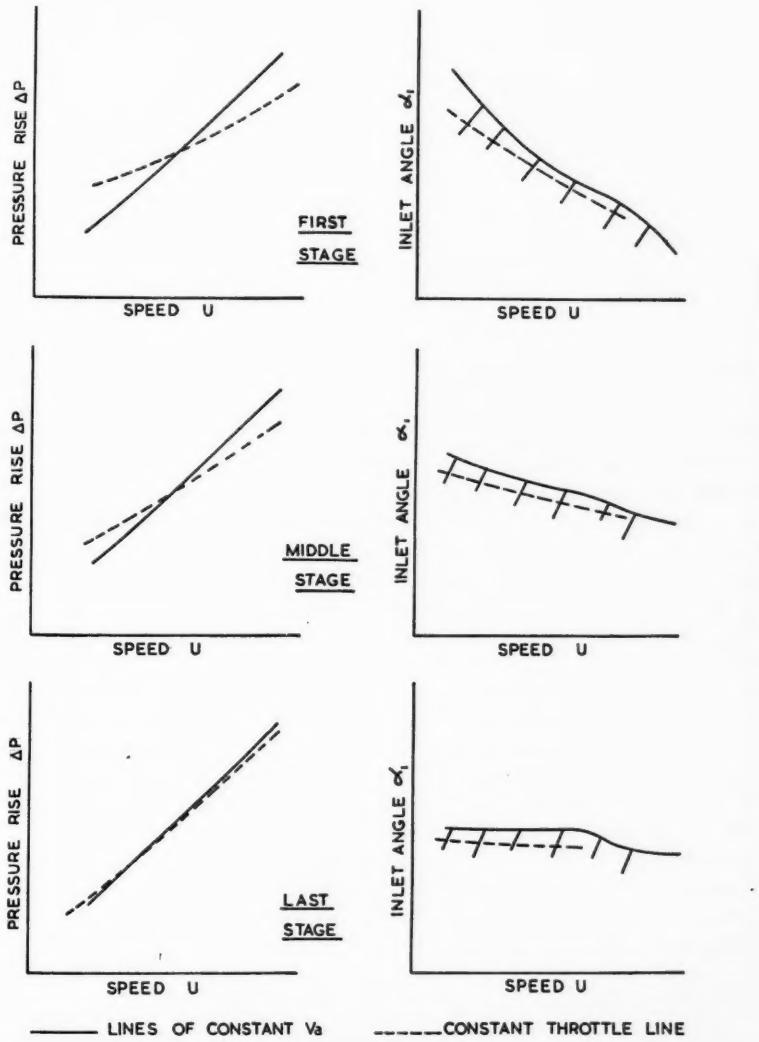

FIGURE 3. Operating conditions for various representative stages in a multi-stage compressor.

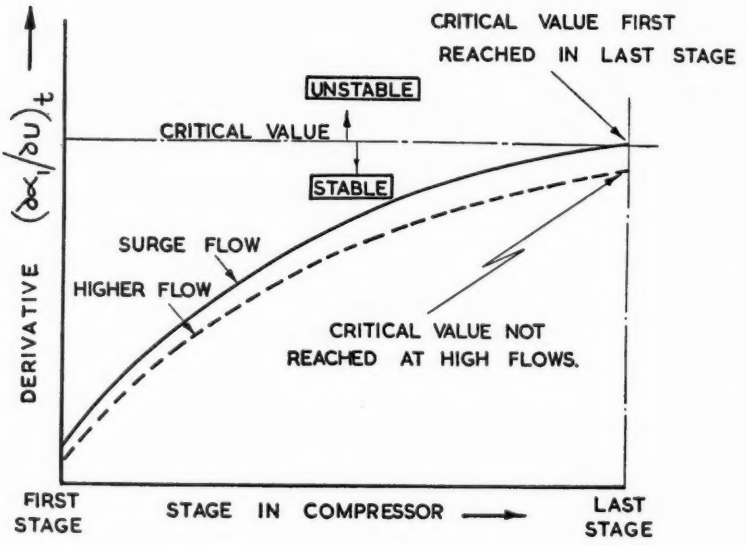

FIGURE 4. Variation of stability derivative $(\partial\alpha_1/\partial U)_t$ through a multi-stage compressor.

2.2. STAGE OPERATING CONDITIONS AND STABILITY OF A MULTI-STAGE MACHINE

It will be appreciated that, for any stage in a multi-stage compressor, the constant throttle operating line will be dictated by the characteristics of the throttle itself plus the characteristics of the remaining stages of the compressor. The throttle and those stages could be regarded as a composite throttle, whose characteristic is different from the simple example, and different for each stage in the compressor. If any stage becomes unstable it is assumed that the compressor as a whole surges. The variation in operating conditions with speed has been given in some detail in Fig. 18 of Ref. 6. In Fig. 3 these have been replotted using the ΔP, U and α_1, U co-ordinates. It can easily be seen from Fig. 3 that $(\partial\alpha_1/\partial U)_t$ will increase from the first to the last stage, as illustrated in Fig. 4. Since the condition for stability in the absence of stalling postulates that this must be less than a given quantity, it follows that critical conditions will always be reached initially in the last stage of the compressor, assuming that it is a normally matched machine with similar blading throughout. Surge will therefore originate in the last stage of the compressor if the type of instability discussed in this paper is the operative one in practice. The conditions pertaining to the last stage before surge will correspond to those illustrated in Fig. 2(*a*), the surge point being transition from the conditions in Fig. 2(*a*) to those in Fig. 2(*b*).

It may be noted that the last stage has been singled out as the critical stage for a compressor in which no stage stalls. In an actual compressor the first stage or stages will stall, and the simple analysis adopted in this paper will no longer apply. However, Pearson and Bowmer[4] have shown that the orientation of the constant

throttle and constant axial velocity characteristics of these stages usually satisfies stability when a unique characteristic is employed. Assuming finite rate of growth of circulation (and separation) will make stalled stages more stable, so no generality appears to be lost. Attention is therefore concentrated on the last stage.

It will be convenient to consider in the first instance pressure ratios greater than 2:1. This implies a choked throttle orifice, so that if losses in the outlet ducting system are neglected the constant throttle lines can be defined analytically by

$$\frac{W\sqrt{(T_{II})}}{P_{II}} = \text{constant}, \quad . \quad . \quad . \quad . \quad . \quad (14)$$

where W is the mass flow and T_{II} and P_{II} are respectively the outlet temperature and pressure from the compressor.

It is shown in Appendix II that in these circumstances

$$\left(\frac{\partial \alpha_1}{\partial U}\right)_t = \left\{1 - \frac{U}{2T_{II}}\left(\frac{\partial \Delta T}{\partial U}\right)_t\right\} \frac{\cos^2 \alpha_1}{V_a} \quad . \quad . \quad . \quad (15)$$

By substituting this value of $(\partial \alpha_1/\partial U)_t$ in (11) the condition of stability becomes

$$\tfrac{1}{2}\frac{U}{T_{II}}\left(\frac{\partial \Delta T}{\partial U}\right)_t > (1-p)\left\{\frac{\tan \alpha_0 + \tan \alpha_1}{\tan \alpha_0 + \tan \alpha_2}\right\} \quad . \quad . \quad . \quad (16)$$

It can be seen that if the simple approach is followed, based on an instantaneous change of circulation corresponding to a constant axial velocity during the transient speed change (*i.e.* $p = 1{\cdot}0$), then the condition for stability is

$$\left(\frac{\partial \Delta T}{\partial U}\right)_t > 0 \quad . \quad . \quad . \quad . \quad . \quad . \quad (17)$$

This is an obvious condition which could have been written down directly, but it supports the method of analysis adopted in this paper when it is applied to a simple case. Examination of any compressor test result shows that this condition is not nearly approached at surge, and stability will be investigated for values of p less than unity.

Along any constant throttle line it is possible to write

$$\frac{\Delta T}{\tfrac{1}{2}U^2} = F + f(U), \quad . \quad . \quad . \quad . \quad . \quad (18)$$

where F is a constant depending on the throttle setting, and $f(U)$ is some function of U which represents the effect of speed on the matching. With this assumption $(\partial \Delta T/\partial U)_t$ can be calculated. Substituting this value in (16), the condition for stability of the last stage, and hence of the compressor as a whole, becomes (*see* Appendix II) that given in (19), which follows.

$$\left[\frac{V_a}{U}\right]_{\text{last stage}} > \frac{(1-p)\,T_{II}}{\{\Delta T + \frac{1}{4}U^3 f'(U)\}} \frac{1}{(\tan\alpha_0 + \tan\alpha_2)} \quad . \quad . \quad (19)$$

where $f'(U)$ is the derivative of $f(U)$ with respect to U. By means of this condition the stability of any point on a characteristic can be tested. The surge point is the highest flow at which instability is found. The expression would not apply to pressure ratios below 2:1, and even at this pressure ratio ducting losses may be playing a significant rôle. At medium speeds, when the throttle is just not choked, no simple analysis seems possible, but at very low speeds a constant throttle line can be represented by

$$\Delta P = kV_a^2 \quad . \quad . \quad . \quad . \quad . \quad . \quad (20)$$

In this case the condition for stability becomes

$$\left[\frac{V_a}{U}\right]_{\text{last stage}} > \frac{(1-p)}{(\tan\alpha_0 + \tan\alpha_2)} \text{ (approximately).} \quad . \quad . \quad (21)$$

For the range of values for α_0 and α_2 used in practice, and if p is limited to the range of values already suggested (and more particularly if limited to the practical values determined later), then the flow coefficient for instability will be very small. This does not exclude any other form of flow breakdown, such as separation and rotating stall, which could occur at higher flows and in the practical range. In fact this does occur, so that according to this hypothesis there must be a fundamental difference in the mechanism of "surge" at high speeds compared with that at low speeds or with incompressible flow.

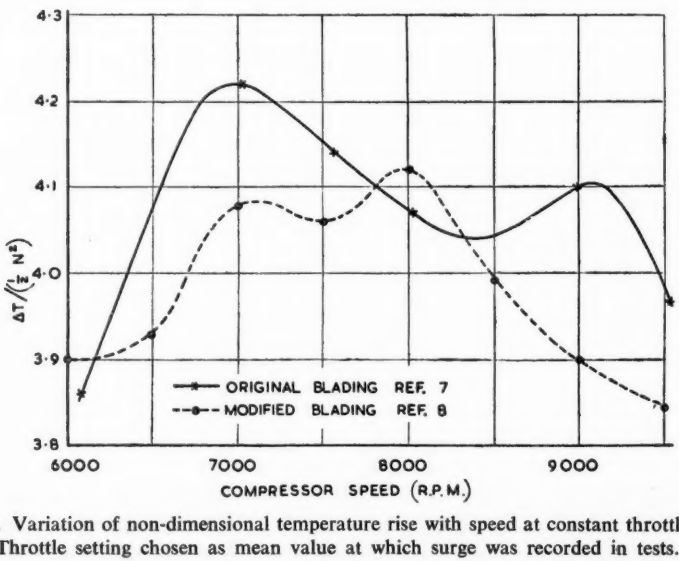

FIGURE 5. Variation of non-dimensional temperature rise with speed at constant throttle setting. Throttle setting chosen as mean value at which surge was recorded in tests.

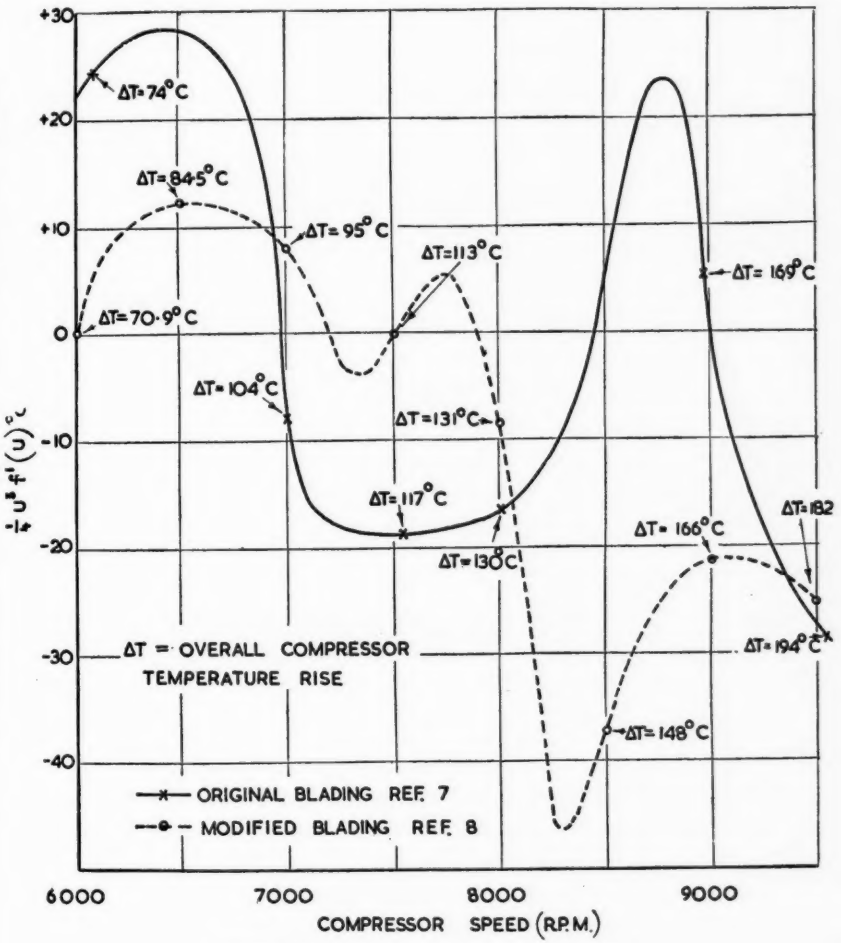

FIGURE 6. Variation of term $\frac{1}{4}U^3 f'(U)$ with speed.

3. Comparison with Test Results and Discussion

Very few compressor test results have been published in sufficient detail to facilitate a direct comparison of theory and experiment. One such set of results is given in Ref. 7 and another set is given (in less detail) on the same compressor, but with some blading modifications, in Ref. 8. The same value of p should therefore apply to both cases and enable a direct check to be made on the known factors in the condition for stability.

In making comparisons it must be noted that the tests were carried out at wide speed increments (though not at all wide by normal standards), so that the calculation of the function $f(U)$, and more particularly its derivative $f'(U)$, is open to some

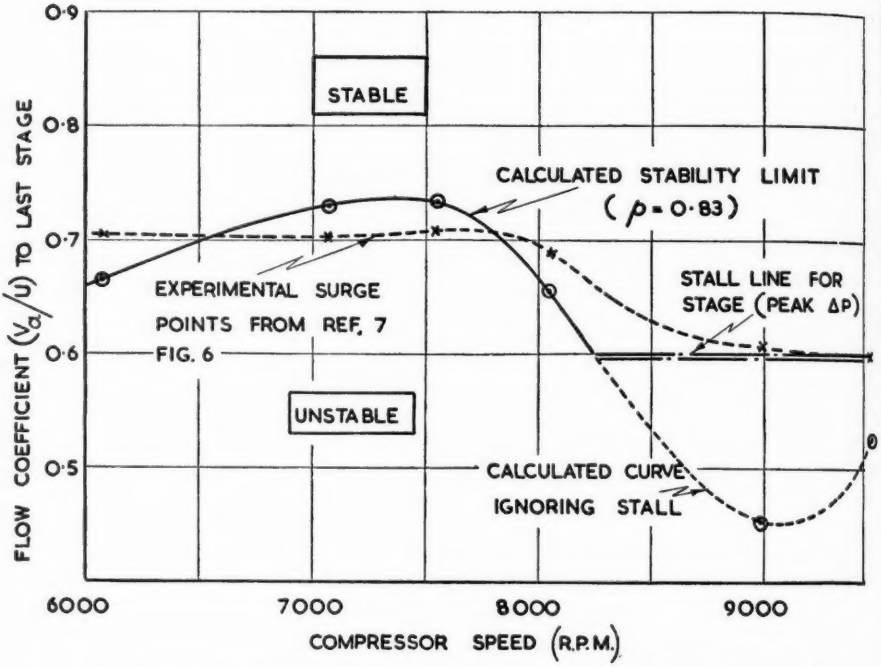

FIGURE 7. Comparison of calculated and measured surge points on basis of flow coefficient to last stage for compressor of Ref. 7.

error. The function $f(U)$, together with the test points by which it is defined, has been plotted for both compressors in Fig. 5, and the derivatives are shown in Fig. 6 to illustrate the errors involved. In Figs. 7 and 8 a direct comparison is made between calculated and measured flow coefficients at entry to the last stage corresponding to surge.

At high speeds the calculated value of the flow coefficient lies in the stall region of the stage. Consequently $(\partial\alpha_0/\partial U)_t$ will not be constant, as assumed in the analysis. Numerical work is impossible, although it can be seen qualitatively that the value of the flow coefficient at which instability is first reached will be increased by stalling. Consequently it is assumed in Figs. 7 and 8 that stalling of the last stage itself represents a surge limit, an assumption which is confirmed by many results on 50 per cent reaction compressors.

It will be seen that good agreement between the calculated and measured flow coefficients is obtained at other speeds. The general shape of the curves would lend confirmation to the theoretical criterion. Particular attention is drawn to the hump in both the curves in Fig. 8 between 8,000 and 8,500 r.p.m. One or two more test points would have confirmed the correlation, but the values at 8,500 r.p.m. are so exceptional that the chances of coincidence are small. In these circumstances it is

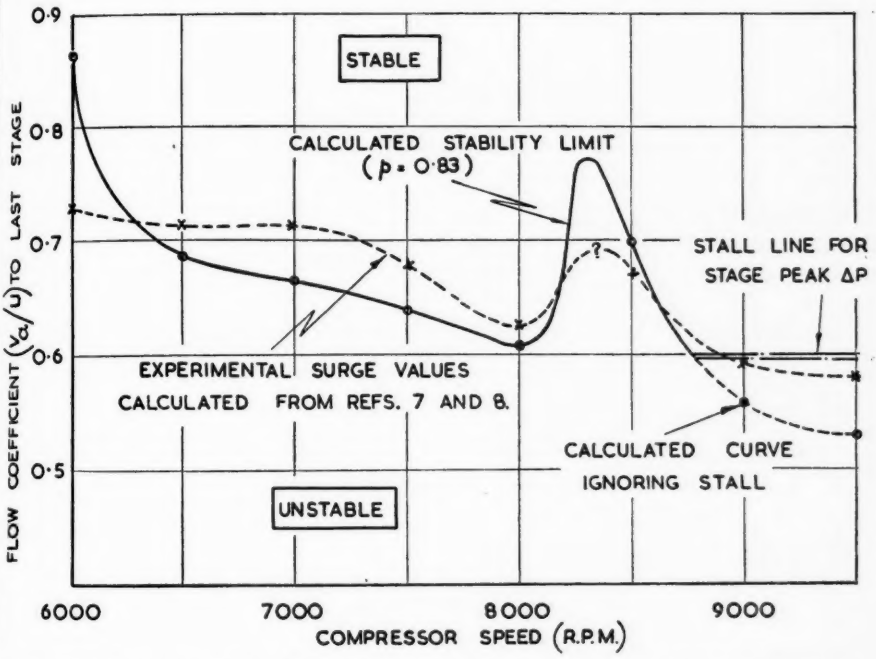

FIGURE 8. Comparison of calculated and measured surge points on basis of flow coefficient to last stage for compressor of Ref. 8.

claimed that the test results confirm the hypothesis advanced in this paper. Closer agreement cannot be expected until more detailed test results are available on the unsurged performance (or more reliable methods of calculating it). The function $f'(U)$ could then be estimated accurately. In this connection it is interesting to note that agreement is closest where the function $f(U)$ is most accurately defined. Such regions include the hump already referred to and the speed range 7,000 to 8,000 r.p.m. of the comparison made in Fig. 7.

Clearly the general level of the calculated curves is directly proportional to the empirical factor $(1-p)$ and in that respect any correlation is meaningless. The value of 0·83 taken for p suggests that the circulation has in fact changed considerably, perhaps somewhat more than might at first be expected. However, in Fig. 9 the rate of growth of circulation round an isolated aerofoil (taken from Ref. 5) has been plotted and the relevant value of p indicated. It shows a remarkable coincidence with the flattening of the curve, that is with the value of the circulation which would be maintained for some time during a transient.

The theory presented in this paper differs from previous work in two respects. The major difference is the assumption of a finite rate of growth of circulation during the small speed increase by which the stability is studied. The second difference is

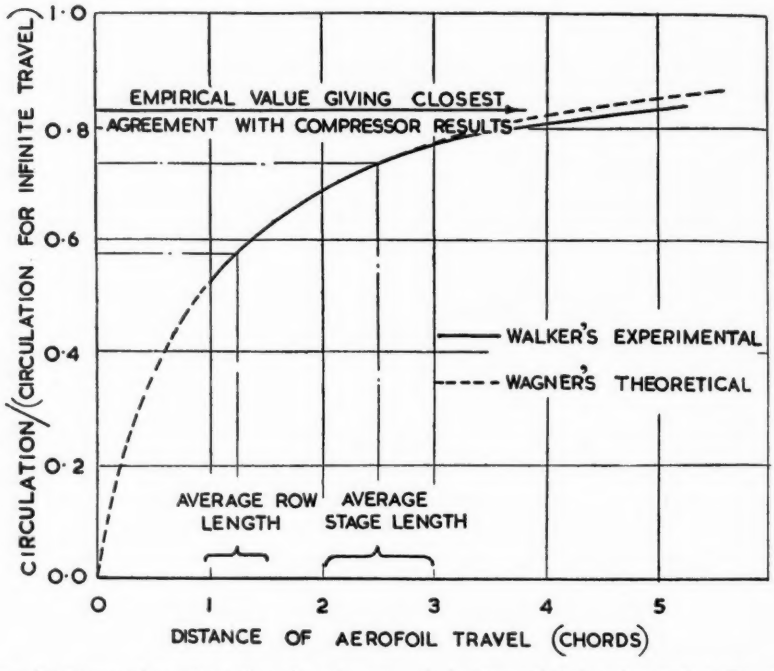

FIGURE 9. Range of possible values for p based on isolated aerofoil data (*see* Ref. 5, Fig. 181).

one of means rather than principle and involves the examination of the effect of small speed changes rather than small mass flow changes. It is essentially a one-dimensional theory.

A consequential difference is that, apart from the fact that changes in work done and efficiency, particularly in the earlier stages of a machine, may considerably alter the shape of the constant throttle lines, stalling does not play any direct rôle in the phenomenon. The instability itself originates, at least at certain speeds, in the unstalled last stage, whereas the stalled first stages have hitherto been held responsible. At these speeds agreement between theory and experiment is best.

It is most probable that a complete theory would have to include capacity inertia and so on, along the lines followed by Pearson and Bowmer[4], the rate of growth of circulation being introduced by a phase lag, dependent on frequency parameter. However, the simpler approach adopted in this note has enabled the rate of growth of circulation to be included, while still avoiding computational difficulties. This does appear to result in a reasonable agreement between theory and experiment in the cases examined; also it throws up some additional qualitative points. For example, the physical difference between the "surge" of multi-stage compressors and the "surge" of single-stage compressors or pumps (*i.e.* compressors operating on an incompressible fluid as at low speeds) is not unknown experimen-

tally, although it has always been difficult to define formally. The surge of a multi-stage compressor at the speeds in question is often violent: it is certainly unmistakable. More particularly, the surge is usually manifest, if allowed to continue, by a series of thumps corresponding to a sudden pressure drop, a gradual recovery, followed by another drop, and so on. There are usually some $\frac{1}{2}$ to 2 cycles per second, often corresponding to the frequency of the whole system as a Helmholtz resonator. By contrast the surge of a single-stage compressor or pump is often difficult to determine, although this may be largely a matter of the pressure magnitudes involved. An essential difference is that the surge of a single-stage compressor or pump is characterised by a drop of pressure but no recovery. The surged flow is stable, although not usually axially symmetrical.

One final comment: experience with part-load performance estimation by the method of Ref. 9 has shown that compressors are extremely fickle in the form of the curve of $\Delta T/(\frac{1}{2}N^2)$ against N that they produce. Quite small changes in this curve could considerably affect its derivative and hence, if this hypothesis is correct, the shape of the surge line. Failure to obtain either qualitative or quantitative correlation of surge behaviour with the major performance parameters is not therefore surprising.

The main object of this paper is a study of the effects of rate of growth of circulation on the stability criteria for axial flow compressors. Although supporting evidence has been produced, the theory cannot be regarded as verified. Hence no attempt is made to examine any practical consequences arising from the stability criterion.

4. Conclusions

A study has been made of the flow stability in multi-stage axial compressors. A hypothesis has been advanced from which a criterion for the stability of a stage has been established. The method of approach differs from previous work in that a finite rate of growth of circulation is postulated. It has also been found necessary to study the stability with respect to speed changes rather than the usual mass flow increment. The criterion so determined has been applied to multi-stage compressors. It has been concluded that instability will always originate in the last stage, even though that stage is unstalled. It has been necessary to introduce one empirical factor into the analysis but, when this is given a value compatible with other experimental and theoretical evidence, reasonably good agreement with experimental results is obtained. Additionally, some peculiarities noted in both the theoretical and experimental curves is strong *prima facie* evidence in favour of the hypothesis. Finally it is suggested that the surge of a multi-stage compressor is a different physical phenomenon from the surge or stall of low speed compressors or pumps.

References

1. Kearton, W. J. *Turbo-Blowers and Compressors.* Pitman, London, 1926.

2. Den Hartog, J. P. *Mechanical Vibrations.* McGraw-Hill, 1940.

3. BULLOCK, R. O., WILCOX, W. W. and MOSES, J. J. Experimental and Theoretical Studies of Surging in Continuous-Flow Compressors. N.A.C.A. Report 861, 1946.

4. PEARSON, H. and BOWMER, T. Surging of Axial Compressors. *The Aeronautical Quarterly*, Vol. I, November 1949.

5. GOLDSTEIN, S. (Editor). *Modern Developments in Fluid Dynamics.* Clarendon Press, Oxford. Vol. II, p. 458, 1938.

6. CARTER, A. D. S. and KILPATRICK, D. A. Self-Excited Vibration of Axial-Flow Compressor Blades. *Proceedings of the Institution of Mechanical Engineers*, Vol. 171, No. 7, 1957.

7. CARTER, A. D. S., ANDREWS, S. J. and FIELDER, E. A. The Design and Testing of an Axial Compressor having a Mean Stage Temperature Rise of 30°C. R. & M. 2985, 1957.

8. CONSTANT, H. Pyestock's Contribution to Propulsion. *Journal of the Royal Aeronautical Society*, Vol. 62, April 1958.

9. HOWELL, A. R. and BONHAM, R. P. Overall and Stage Characteristics of Axial Flow Compressors. *Proceedings of the Institution of Mechanical Engineers*, Vol. 163, 1950.

Appendix I

STABILITY CONDITIONS FOR A STAGE

Four variables are used to define the operating point of a stage. These are the representative blade speed U, the fluid axial velocity V_a, the pressure rise ΔP, and the throttle position which can be denoted by "t." Of these quantities only two are independent. Let U and V_a be the independent variables. Then for any small change

$$\delta\Delta P = \left(\frac{\partial \Delta P}{\partial U}\right)_{V_a} \delta U + \left(\frac{\partial \Delta P}{\partial V_a}\right)_{U} \delta V_a \quad . \quad . \quad . \quad (22)$$

where, in general, the throttle position would have to assume a value compatible with this change, given by a similar expression.

Since δU and δV_a are independent, they can be chosen in such a way that ΔP remains constant (*i.e.* $\delta\Delta P = 0$). Equation (22) then becomes

$$\left(\frac{\partial \Delta P}{\partial V_a}\right)_{U} \left(\frac{\partial V_a}{\partial U}\right)_{\Delta P} \left(\frac{\partial U}{\partial \Delta P}\right)_{V_a} = -1.$$

In an unstalled stage $(\partial \Delta P / \partial V_a)_U$ is negative and $(\partial V_a / \partial U)_{\Delta P}$ is positive; hence $(\partial \Delta P / \partial U)_{V_a}$ is always positive under these conditions.

It can also be specified that δU and δV_a be chosen in such a way that "t" is maintained constant. In this case equation (22) becomes

$$\left(\frac{\partial \Delta P}{\partial V_a}\right)_t = \left(\frac{\partial \Delta P}{\partial U}\right)_{V_a} \left(\frac{\partial U}{\partial V_a}\right)_t + \left(\frac{\partial \Delta P}{\partial V_a}\right)_U \quad . \quad . \quad . \quad . \quad (23)$$

$$\text{But} \quad \left(\frac{\partial U}{\partial V_a}\right)_t = \left(\frac{\partial \Delta P}{\partial V_a}\right)_t \left(\frac{\partial U}{\partial \Delta P}\right)_t \quad . \quad . \quad . \quad . \quad . \quad . \quad . \quad (24)$$

Hence, substituting in (23),

$$\left(\frac{\partial \Delta P}{\partial V_a}\right)_t - \left(\frac{\partial \Delta P}{\partial V_a}\right)_U = \left(\frac{\partial \Delta P}{\partial U}\right)_{V_a}\left(\frac{\partial \Delta P}{\partial V_a}\right)_t\left(\frac{\partial U}{\partial \Delta P}\right)_t \quad . \quad . \quad (25)$$

$$\text{or } 1 - \frac{(\partial \Delta P/\partial V_a)_U}{(\partial \Delta P/\partial V_a)_t} = \frac{(\partial \Delta P/\partial U)_{V_a}}{(\partial \Delta P/\partial U)_t} \quad . \quad . \quad . \quad . \quad . \quad (26)$$

Hence if the stage remains unstalled the condition for stability

$$\left(\frac{\partial \Delta P}{\partial V_a}\right)_t > \left(\frac{\partial \Delta P}{\partial V_a}\right)_U \quad . \quad . \quad . \quad . \quad . \quad (27)$$

becomes

$$\left(\frac{\partial \Delta P}{\partial U}\right)_t < \left(\frac{\partial \Delta P}{\partial U}\right)_{V_a} \quad . \quad . \quad . \quad . \quad . \quad (28)$$

The stage pressure rise ΔP will be given by

$$\frac{\Delta P}{\frac{1}{2}\rho U^2} = gJK_p\eta\,\frac{\Delta T_s}{\frac{1}{2}U^2} \quad . \quad . \quad . \quad . \quad . \quad (29)$$

where ρ is the density at inlet and η is the stage efficiency. In the unstalled range η can be taken as constant, so that the condition (28) for stability becomes

$$\left(\frac{\partial \Delta T_s}{\partial U}\right)_t < \left(\frac{\partial \Delta T_s}{\partial U}\right)_{V_a}, \quad . \quad . \quad . \quad . \quad . \quad (30)$$

where the stage temperature rise is given by

$$\Delta T_s = \frac{\Omega U V_a}{gJK_p}(\tan\alpha_1 - \tan\alpha_2) = \frac{\Omega U^2}{gJK_p}\,\frac{(\tan\alpha_1 - \tan\alpha_2)}{(\tan\alpha_1 + \tan\alpha_0)} \quad . \quad . \quad (31)$$

Differentiation with respect to U gives

$$\frac{\partial \Delta T_s}{\partial U} = \frac{2\Omega U}{gJK_p}\,\frac{(\tan\alpha_1 - \tan\alpha_2)}{(\tan\alpha_1 + \tan\alpha_0)} + \frac{\Omega U^2}{gJK_p}\,\frac{(\tan\alpha_0 + \tan\alpha_2)}{(\tan\alpha_1 + \tan\alpha_0)^2}\sec^2\alpha_1\,\frac{\partial \alpha_1}{\partial U} \quad . \quad (32)$$

Hence, considering this as taken at constant throttle and constant axial velocity conditions, the condition for stability can be written as

$$\left(\frac{\partial \alpha_1}{\partial U}\right)_t < \left(\frac{\partial \alpha_1}{\partial U}\right)_{V_a} \quad . \quad . \quad . \quad . \quad . \quad . \quad . \quad . \quad (33)$$

provided that $(\tan\alpha_0 + \tan\alpha_2) > 0$ . . . . . (34)

The condition (34) will be satisfied in all normal axial compressors.

Additionally, condition (33) may be deduced as an aerodynamic flow instability as follows.

With the stage operating in equilibrium suppose that the speed is suddenly increased by a small amount. Let the mean blade speed increase by δU from U to $(U+\delta U)$. Momentarily the mass flow, and therefore the axial velocity, will remain unchanged. The blade incidence will consequently suddenly increase, and a new operating point not on the constant throttle line will be established. The change of incidence or fluid inlet angle will be given by

$$\delta\alpha_1 = \left(\frac{\partial \alpha_1}{\partial U}\right)_{V_a} \delta U. \quad . \quad . \quad . \quad . \quad . \quad (35)$$

As the mass flow, or axial velocity, increases to that demanded by the new speed, the inlet angle will decrease. It follows that

$$\delta\alpha_1 > \triangle\alpha_1 \text{ for stability} \quad . \quad . \quad . \quad . \quad (36)$$

where $\triangle\alpha_1$ is the ultimate change of fluid inlet angle to the constant throttle operating point. If this condition were not satisfied a state would be reached in which the actual operating fluid inlet angle was less than that for the equilibrium point. As the mass flow increased the inlet angle would decrease further, and equilibrium could never be achieved.

We can write

$$\triangle\alpha_1 = \left(\frac{\partial \alpha_1}{\partial U}\right)_t \delta U \quad . \quad . \quad . \quad . \quad . \quad (37)$$

Then substituting in the inequality (36) gives

$$\left(\frac{\partial \alpha_1}{\partial U}\right)_t < \left(\frac{\partial \alpha_1}{\partial U}\right)_{V_a} \quad . \quad . \quad . \quad . \quad . \quad . \quad (38)$$

which is condition (33).

If a finite rate of growth of circulation during a transient speed increase is assumed the condition (33) or (38) must be rewritten

$$\left(\frac{\partial \alpha_1}{\partial U}\right)_t < \left(\frac{\partial \alpha_1}{\partial U}\right)_\Gamma \text{ for stability.} \quad . \quad . \quad . \quad (39)$$

Now the circulation Γ round a blade is given by

$$\Gamma = s(V_{w1} - V_{w2}) = sV_a(\tan\alpha_1 - \tan\alpha_2), \quad . \quad . \quad . \quad (40)$$

whence

$$\frac{\partial \Gamma}{\partial U} = sV_a \sec^2\alpha_1 \frac{\partial \alpha_1}{\partial U} + s(\tan\alpha_1 - \tan\alpha_2)\frac{\partial V_a}{\partial U} \quad . \quad . \quad . \quad (41)$$

From the velocity triangles at inlet

$$U = V_a \tan\alpha_1 + V_a \tan\alpha_0 \quad . \quad . \quad . \quad . \quad . \quad (42)$$

and so
$$\left(\frac{\partial \alpha_1}{\partial U}\right)_{V_a} = \frac{\cos^2 \alpha_1}{V_a} \quad . \quad . \quad . \quad . \quad . \quad . \quad (43)$$

whence, substituting (4) with $\partial V_a = 0$,

$$\left(\frac{\partial \Gamma}{\partial U}\right)_{V_a} = s. \quad . \quad . \quad . \quad . \quad . \quad . \quad . \quad (44)$$

Now assume that
$$\left(\frac{\partial \Gamma}{\partial U}\right)_r = p\left(\frac{\partial \Gamma}{\partial U}\right)_{V_a} = ps. \quad . \quad . \quad . \quad . \quad (45)$$

Then equation (41) yields

$$\left(\frac{\partial V_a}{\partial U}\right)_r = \frac{p - V_a \sec^2 \alpha_1 \, (\partial \alpha_1 / \partial U)_r}{(\tan \alpha_1 - \tan \alpha_2)} \quad . \quad . \quad . \quad . \quad (46)$$

Also equation (42) gives

$$\left(\frac{\partial V_a}{\partial U}\right)_r = \frac{1 - V_a \sec^2 \alpha_1 \, (\partial \alpha_1 / \partial U)_r}{(\tan \alpha_1 + \tan \alpha_0)} \quad . \quad . \quad . \quad . \quad (47)$$

Hence, equating (46) and (47),

$$\left(\frac{\partial \alpha_1}{\partial U}\right)_r = \left\{\frac{p \tan \alpha_0 - (1-p) \tan \alpha_1 + \tan \alpha_2}{\tan \alpha_0 + \tan \alpha_2}\right\} \frac{\cos^2 \alpha_1}{V_a} \quad . \quad . \quad (48)$$

and the condition (39) for stability becomes

$$\left(\frac{\partial \alpha_1}{\partial U}\right)_t < \left\{\frac{p \tan \alpha_0 - (1-p) \tan \alpha_1 + \tan \alpha_2}{\tan \alpha_0 + \tan \alpha_2}\right\} \frac{\cos^2 \alpha_1}{V_a} \quad . \quad . \quad (49)$$

Appendix II

Stability Conditions for a Multi-Stage Compressor

It will be assumed that the outlet throttle is choked, as at pressure ratios above about 2:1. Then if all losses in the outlet ducting system are neglected the constant throttle line will be defined by

$$\frac{W\sqrt{(T_{II})}}{P_{II}} = \text{constant.} \quad . \quad . \quad . \quad . \quad . \quad . \quad (50)$$

Also $W = \rho A V_a$, for continuity, . . . (51)

and $P_{II} = \rho R T_{II}$, ... (52)

whence, for the last stage,
$$V_a = k\sqrt{(T_{II})} \, . \quad . \quad . \quad . \quad . \quad . \quad . \quad (53)$$

At inlet to the last stage,

$$U=V_a(\tan\alpha_1+\tan\alpha_0), \quad . \quad . \quad . \quad . \quad . \quad . \quad . \quad . \quad (54)$$

whence, considering the flow in the ultimate state when all transients have disappeared,

$$\frac{\partial\alpha_1}{\partial U}=\left\{1-\left(\frac{\partial V_a}{\partial U}\right)_t(\tan\alpha_1+\tan\alpha_0)\right\}\frac{\cos^2\alpha_1}{V_a}$$

$$=\left\{1-\frac{U}{V_a}\left(\frac{\partial V_a}{\partial U}\right)_t\right\}\frac{\cos^2\alpha_1}{V_a} \quad . \quad . \quad . \quad . \quad . \quad . \quad . \quad (55)$$

Substituting $$V_a=k\sqrt{(T_{II})}=k\sqrt{(T_I+\Delta T)}, \quad . \quad . \quad . \quad . \quad . \quad . \quad . \quad (56)$$

where ΔT is the overall compressor temperature rise, gives for the last stage

$$\left(\frac{\partial\alpha_1}{\partial U}\right)_t=\left\{1-\frac{U}{2T_{II}}\left(\frac{\partial\Delta T}{\partial U}\right)_t\right\}\frac{\cos^2\alpha_1}{V_a} \quad . \quad . \quad . \quad . \quad . \quad . \quad (57)$$

Substitute in the condition for stability given at (45) of Appendix I; then

$$\left\{1-\frac{U}{2T_{II}}\left(\frac{\partial\Delta T}{\partial U}\right)_t\right\}<\left\{\frac{p\tan\alpha_0-(1-p)\tan\alpha_1+\tan\alpha_0}{\tan\alpha_0+\tan\alpha_2}\right\} \quad . \quad . \quad . \quad . \quad . \quad (58)$$

or $$-\tfrac{1}{2}\frac{U}{T_{II}}\left(\frac{\partial\Delta T}{\partial U}\right)_t<-(1-p)\left\{\frac{\tan\alpha_0+\tan\alpha_1}{\tan\alpha_0+\tan\alpha_2}\right\} \quad . \quad . \quad . \quad . \quad . \quad . \quad (59)$$

To evaluate the overall temperature rise at various speeds for constant throttle setting it is convenient to write

$$\frac{\Delta T}{\tfrac{1}{2}U^2}=F+f(U) \text{ along the constant throttle line.} \quad . \quad . \quad . \quad . \quad (60)$$

Then $$\left(\frac{\partial\Delta T}{\partial U}\right)_t=UF+Uf(U)+\tfrac{1}{2}U^2f'(U) \quad . \quad . \quad . \quad . \quad . \quad . \quad (61)$$

and $$\tfrac{1}{2}\frac{U}{T_{II}}\left(\frac{\partial\Delta T}{\partial U}\right)_t=\frac{\Delta T+\tfrac{1}{4}U^3f'(U)}{T_{II}} \quad . \quad . \quad . \quad . \quad . \quad . \quad . \quad . \quad (62)$$

The condition for stability in (59) then becomes

$$\frac{\tan\alpha_0+\tan\alpha_1}{\tan\alpha_0+\tan\alpha_2}<\frac{1}{(1-p)}\frac{\Delta T+\tfrac{1}{4}U^3f'U}{T_{II}} \quad . \quad . \quad . \quad . \quad (63)$$

or $$\left[\frac{V_a}{U}\right]_{\text{last stage}}>\frac{(1-p)\,T_{II}}{\Delta T+\tfrac{1}{4}U^3f'(U)}\frac{1}{(\tan\alpha_0+\tan\alpha_2)}.$$

Asymmetrically Plate-Reinforced Circular Hole in a Uniformly End-Loaded Flat Plate

RAYMOND HICKS, Ph.D., M.Sc.

(G.E.C. Simon-Carves Atomic Energy Group)

SUMMARY: General expressions are obtained for the stress distribution in a flat plate end-loaded by equal principal stresses and containing a circular hole reinforced by an annular plate. The reinforcement is placed on one side of the plate only so that the other side remains flush. It is shown that the effect of an asymmetrically placed reinforcement is to induce, in the plate and reinforcement, bending stresses which are not negligible compared with the externally applied direct stress. From particular examples it is found that reinforcements having practical dimensions can give rise to stress concentrations in the same order of magnitude as those in a similarly loaded plate containing an unreinforced hole. For practical purposes, data have been obtained which enable the designer to determine quickly the stress distributions associated with reinforcements and plates having a reasonably wide range of dimensions.

1. Introduction

The problem of a symmetrically reinforced hole in an end-loaded plate has been considered by Timoshenko[1], Gurney[2] and many others, for example in Refs. 3, 4, 5, 6. Timoshenko used a compact ring as a reinforcement, the radial width of which was small compared with the diameter of the hole. This implies that, in the plane of the plate, the bending stiffness of the reinforcement is small and the corresponding shear stresses negligible. Gurney used a relatively thin annular plate as a reinforcement and determined the stress distribution in the reinforcement, as well as the plate, for various stress systems applied at infinity.

Mansfield[7] and the author[8] have considered the problem of a variably reinforced circular hole in an end-loaded plate, the variation in the cross-sectional area being chosen so that the tensile resistance of the reinforcement increases at points around the hole where the stresses in the plate tend to be high.

Elsewhere, the author[9] has considered the problem of an asymmetrically ring-reinforced circular hole in an end-loaded infinite flat plate. That is, a reinforcement whose radial width is small compared with the diameter of the hole, so that it has no radial stress variation. In this case it is found that the asymmetry of the reinforcement has two effects on the stress distribution in the plate. Firstly, bending stresses are induced in the plate and reinforcement. In general it is found that, for the plate, these bending stresses are less than the corresponding stresses in a plate with the relatively thin annular type of reinforcement considered

Received November 1958.

here. Secondly, for a given area of cross section, the asymmetrical reinforcement is less effective in reducing the stress concentration at the middle plane of the plate than a corresponding symmetrical reinforcement. This follows from the fact that elements of the asymmetrical reinforcement adjacent to the plate are elongated tangentially by bending of the reinforcement as well as by hoop stresses, and this results in less resistance to radial displacements of the plate around the hole. As shown later, the asymmetry of a plate reinforcement considered here has no effect on the stress distribution at the middle plane of the plate.

This analysis deals with the problem of a circular hole in a flat plate uniformly loaded in its own plane by equal principal stresses applied at the boundary. The hole is reinforced by an annular plate having a radial width which is not small compared with the diameter of the hole. That is, there is a radial variation in the stresses acting at the middle plane of the reinforcement; furthermore, this variation is the same as the well-known radial variation for thick cylinders.

The reinforcement is located on one side of the plate only (Fig. 1), so that the other side remains flush. This implies that bending moments are induced in the structure at the junction of the reinforcement and plate, since the middle plane of the plate does not coincide with the middle plane of the reinforcement. Also, since practical reinforcements may be several times as thick as the plate, it follows that the magnitude of these stresses may be high. That is, in the same order of magnitude as the stresses at the middle plane of the plate.

As would be expected, for a plate under the combined action of bending and end load, the bending stress concentrations are not linearly related to the applied stress but become relatively more severe as the stress at the middle plane of the plate increases. For example, for a plate reinforced so that the stress distribution at the middle plane is the same as the stress distribution in a similarly loaded plate with no hole, the radial bending stress in the plate adjacent to the reinforcement is practically equal to the stress at the middle plane of the plate when the applied stress is 17,200 lb./in^2. That is, for this particular example, the resultant stress concentration in the plate with an asymmetrical hole is the same as the stress concentration in a similarly loaded plate with an unreinforced hole.

A general solution is obtained for an annular plate with a fixed or simply-supported boundary. This solution is extended to deal with the problem of a similarly loaded infinite plate. It is found that, when the least lateral dimension of a plate is several times the diameter of the hole, the solution for an infinite plate can be applied with sufficient accuracy to a plate of finite size. Furthermore, for any particular problem, the degree of approximation can be determined readily by comparing the stress applied to the boundary of the finite plate to the stresses acting around the corresponding contour in an infinite plate.

For almost all practical problems numerical values for the stress concentrations can only be found by evaluating Bessel functions that are outside the range given in standard works of reference. It has been necessary, therefore, to tabulate data which will enable the designer to evaluate quickly the important stress concentrations for any particular problem within a reasonably wide practical range.

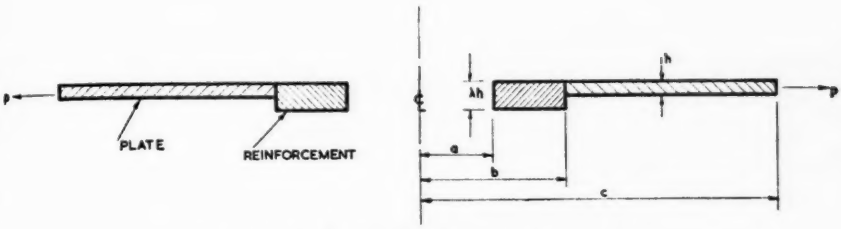

FIGURE 1. Section through plate and reinforcement.

NOTATION

w	deflection of plate
r	radial co-ordinate
ψ	radial slope of plate
h	thickness of plate
a, b	inner and outer radii of annular reinforcement
b, c	inner and outer radii of annular plate
λ	(thickness of reinforcement)/(thickness of plate)
p	applied stress
$\widehat{rr}, \widehat{\theta\theta}$	stress components at the middle plane of the plate
M_r, M_θ	moment components for the plate
Q_r, Q_θ	shear components for the plate
E	Young's modulus
ν	Poisson's ratio
D	flexural rigidity of plate
α_1, β_1	constants defined by equation (2)
α, β	constants defined by $\alpha_1 h/D$ and $\beta_1 h/D$
x	dimensionless parameter $r\sqrt{\alpha}$
$K_n(x), I_n(x)$	Bessel functions
n	order of Bessel function, given by $\sqrt{(1+\beta)}$
C_1, C_2	arbitrary constants
K, S, S_R, T	constants defined by equation (22)
L, P	constants defined by equation (26)
$\phi_P, \phi_R, \phi_\theta$	design parameters defined by equation (34)

Suffix

R	denotes reinforcement.

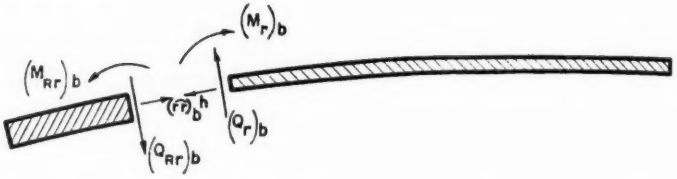

FIGURE 2. Forces and moments interacting between plate and reinforcement.

2. Theory

The stresses acting at the middle plane of the plate (Figs. 1 and 2) are given by the following expressions

$$\left.\begin{aligned} \widehat{rr} &= \alpha_1 + \frac{\beta_1}{r^2} \\ \widehat{\theta\theta} &= \alpha_1 - \frac{\beta_1}{r^2}, \end{aligned}\right\} \qquad (1)$$

where

$$\left.\begin{aligned} \alpha_1 &= \frac{c^2 p - b^2 (\widehat{rr})_b}{(c^2 - b^2)} \\ \beta_1 &= -\frac{b^2 c^2 [p - (\widehat{rr})_b]}{(c^2 - b^2)}. \end{aligned}\right\} \qquad (2)$$

For force equilibrium in a direction normal to the surface of the bent plate,

$$Q_r = -(\widehat{rr})\, h \frac{dw}{dr}. \qquad (3)$$

The negative sign has been inserted to satisfy the convention that downward deflections are positive.

Using the classical theory for bending, equation (3) becomes

$$D \frac{d}{dr}\left(\frac{d^2w}{dr^2} + \frac{1}{r}\frac{dw}{dr}\right) - (\widehat{rr})\, h \frac{dw}{dr} = 0,$$

$$i.e. \qquad D \frac{d}{dr}\left(\frac{d^2w}{dr^2} + \frac{1}{r}\frac{dw}{dr}\right) - \left(\alpha_1 + \frac{\beta_1}{r^2}\right) h \frac{dw}{dr} = 0 \qquad (4)$$

For convenience, let

$$\left.\begin{aligned} \alpha = \alpha_1 h/D, \qquad \beta = \beta_1 h/D, \qquad \psi = dw/dr \\ x = r\sqrt{\alpha}, \qquad n^2 = 1 + \beta. \end{aligned}\right\} \qquad (5)$$

Then equation (4) becomes

$$x^2\frac{d^2\psi}{dx^2}+x\frac{d\psi}{dx}-(x^2+n^2)\psi=0. \quad . \quad . \quad . \quad . \quad . \quad (6)$$

This is a modified Bessel equation of order n; its complete solution is given by

$$\psi=C_1I_n(x)+C_2K_n(x) \quad (n \text{ integer}) \quad . \quad . \quad . \quad (7a)$$

$$\psi=C_1I_n(x)+C_3I_{-n}(x) \quad (n \text{ fractional}) \quad . \quad . \quad . \quad (7b)$$

For the range of problems considered here, n can be fractional or integer. However, it is proposed to use relation (7*a*) for all values of n, it being understood that when n is fractional $K_n(x)$ is given by

$$K_n(x)=\tfrac{1}{2}\pi\frac{[I_{-n}(x)-I_n(x)]}{\sin n\pi} \quad . \quad . \quad . \quad . \quad . \quad (8)$$

Similarly, using the suffix "R" to denote symbols associated with the reinforcement, it can be shown that

$$(\widehat{rr}_{\mathrm{R}})=\alpha_{1\mathrm{R}}+\frac{\beta_{1\mathrm{R}}}{r^2}, \qquad (\widehat{\theta\theta}_{\mathrm{R}})=\alpha_{1\mathrm{R}}-\frac{\beta_{1\mathrm{R}}}{r^2}, \quad . \quad . \quad . \quad (9)$$

where $$\alpha_{1\mathrm{R}}=\frac{b^2(\widehat{rr}_{\mathrm{R}})_b}{(b^2-a^2)}, \quad \beta_{1\mathrm{R}}=-\frac{a^2b^2(\widehat{rr}_{\mathrm{R}})_b}{(b^2-a^2)}, \quad \alpha_{\mathrm{R}}=\frac{\alpha_{1\mathrm{R}}h_{\mathrm{R}}}{D_{\mathrm{R}}}. \quad . \quad . \quad (10)$$

Also, for the reinforcement,

$$\psi_{\mathrm{R}}=C_{\mathrm{R}1}I_{\mathrm{R}n}(x_{\mathrm{R}})+C_{\mathrm{R}2}K_{\mathrm{R}n}(x_{\mathrm{R}}), \quad . \quad . \quad . \quad . \quad (11)$$

where n is fractional or an integer.

3. Boundary Conditions

3.1. General

For compatibility of displacements between reinforcement and plate,

$$(\widehat{\theta\theta}_{\mathrm{R}}-\nu\widehat{rr}_{\mathrm{R}})_b=(\widehat{\theta\theta}-\nu\widehat{rr})_b. \quad . \quad . \quad . \quad . \quad (12)$$

Substituting for $\widehat{\theta\theta}_{\mathrm{R}}$ etc., this gives

$$(\widehat{rr})_b=\frac{\dfrac{2pc^2}{(c^2-b^2)}}{\left[\dfrac{1}{\lambda}\left(\dfrac{b^2+a^2}{b^2-a^2}\right)+\left(\dfrac{b^2+c^2}{c^2-b^2}\right)-\dfrac{\nu}{\lambda}+\nu\right]}, \quad . \quad . \quad (13)$$

where $$\lambda=h_{\mathrm{R}}/h. \quad . \quad . \quad . \quad . \quad . \quad . \quad . \quad . \quad (14)$$

Referring to Fig. 2, for moment equilibrium

$$(M_r)_b = (M_{Rr})_b + (\widehat{rr})_b \frac{h^2}{2}(\lambda - 1), \quad . \quad . \quad . \quad . \quad . \quad (15)$$

that is, $$D\sqrt{\alpha}\left[\frac{d\psi}{dx} + \frac{\nu\psi}{x}\right]_b - D_R\sqrt{\alpha_R}\left[\frac{d\psi_R}{dx_R} + \frac{\nu\psi_R}{x_R}\right] + (\widehat{rr})_b \frac{h^2}{2}(\lambda - 1) = 0. \quad . \quad (16)$$

Around the curve $r = b$, the radial slope of the plate is the same as the radial slope of the reinforcement, so that

$$(\psi)_b = (\psi_R)_b. \quad . \quad . \quad . \quad . \quad . \quad . \quad (17)$$

Also, since the radial moment is zero around the hole,

$$\left[\frac{d\psi_R}{dx_R} + \frac{\nu\psi_R}{x_R}\right]_a = 0. \quad . \quad . \quad . \quad . \quad . \quad . \quad (18)$$

The remaining boundary conditions depend on the manner of supporting the plate and are given in the following sections.

3.2. Simply-Supported Plate

For a simply-supported plate,

$$\left[\frac{d\psi}{dx} + \frac{\nu\psi}{x}\right]_a = 0. \quad . \quad . \quad . \quad . \quad . \quad . \quad (19)$$

In this case the boundary conditions (16), (17), (18), and (19) reduce to

$$\left.\begin{aligned}
&D\sqrt{\alpha}\left\{C_1\left[I_n'(b\sqrt{\alpha}) + \frac{\nu}{b\sqrt{\alpha}} I_n(b\sqrt{\alpha})\right] + C_2\left[K_n'(b\sqrt{\alpha}) + \frac{\nu}{b\sqrt{\alpha}} K_n(b\sqrt{\alpha})\right]\right\} - \\
&\quad - D_R\sqrt{\alpha_R}\left\{C_{R1}\left[I_{Rn}'(b\sqrt{\alpha_R}) + \frac{\nu}{b\sqrt{\alpha_R}} I_{Rn}(b\sqrt{\alpha_R})\right] + \right. \\
&\quad \left. + C_{R2}\left[K_{Rn}'(b\sqrt{\alpha_R}) + \frac{\nu}{b\sqrt{\alpha_R}} K_{Rn}(b\sqrt{\alpha_R})\right]\right\} + (\widehat{rr})_b \frac{h^2}{2}(\lambda - 1) = 0 \\
&\quad C_1 I_n(b\sqrt{\alpha}) + C_2 K_n(b\sqrt{\alpha}) - C_{R1} I_{Rn}(b\sqrt{\alpha_R}) - C_{R2} K_{Rn}(b\sqrt{\alpha_R}) = 0 \\
&C_{R1}\left[I_{Rn}'(a\sqrt{\alpha_R}) + \frac{\nu}{a\sqrt{\alpha_R}} I_{Rn}(a\sqrt{\alpha_R})\right] + \\
&\quad + C_{R2}\left[K_{Rn}'(a\sqrt{\alpha_R}) + \frac{\nu}{a\sqrt{\alpha_R}} K_{Rn}(a\sqrt{\alpha_R})\right] = 0 \\
&C_1\left[I_n'(c\sqrt{\alpha}) + \frac{\nu}{c\sqrt{\alpha}} I_n(c\sqrt{\alpha})\right] + C_2\left[K_n'(c\sqrt{\alpha}) + \frac{\nu}{c\sqrt{\alpha}} K_n(c\sqrt{\alpha})\right] = 0
\end{aligned}\right\} \quad (20)$$

where the primes$^{(\prime)}$ denote differentiation with respect to x.

Solving these equations, it is found that

$$\left.\begin{aligned} C_1 &= -(\widehat{rr})_b \frac{h^2}{2}(\lambda-1)K \\ C_2 &= (\widehat{rr})_b \frac{h^2}{2}(\lambda-1)TK \\ C_{R1} &= -(\widehat{rr})_b \frac{h^2}{2}(\lambda-1)SK \\ C_{R2} &= (\widehat{rr})_b \frac{h^2}{2}(\lambda-1)TS_R K \end{aligned}\right\} \quad . \quad . \quad . \quad . \quad . \quad (21)$$

where

$$\left.\begin{aligned} S_R &= \frac{\left[I_{Rn}'(a\sqrt{\alpha_R}) + \frac{\nu}{a\sqrt{\alpha_R}} I_{Rn}(a\sqrt{\alpha_R})\right]}{\left[K_{Rn}'(a\sqrt{\alpha_R}) + \frac{\nu}{a\sqrt{\alpha_R}} K_{Rn}(a\sqrt{\alpha_R})\right]} \\ S &= \frac{\left[I_n'(c\sqrt{\alpha}) + \frac{\nu}{c\sqrt{\alpha}} I_n(c\sqrt{\alpha})\right]}{\left[K_n'(c\sqrt{\alpha}) + \frac{\nu}{c\sqrt{\alpha}} K_n(c\sqrt{\alpha})\right]} \\ T &= \frac{[I_n(b\sqrt{\alpha}) - SK_n(b\sqrt{\alpha})]}{[I_{Rn}(b\sqrt{\alpha_R}) - S_R K_{Rn}(b\sqrt{\alpha_R})]} \\ \frac{1}{K} &= D\sqrt{\alpha}\left\{\left[I_n'(b\sqrt{\alpha}) + \frac{\nu}{b\sqrt{\alpha}} I_n(b\sqrt{\alpha})\right] - S\left[K_n'(b\sqrt{\alpha}) + \frac{\nu}{b\sqrt{\alpha}} K_n(b\sqrt{\alpha})\right]\right\} - \\ &\quad - TD_R\sqrt{\alpha_R}\left\{\left[I_{Rn}'(b\sqrt{\alpha_R}) + \frac{\nu}{b\sqrt{\alpha_R}} I_{Rn}(b\sqrt{\alpha_R})\right] - \right. \\ &\quad \left. - S_R\left[K_{Rn}'(b\sqrt{\alpha_R}) + \frac{\nu}{b\sqrt{\alpha_R}} K_{Rn}(b\sqrt{\alpha_R})\right]\right\}. \end{aligned}\right\} \quad (22)$$

These expressions for the constants C_1 etc. are explicit, since the radial stress $(\widehat{rr})_b$ is defined by relation (13). It is interesting to note that, for the corresponding problem of an asymmetrical ring-type reinforcement (*i.e.* a reinforcement with a negligible bending stiffness in the plane of the plate), the radial stress $(\widehat{rr})_b$ cannot be obtained explicitly, since it is a function of the constants defining the deflection surface of the plate. Because of this the order of the Bessel function can only be found by solving a transcendental equation. This particular problem is discussed by the author in Ref. 9.

Using the values just given for the constants, the radial and tangential moments in the plate are given by equations (23) which follow, where $(\widehat{rr})_b$ is given by relation (13).

$$\left.\begin{aligned}
M_r &= D\sqrt{\alpha}\,(\widehat{rr})_b \frac{h^2}{2}(\lambda-1)K\left\{\left[I_n'(x)+\frac{\nu}{x}I_n(x)\right]-\right.\\
&\qquad\left.-T\left[K_n'(x)+\frac{\nu}{x}K_n(x)\right]\right\}\\
M_\theta &= D\sqrt{\alpha}\,(\widehat{rr})_b \frac{h^2}{2}(\lambda-1)K\left\{\left[\nu I_n'(x)+\frac{I_n}{x}(x)\right]-\right.\\
&\qquad\left.-T\left[\nu K_n'(x)+\frac{K_n}{x}(x)\right]\right\}\\
M_{Rr} &= D_R\sqrt{\alpha_R}\,(\widehat{rr})_b \frac{h^2}{2}(\lambda-1)K\left\{S\left[I_{Rn}'(x_R)+\frac{\nu}{x_R}I_{Rn}(x_R)\right]-\right.\\
&\qquad\left.-TS_R\left[K_{Rn}'(x_R)+\frac{\nu}{x_R}K_{Rn}(x_R)\right]\right\}\\
M_{r\theta} &= D_R\sqrt{\alpha_R}\,(\widehat{rr})_b \frac{h^2}{2}(\lambda-1)K\left\{S\left[\nu I_{Rn}'(x_R)+\frac{I_{Rn}}{x_R}(x_R)\right]-\right.\\
&\qquad\left.-TS_R\left[\nu K_{Rn}'(x_R)+\frac{K_{Rn}}{x_R}(x_R)\right]\right\}.
\end{aligned}\right\} \quad . \quad (23)$$

3.3. Built-In Support

For this particular problem the radial slope of the plate is zero at $r=c$, and it can be shown that expressions (21), (22), and (23) are valid provided that S is defined as

$$S=\frac{I_n(c\sqrt{\alpha})}{K_n(c\sqrt{\alpha})}. \quad . \quad . \quad . \quad . \quad . \quad . \quad (24)$$

3.4. Infinite Plate

The induced stress distribution in an infinite plate is defined by a modified Bessel function of the second kind. In general the absolute value of such a function decreases rapidly as its argument increases and is found to become negligible when the radial co-ordinate is several times its value at the junction of the reinforcement and plate. This implies that the solution for an infinite plate can be applied to a plate of finite size, provided that its least lateral dimension is several times the diameter of the hole.

Proceeding as before, for an infinite plate, it can be shown that

$$\left.\begin{aligned}
C_1 &= 0\\
C_2 &= -\frac{(\widehat{rr})_b h^2(\lambda-1)\left[I_{Rn}(b\sqrt{\alpha_R})-S_R K_{Rn}(b\sqrt{\alpha_R})\right]}{2DK_n(b\sqrt{\alpha})\left[L\sqrt{\alpha}-\lambda^3 P\sqrt{\alpha_R}\right]}\\
C_{R1} &= -\frac{(\widehat{rr})_b h^2(\lambda-1)}{2D\left[L\sqrt{\alpha}-\lambda^3 P\sqrt{\alpha_R}\right]}\\
C_{R2} &= \frac{S_R(\widehat{rr})_b h^2(\lambda-1)}{2D\left[L\sqrt{\alpha}-\lambda^3 P\sqrt{\alpha_R}\right]}.
\end{aligned}\right\} \quad . \quad . \quad (25)$$

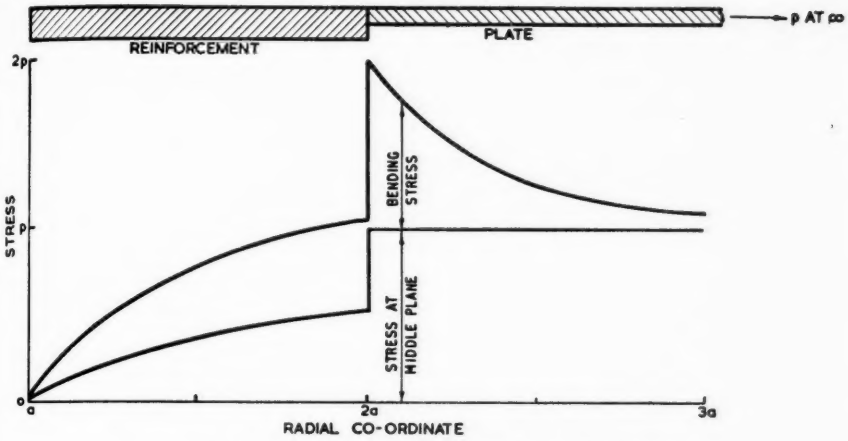

FIGURE 3. Example of radial stress distribution.

Here

$$\left.\begin{aligned} L &= \frac{[I_{Rn}(b\sqrt{\alpha_R}) - S_R K_{Rn}(b\sqrt{\alpha_R})]}{K_n(b\sqrt{\alpha})}\left[K_n'(b\sqrt{\alpha}) + \frac{\nu}{b\sqrt{\alpha}}K_n(b\sqrt{\alpha})\right] \\ P &= \left[I_{Rn}'(b\sqrt{\alpha_R}) + \frac{\nu}{b\sqrt{\alpha_R}}I_{Rn}(b\sqrt{\alpha_R})\right] - S_R\left[K_{Rn}'(b\sqrt{\alpha_R}) + \frac{\nu}{b\sqrt{\alpha_R}}K_{Rn}(b\sqrt{\alpha_R})\right] \\ (\widehat{rr})_b &= \frac{2p}{\left[1 + \frac{1}{\lambda}\left(\frac{b^2+a^2}{b^2-a^2}\right) + \nu\left(1 - \frac{1}{\lambda}\right)\right]}. \end{aligned}\right\} \quad (26)$$

S_R is defined in equations (22).

4. Numerical Example

To illustrate the order of the bending stresses induced in an infinite plate by the asymmetry of a reinforcement, consider the particular case where $b=2a$, $a=30h$ and $\nu=0{\cdot}3$. Also, for convenience of calculation, assume $\lambda=1{\cdot}955$. Then from (2), (5), and (13), it is found that $\beta=0$, $n=1$, and $(\widehat{rr})_b=p$. That is, the stress distribution at the middle plane of the plate is the same as the stress distribution in a similarly loaded plate with no hole. Also, for the particular parameters given here, numerical values for the Bessel functions are given in standard publications (for example, Refs. 10, 11, 12).

For the reinforcement

$$\beta_R = -\frac{a^2b^2(\widehat{rr}_R)_b}{(b^2-a^2)}\frac{h_R}{D_R} = -(x_R)_a^2, \quad . \quad . \quad . \quad . \quad (27)$$

so that

$$n_R^2 = 1 - (x_R)_a^2. \quad . \quad . \quad . \quad . \quad . \quad (28)$$

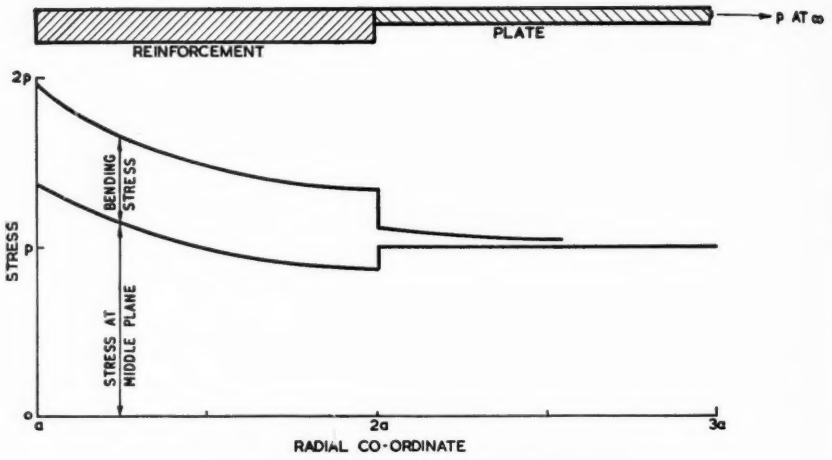

FIGURE 4. Example of tangential stress distribution.

Assuming $E=30\times10^6$ lb./in.^{2}, and for convenience taking $p=17{,}200$ lb./in.^{2}, n is zero, so that the Bessel functions are given again numerically in standard publications.

Thus, using (25) and (26), the stress distribution in the reinforcement and plate are as shown in Figs. 3 and 4. From these figures it is clear that the radial bending stress concentration in the plate, and the total tangential stress concentrations in the reinforcement, are both substantially the same as the tangential stress distribution in a similarly loaded plate with no reinforcement, that is, $2p$.

5. Bessel Functions

Except in a few special cases, it is found that, for practical reinforcements, the order of the Bessel functions and the magnitude of their arguments are outside the range of those given in standard works of reference. For this reason it is proposed to obtain numerical values for a set of parameters which can be used to determine the stress concentrations in plates and reinforcements having a reasonably wide range of practical dimensions.

Considering the reinforcement, the order of the appropriate Bessel functions is given by

$$n_R^2=1+\beta_R=1-\frac{a^2b^2}{(b^2-a^2)}(\widehat{rr}_R)_b\frac{h_R}{D_R}. \quad . \quad . \quad . \quad . \quad (29)$$

Thus, since the applied stress is positive, it follows that $n_R\leqslant 1$.

Also, the order of the Bessel functions is real if

$$\left(\frac{a}{h_R}\right)^2\leqslant\frac{E}{(\widehat{rr}_R)_b}\frac{[1-a^2/b^2]}{12(1-\nu^2)}. \quad . \quad . \quad . \quad . \quad . \quad (30)$$

Now the effect of increasing the reinforcement is to increase the ratio $(\widehat{rr})_b/p$, so that when the ratio is unity the stresses at the middle plane of the plate are the same as those in a similarly loaded plate with no hole. Since there is no practical advantage in increasing the reinforcement to give values of $(\widehat{rr})_b/p$ greater than unity, it may be assumed that, as an upper limit, $(\widehat{rr})_b = p\lambda$.

In this case, from (26) and (29), and assuming $\nu = 0{\cdot}3$, it is found that

$$\left(\frac{a}{h_R}\right)^2 \leqslant \frac{E}{7{\cdot}64\,p}(0{\cdot}7 + 1{\cdot}3a^2/b^2). \quad . \quad . \quad . \quad . \quad (31)$$

This relationship implies that, even for small values of E/p (say less than 2,000), the order of the Bessel functions is real, for practical values of a/b, provided that

$$\frac{\text{diameter of hole in reinforcement}}{\text{thickness of reinforcement}} < 30 \text{ approximately.}$$

In view of this result, design data will be obtained for all values of n_R in the range $0 \leqslant n_R \leqslant 1$. From (28), it follows that for the reinforcement the maximum value of x_R will be

$$(x_R)_{max} = \frac{b}{a}\sqrt{(1 - n_R^2)}.$$

That is, x_R is always sufficiently small to justify the use of the following series to determine the value of the Bessel functions.

$$I_\nu(z) = \sum_{r=0}^{\infty} \frac{(\frac{1}{2}z)^{\nu+2r}}{r!\,\Gamma(\nu + r + 1)} \quad . \quad . \quad . \quad . \quad (32)$$

where $\nu = \pm n_R$

$z = x_R$.

For the plate, x is not always sufficiently small to justify the use of the series (32). In this case values of $K_1(x)$ and $K_0(x)$ can be obtained from Ref. 10, while $K_{1/2}(x)$ is given by

$$K_{1/2}(x) = \left(\frac{\pi}{2x}\right)^{1/2} e^{-x}.$$

Also, using the relationships

$$K_n(x) = \tfrac{1}{2}\pi \frac{[I_{-n}(x) - I_n(x)]}{\sin n\pi}$$

$$I_n(x) = i^{-n}J_n(ix),$$

values of $K_{1/3}(x)$ and $K_{2/3}(x)$ can be calculated from information given in Ref. 11.

Finally, for intermediate values of n, values for the Bessel functions can be interpolated graphically.

6. Design Data

The stress distribution at the middle plane of the plate and reinforcement can be determined readily for any particular example, since $(\widehat{rr})_b$ is given explicitly by equation (13). Thus, for practical application, it is necessary only to tabulate data for the bending stress concentrations. In general the significant bending stress concentration in the plate acts in a radial direction and occurs at the point where the plate is attached to the reinforcement. Also, the significant bending stress concentration in the reinforcement occurs on the boundary of the hole and acts in a tangential direction.

The design data in the rest of this section have been obtained so that these important bending stress concentrations can be evaluated readily for a wide range of practical plate and reinforcement dimensions.

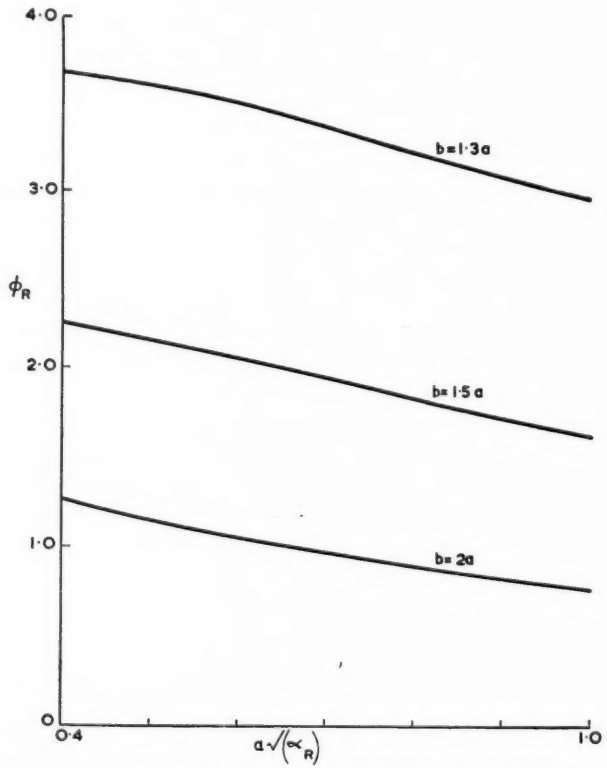

FIGURE 5. ϕ_R for various values of $a\sqrt{(\alpha_R)}$ and b/a.

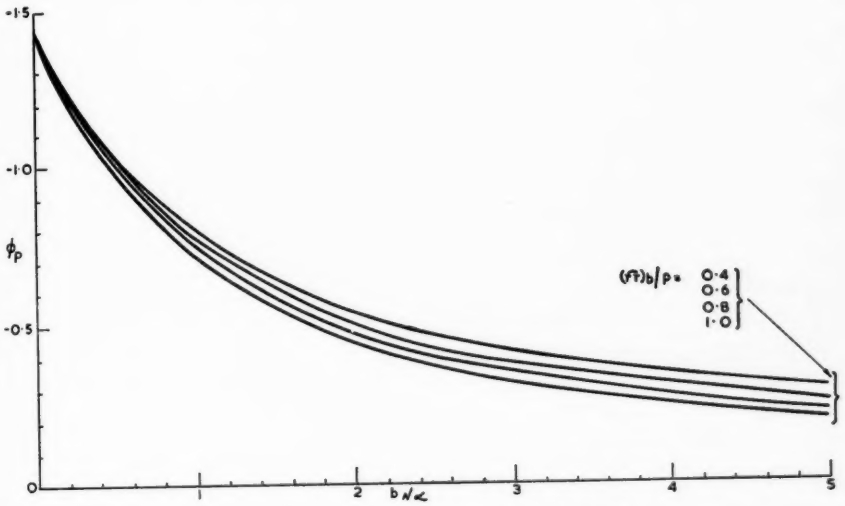

FIGURE 6. ϕ_p for various values of $b\sqrt{\alpha}$ and $\widehat{(rr)}_b/p$.

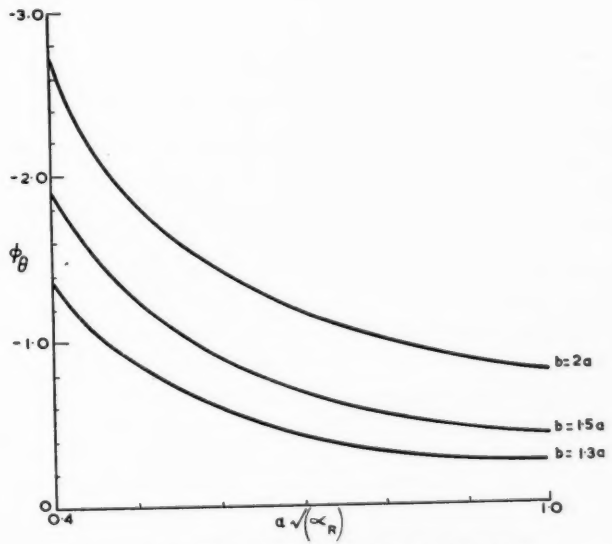

FIGURE 7. ϕ_θ for various values of $a\sqrt{(\alpha_R)}$ and b/a.

For the plate and reinforcement,

$$\left.\begin{aligned}(M_R)_b &= -D\sqrt{\alpha}C_2\left[K_n'(b\sqrt{\alpha})+\frac{\nu}{b\sqrt{\alpha}}K_n(b\sqrt{\alpha})\right]\\(M_{r\theta})_a &= -D_R\sqrt{\alpha_R}\left\{C_{R1}\left[\nu I_{Rn}'(a\sqrt{\alpha_R})+\frac{1}{a\sqrt{\alpha_R}}I_{Rn}(a\sqrt{\alpha_R})\right]+C_{R2}\left[\nu K_{Rn}'(a\sqrt{\alpha_R})+\right.\right.\\&\qquad\left.\left.+\frac{1}{a\sqrt{\alpha_R}}K_{Rn}(a\sqrt{\alpha_R})\right]\right\}.\end{aligned}\right\}\quad(33)$$

For convenience in tabulating design data, the following parameters are introduced into the analysis: —

$$\left.\begin{aligned}\phi_\theta &= \left[I_{Rn}'(b\sqrt{\alpha_R})+\frac{\nu}{b\sqrt{\alpha_R}}I_{Rn}(b\sqrt{\alpha_R})\right]\left[K_{Rn}'(a\sqrt{\alpha_R})+\frac{\nu}{a\sqrt{\alpha_R}}K_{Rn}(a\sqrt{\alpha_R})\right]-\\&\quad-\left[K_{Rn}'(b\sqrt{\alpha_R})+\frac{\nu}{b\sqrt{\alpha_R}}K_{Rn}(b\sqrt{\alpha_R})\right]\left[I_{Rn}'(a\sqrt{\alpha_R})+\frac{\nu}{a\sqrt{\alpha_R}}I_{Rn}(a\sqrt{\alpha_R})\right]\\\phi_R &= \frac{1}{\phi_\theta\, b\sqrt{\alpha_R}}\left\{\left[K_{Rn}'(a\sqrt{\alpha_R})+\frac{\nu}{a\sqrt{\alpha_R}}K_{Rn}(a\sqrt{\alpha_R})\right]I_{Rn}(b\sqrt{\alpha_R})-\right.\\&\qquad\left.-\left[I_{Rn}'(a\sqrt{\alpha_R})+\frac{\nu}{a\sqrt{\alpha_R}}I_{Rn}(a\sqrt{\alpha_R})\right]K_{Rn}(b\sqrt{\alpha_R})\right\}\\\phi_P &= \frac{K_n(b\sqrt{\alpha})}{b\sqrt{\alpha}\left[K'(b\sqrt{\alpha})+\frac{\nu}{b\sqrt{\alpha}}K(b\sqrt{\alpha})\right]}.\end{aligned}\right\}\quad(34)$$

Using the appropriate series for the Bessel functions, numerical values for these parameters have been evaluated and are given graphically in Figs. 5, 6 and 7.

With reference to Fig. 6, for $(\widehat{rr})_b/p$ less than one, Bessel functions defining ϕ_P become imaginary for sufficiently large values of $b\sqrt{\alpha}$. Thus, for $b\sqrt{\alpha}>3$, points on the curves for ϕ_P have been obtained by using the approximate method now described.

Figure 3 shows that the attenuation of the induced radial moment is very rapid in the plate, so that, when the radial co-ordinate is $1{\cdot}5b$ (that is, $3a$ for this particular example), the magnitude of the bending stress is only 7 per cent of its value at the junction of the reinforcement and plate.

In general, for any particular case, the attenuation of the radial stress becomes more rapid as the stress applied to the plate increases. Thus, for practical reinforcements, and for sufficiently high values of the applied stress, the variation in the stress at the middle plane of the plate is small in the region of the plate where the radial bending stresses are concentrated. This implies that the local effects of the induced bending can be determined by assuming that the plate is everywhere under the action of constant radial and tangential stresses of magnitude $(\widehat{rr})_b$.

In this case $\beta=0$, $n=1$, and

$$\phi_P \simeq \frac{K_1(\gamma)}{\gamma\left[K_1'(\gamma)+\frac{\nu}{\gamma}K_1(\gamma)\right]}, \quad . \quad . \quad . \quad . \quad . \quad (35)$$

where $\gamma=b\sqrt{\left[\frac{\alpha(\widehat{rr})_b}{p}\right]}$.

For any particular example, the accuracy of this simplification increases as $b\sqrt{\alpha}$ increases and any error will result in an over-estimate of ϕ_P.

From equations (25), (26) and (34)

$$\left.\begin{aligned} \phi_R &= \frac{K_n(b\sqrt{\alpha})L}{b\sqrt{\alpha_R}\left[K_n'(b\sqrt{\alpha})+\frac{\nu}{b\sqrt{\alpha}}K_n(b\sqrt{\alpha})\right]P} \\ \frac{\phi_R}{\phi_P} &= \frac{L\sqrt{\alpha}}{P\sqrt{\alpha_R}} \\ \frac{\phi_P}{P\sqrt{\alpha_R}(\phi_R-\lambda^3\phi_P)} &= \frac{P\sqrt{\alpha_R}}{L\sqrt{\alpha}-\lambda^3 P\sqrt{\alpha_R}} \\ \phi_\theta &= P\left[K_{Rn}'(a\sqrt{\alpha_R})+\frac{\nu}{a\sqrt{\alpha_R}}K_{Rn}(a\sqrt{\alpha_R})\right]. \end{aligned}\right\} \quad (36)$$

Thus, in terms of these parameters, the moment concentrations become

$$\left.\begin{aligned} (M_r)_b &= \frac{(\widehat{rr})_b h^2(\lambda-1)\phi_R}{2(\phi_R-\lambda^3\phi_P)} \\ (M_{r\theta})_a &= -\frac{(\widehat{rr})_b h_R^2\lambda(\lambda-1)(1-\nu^2)\phi_P}{2(\phi_R-\lambda^3\phi_P)\phi_\theta a^2\alpha_R} \end{aligned}\right\} \quad (37)$$

For any particular example these can be evaluated readily from the curves given in Figs. 5, 6 and 7.

References

1. Timoshenko, S. Stresses on a Plate with a Circular Hole. *Journal of the Franklin Institute*, Vol. 197, p. 508, 1924.
2. Gurney, C. On the Analysis of the Stresses in a Flat Plate with a Reinforced Circular Hole under Edge Forces. R. & M. 1834, 1938.
3. Biskin, L. Strengthening of Circular Holes in Plates under Edge Loads. *Journal of Applied Mechanics*, p. A-140, September 1944.
4. Reissner, H. and Morduchow, M. Reinforced Circular Cut-Outs in Plane Sheets. N.A.C.A. T.N. 1852, April 1949.

5. MANSFIELD, E. H. Neutral Holes in Plane Sheets. *Quarterly Journal of Mechanics and Applied Mathematics*, Vol. VI, Part 3, 1953.

6. HICKS, R. Reinforced Elliptical Holes in Stressed Plates. *Journal of the Royal Aeronautical Society*, Vol. 61, p. 688, October 1957.

7. MANSFIELD, E. H. Optimum Designs for Reinforced Circular Holes. A.R.C. Current Paper 239, 1956.

8. HICKS, R. Variably Reinforced Circular Holes in Stressed Plates. *Aeronautical Quarterly*, Vol. IX, August 1958.

9. HICKS, R. Asymmetrically Ring-Reinforced Circular Hole in a Uniformly End-Loaded Plate, with Reference to Pressure Vessel Design. *The Chartered Mechanical Engineer*, Vol. 5, November 1958.

10. British Association Mathematical Tables. Cambridge University Press, 1950.

11. JAHNKE, E. and EMDE, F. *Funktionentafeln*. Teubmer, Leipzig, 1933. Dover Publications, New York. p. 235, 1943.

12. MCLACHLAN, N. W. *Bessel Functions for Engineers*. Second edition. Clarendon Press, Oxford, 1955.

and

ical

per

rly,

ded
eer,

ons,

ess,

rly